

Quantum Simulation with Ultracold Atoms and Trapped Ions

by
Guin-Dar Lin

A dissertation submitted in partial fulfillment
of the requirements for the degree of
Doctor of Philosophy
(Physics)
in The University of Michigan
2010

Doctoral Committee:

Associate Professor Luming Duan, Chair
Professor Paul R. Berman
Professor Georg A. Raithel
Professor Duncan G. Steel
Assistant Professor Aaron E. Leanhardt

To my parents.

ACKNOWLEDGEMENTS

I am deeply grateful to my advisor, Professor Luming Duan, for mentoring me throughout my graduate research years. My first introduction to him was in the first-year Quantum Mechanics class he taught. I was overwhelmed by his broad knowledge and sharp insights on various subjects. The feeling has become even stronger since I joined the group and started working with him. He is always easily accessible for questions and discussions, and the atmosphere of discussion is always pleasant and refreshing. I am very fortunate and honored to have had him as my advisor for these years. Now I feel I know better how to appreciate the beauty of the quantum world and how to deal with problems; it is all thanks to him.

I am also thankful to my former and current groupmates, Wei Yi, Bin Wang, Timothy Goodman, Jason Kestner, Wei Zhang, Yongjian Han, Yang-Hao Chan, Zhexuan Gong, Chao Shen, Zhaohui Wei, Zhangqi Yin, Jin Xiong, and my good friends, Yu-Miin Sheu and Jia-Yin Chao, for their support and companionship during these years in Ann Arbor. I cherish every opportunity to interact with them and benefit a lot from their valuable opinions and advice. I would especially like to thank Wei Yi, who helped me familiarize myself with the subjects of study when I first came to the group (including helping publish my first paper), Wei Zhang, who shared lots of his experiences and inspired me in many ways, and Jason Kestner, who has been not only my classmate and a smart collaborator but also a best friend during these years. I appreciate his friendship and understanding in all aspects; through him I

see only positive attitudes for being an enthusiastic researcher and also a civilized person.

I also would like to acknowledge Professor Shi-Liang Zhu in South China Normal University at Guangzhou, China, Professor Chris Monroe in the Joint Quantum Institute of the University of Maryland at College Park and National Institute of Standards and Technology and members in his group, Ming-Shien Chang, Kihwan Kim, Simcha Korenblit, Islam Rajibul, and Professor Jim Freericks in Georgetown University for their collaboration and efforts in the work of large-scale trapped ion quantum computation and simulation.

Finally, I must thank my family in Taiwan. I could never get this far without their unselfish sacrifice, constant encouragement, and support.

TABLE OF CONTENTS

DEDICATION	ii
ACKNOWLEDGEMENTS	iii
LIST OF TABLES	vii
LIST OF FIGURES	viii
LIST OF APPENDICES	xiii
ABSTRACT	xiv
CHAPTER	
I. Introduction	1
1.1 Motivation	1
1.2 Background	3
1.2.1 Quantum simulation with neutral gases: BEC-BCS crossover	3
1.2.2 Quantum simulation with optical lattices	7
1.2.3 Quantum computation and simulation with trapped ions	11
1.3 Thesis Outline	15
II. Ultracold Fermi Gas with Spin Population and Mass Imbalance	18
2.1 Overview	18
2.2 Formalism	19
2.2.1 Basic Hamiltonian: two-channel model	19
2.2.2 Single-channel model	20
2.2.3 Effects of traps and the local-density approximation	21
2.2.4 Fermi gases with population and mass imbalance	22
2.3 Results and Discussion	24
2.4 Chapter Summary	31
III. BCS-BEC Crossover in a Quasi-two-dimensional Fermi Gas	32
3.1 Overview	32
3.2 Model 1 with Renormalized Atom-atom Interaction	34
3.3 Model 2 with Inclusion of Dressed Molecules	38
3.4 Chapter Summary	42
IV. Characteristics of Bose-Einstein Condensation in an Optical Lattice	44
4.1 Overview	44

4.2	Ideal Bose Gas in an Inhomogeneous Optical Lattice	47
4.2.1	Formalism	47
4.2.2	Interference patterns	49
4.2.3	Visibility	52
4.2.4	Momentum-space density profile and the peak width	54
4.2.5	The condensate fraction as a measure of temperature	57
4.3	Interacting Bose Gas in an Inhomogeneous Optical Lattice	59
4.3.1	Visibility of the interference pattern	62
4.3.2	Momentum-space density profile and the peak width	65
4.3.3	The condensate fraction	68
4.3.4	Interaction effects during the time-of-flight expansion	71
4.4	Chapter Summary	75
V. Large-scale Quantum Computation in an Anharmonic Linear Ion Trap . .		76
5.1	Overview	76
5.2	Scalability	77
5.3	Anharmonic Architecture	79
5.4	Gate Design	81
5.5	Other Imperfections	86
5.6	Chapter Summary	87
VI. Quantum Simulation of Ising Magnets with Trapped Ions		89
6.1	Overview	89
6.2	Formalism	91
6.3	Three-ion Network	93
6.4	Experimental Comparison	98
6.5	Multiple-ion Network	101
6.6	Chapter Summary	105
VII. Conclusions		107
7.1	Summary	107
7.2	Future Directions	111
APPENDICES		113
BIBLIOGRAPHY		119

LIST OF TABLES

Table

6.1	Coupling pattern and the corresponding ground spin configurations for the three-ion network. The coupling pattern is classified into types: all bonds are ferromagnetic (FM), anti-ferromagnetic (AFM), and hybrid with the nearest-neighbor coupling stronger than the next-nearest-neighbor (Short), or the opposite (Long). FM or AFM in parentheses denotes the type of the stronger bond. Note that when approaching the CM mode ($\tilde{\mu} \rightarrow 0^\pm$), the two couplings are asymptotically identical and introduce extra degeneracy.	94
6.2	Ground spin configurations for odd numbers of ions. For the spin order indicated in binary numbers, only one specific component is shown. The real ground states should be superpositions of all possible configurations that can be transformed from this specific component by Z_2 transformation and reflection with respect to the middle ion. Among rows, the thick borders between different spin configurations indicate the separation due to motional modes; the dashed borders indicate the change of spin order due to competing interactions, with similar coupling patterns, between modes. The number beside a dashed border shows the corresponding (rescaled) detuning μ' (see text).	102

LIST OF FIGURES

Figure

1.1	Illustration of BEC-BCS crossover. Two spin types are represented in different colors. On the BEC side, two spin species form deep-bound molecules (composite bosons). On the BCS side, the fermions are loosely bound and paired in the momentum space. In the middle region the effective scattering length diverges, signaling a strong interaction between atoms.	5
1.2	Energy diagram for a Feshbach resonance. The closed channel potential with a bound state is coupled to the scattered state continuum of the open channel. The degree of resonance can be adjusted by a magnetic field through Zeeman effects.	6
1.3	Two-level configuration for a neutral atom interacting with the laser field. In this illustration the spontaneous emission is neglected.	8
1.4	Graphical representation for a Cirac-Zoller gate.	12
1.5	Graphical representation for a Sørensen-Mølmer gate. A bichromatic field is applied with two frequencies summed up to $2\omega_{eg}$. Because both frequencies are detuned off the energy levels, the transitions occur only when two photons are absorbed or emitted. Different paths interfere with each other and eliminate the dependence of phonon population. (Figure from [55].)	13
2.1	The zero temperature phase diagrams for trapped ${}^6\text{Li}$ - ${}^{40}\text{K}$ mixture near a Feshbach resonance. The phases include the BCS superfluid state (SF), the breached pair phase of type 1 (BP1), the normal mixture (NM_K or NM_{Li} , with ${}^{40}\text{K}$ or ${}^6\text{Li}$ in excess, respectively), and the normal polarized (single-component) states (NP_K or NP_{Li}). The phases are shown versus the population imbalance p and the normalized trap radius \tilde{r}	25
2.2	(a) The thermodynamical potential Ω shown as a function of the order parameter Δ (both in the unit of E_F) at different trap positions (different chemical potentials) characterized by the normalized radius \tilde{r} . The other parameters are $p = 0.2$, $T = 0$, and $(k_F a_s)^{-1} = 0$. The two solid curves bound a region corresponding to the SF phase, where the global minimum of Ω is at a nonzero Δ . (b) and (c) Schematic illustration of the radius of the Fermi surfaces k_F^σ for the two components as a function of the normalized trap radius \tilde{r} . In (b), one can only have a superfluid core at the trap center, while in (c), one in general has a superfluid shell in the intermediate region.	29

2.3	The atomic number densities n_σ (in the unit of $n_F \equiv k_F^3/(3\pi^2)$) shown versus the normalized trap radius \tilde{r} . The solid (dashed) curves are for the ^{40}K (^6Li) atoms, respectively. The inserts of (a) and (b) show the amplified tails of the density profiles. The other parameters are: (a) $T = 0$, resonance, and $p = 0.2$, (b) $T = 0.1T_F$, resonance, and $p = 0.2$, (c) $T = 0$, $(k_F a_s)^{-1} = -1$ (BCS side), $p = -0.4$, (d) $T = 0$, $(k_F a_s)^{-1} = 0.2$ (BEC side), $p = 0.3$	30
3.1	The BCS-BEC crossover behavior of a uniform quasi-2D Fermi gas at zero temperature, showing (a) the chemical potential μ , (b) the gap Δ , both in unit of $\hbar\omega_z$, and (c) the dressed-molecule fraction n_b/n . Notice that the results for ^6Li (solid) and those for ^{40}K (dashed) almost coincide as plotted as functions of a_z/a_s , indicating a universal behavior around the resonance point. Furthermore, significant difference between model 1 (gray) and model 2 (black) can be observed in (b) and (c), which shows that model 1 is oversimplified at unitary and on the BEC side of the resonance. The parameters used in these plots are $\omega_z = 2\pi \times 62$ kHz, and $na_z^2 = 0.001$	39
3.2	The Thomas-Fermi cloud size of a quasi-2D Fermi gas of ^6Li over a wide BCS-BEC crossover region. Here, results from model 2 (solid) are compared with those from model 1 (dashed). All curves are normalized to the cloud size of a noninteracting Fermi gas R_{BCS} . Notice that the results of model 2 recover the correct pictures in the BCS and BEC limits, in clear contrast to the model 1 prediction of a flat line. Parameters used for these two plots are $\omega_z = 2\pi \times 62$ kHz, $\omega_\perp = 2\pi \times 20$ Hz, and the total particle number $N = 10^4$. For reference, the results for an isotropic 3D Fermi gas with the same total particle number is also plotted (dotted), where a single-channel model and a two-channel model are both incorporated to give indistinguishable predictions.	40
3.3	The in-trap number density (the solid lines) and dressed-molecule fraction (the dashed lines) distribution along the radial direction of a quasi-2D Fermi gas of ^6Li , obtained from model 2 (a-c) and model 1 (d-f). The top panels correspond to the case of $a_z/a_s = -1$ (BCS side), the middle panels to the case of $a_z/a_s = 0$ (unitary), and the bottom panels to the case of $a_z/a_s = 1$ (BEC side). The parameters are $\omega_z = 2\pi \times 62$ kHz, $\omega_\perp = 2\pi \times 20$ Hz, and $N = 10^4$	42
4.1	Calculated column-integrated momentum density profile near the first Brillouin zone measured through the time-of-flight imaging, taking for two different trapping frequencies at various temperatures. Parameters chosen in these plots are close to those for a typical experiment of ^{87}Rb , with lattice depth $V_0 = 10E_R$ and a total number of particles $N = 10^5$. The global harmonic trapping frequencies are $\omega = 2\pi \times 10$ Hz for (a)-(c), and $2\pi \times 60$ Hz for (d)-(f).	50
4.2	The visibility as a function of temperature around the BEC transition temperature T_c for various values of trapping frequencies. Other parameters are the same as those used in Fig. 4.1 with $V_0 = 10E_R$ and $N = 10^5$. Remind that the variation of V_0 is equivalent to that of ω , with a fixed value of $\hbar^2\omega^2/(V_0^{3/4}e^{-2\sqrt{V_0}})$	52

4.3	Correlation functions around the trap center indicating real space coherence below (for a superfluid, SF) and above (for a thermal gas, TG) the BEC transition temperature, with trapping frequencies (a) $\omega = 2\pi \times 10$ Hz, (b) $2\pi \times 60$ Hz, and (c) $2\pi \times 120$ Hz. Curves in each panel are taken at, from top to bottom, $0.9T_c$ (solid), $0.95T_c$ (solid), $1.0T_c$ (dotted), $1.05T_c$ (dashed), and $1.1T_c$ (dashed), respectively. Parameters used in these plots are $V_0 = 10E_R$ and $N = 10^5$. For reference, the characteristic length of the single particle ground state wavefunction adjusted by effective mass ($L \equiv \sqrt{\hbar/m^*\omega}$) are (in unit of the lattice constant) (a) $L = 3.80$, (b) $L = 1.55$, and (c) $L = 1.09$, respectively.	54
4.4	Momentum space columnar density along the x -axis in the first Brillouin zone. The left and right panels correspond to the cases of trapping frequencies $\omega = 2\pi \times 10$ Hz and $2\pi \times 60$ Hz, respectively. Notice that while a thermal distribution is present above T_c [(c) and (f)], a clear bimodal structure starts to appear for temperatures slightly below T_c with only precentral condensate fractions [$n_0 \sim 0.14$ in (b) and ~ 0.09 in (e)]. Here, the solid curves represent the total momentum density profile, and the dashed curves represent the momentum density profile of the normal component. Parameters used in these plots are $V_0 = 10E_R$ and $N = 10^5$	56
4.5	The peak width (defined in the text) within the first Brillouin zone, taking across the transition temperature for various values of trapping frequencies. Notice that the sharp and substantial change around T_c occurs for all cases hence serves as a distinctive signature of BEC transition. Parameters used in these plots are $V_0 = 10E_R$ and $N = 10^5$	57
4.6	The condensate fraction as a function of temperature below the BEC transition. By extracting n_0 from the momentum distribution as shown in Fig. 4.4(a-b) and (d-e), temperatures of such cases can be determined correspondingly (triangles). Parameters used in this figure are $V_0 = 10E_R$ and $N = 10^5$	58
4.7	The visibility as a function of temperature around the BEC transition temperature T_c for (a) $V_0 = 10E_R$ and (b) $\omega = 2\pi \times 60$ Hz. The number density per site at the trap center is set as $n_{\text{tot}} = 1$, and the total number of particles in the trap is $N \sim 10^4$	63
4.8	Momentum space columnar density along the x -axis in the first Brillouin zone, where clear bimodal structures appear for temperatures below T_c . Here, the solid curves are the total momentum density profile, and the dashed curves are the momentum density profile of the normal component. The trapping frequency used in these plots is $\omega = 2\pi \times 60$ Hz, and the number density per site is unity at the trap center.	66
4.9	The peak width within the first Brillouin zone, taking across the transition temperature for (a) $V_0 = 10E_R$ and (b) $\omega = 2\pi \times 60$ Hz. The number density per site is unity at the trap center.	67
4.10	The condensate fraction as a function of temperature below the BEC transition, for an interacting Bose gas in an optical lattice with $\omega = 2\pi \times 60$ Hz and different lattice barriers V_0 . The number density per site is unity at the trap center. By comparing with the momentum distribution as shown in Fig. 4.8, temperatures of such a system can be determined correspondingly (triangles).	69

4.11	The in-trap quantum depletion fraction as a function of the lattice barrier V_0 . The trapping frequency is $\omega = 2\pi \times 60$ Hz. The number density per site at the trap center is unity.	69
4.12	The number and condensate density distribution along the radial direction away from the trap center. Two different temperatures are considered as in (a) $T = 0.1T_c$, and (b) $T = 0.8T_c$. The solid curves correspond to the overall density profiles and the dashed curves to the condensate portions. The trapping frequency used here is $\omega = 2\pi \times 60$ Hz. The total number of particles N_{tot} and the number of condensate particles N_0 are respectively (a) $V_0 = 6E_R$ (red): $N_{\text{tot}} = 0.54 \times 10^4$, $N_0 = 0.50 \times 10^4$; $V_0 = 10E_R$ (black): $N_{\text{tot}} = 1.3 \times 10^4$, $N_0 = 1.0 \times 10^4$; (b) $V_0 = 6E_R$ (red): $N_{\text{tot}} = 2.5 \times 10^4$, $N_0 = 2.8 \times 10^2$; $V_0 = 10E_R$ (black): $N_{\text{tot}} = 2.3 \times 10^4$, $N_0 = 6.7 \times 10^2$	70
4.13	Illustration of the scattering between atoms from different peaks (the central and the secondary). This process leads to blurring of the interference peaks with a characteristic blurring pattern.	73
5.1	Linear architecture for large scale quantum computation, where lasers address individual ions and couple to local modes of the ions, while the edge ions are continuously Doppler laser-cooled. In a large ion chain, more efficient sympathetic cooling could be achieved with cooling ions sparsely distributed in the ion chain.	79
5.2	(a) Sample five-segment linear ion trap with voltages $V_i (i = 1, 2)$ to produce a quartic axial potential. The ions are confined in the central segment. (b) The variance of the ion spacings s_z in a linear quartic trap as a function of the trap parameter B that characterizes the ratio of quadratic to positive-quartic nature of the potential. (c) The distribution of the ion spacing at the optimum value $B = -6.1$. The computational ions are within the dashed lines, where the spacing is essentially uniform.	82
5.3	(a) The gate infidelity δF as a function of the laser detuning μ from the qubit resonance, with optimized Rabi frequencies over $M = 5$ equal segments of the laser pulse. Different curves correspond to different gate times. The 120 transverse phonon modes are all distributed within the narrow frequency range indicated by the two vertical lines. (b) The shape of the laser pulse $\eta\Omega$ (in units of ω_x) that achieves the optimal fidelity (with $\delta F = 8.5 \times 10^{-6}$), at the detuning shown by the arrow in (a) (with $(\mu - \omega_x)/\omega_x = 9.3 \times 10^{-3}$) and the gate time $\tau = 500\tau_0$. The dashed (or dotted) lines represent the approximate optimal solutions of the laser shape where only 4 (or 8) ions (from the 59th to 62nd or the 57th to 64th, respectively) are allowed to vibrate and all the other ions are fixed in their equilibrium positions. This approximation does not significantly change the optimal laser pulse shape compared to that of the exact solution (represented by the solid line) where all ions are allowed to vibrate, so the gate is essentially local and the gate complexity does not depend on the crystal size. (c) The relative response of the ions for the gate shown in (b) (characterized by the largest spin-dependent shift $ q_n^{(m)} $ during the gate time τ). We take a relative unit where $ q_n^{(m)} $ for the target ions have been normalized to 1. The fast decay of the response as one moves away from the target ions (59th and 62nd) shows that the gate involves vibration of only local ions.	84
6.1	Coupling coefficients and ratio as a function of the normalized detuning $\tilde{\mu}$	93

6.2	Phase diagram showing the projection (probability) of the ground state to the FM order component. ($J_{rms} \equiv \sqrt{(2J_{12}^2 + J_{13})/3}$)	95
6.3	Time evolution of the probability of each component for (a) $J_{12} = J_{13} = 1\text{kHz}$, (b) $J_{12} = -1\text{kHz}$, $J_{13} = -2\text{kHz}$, (c) $J_{12} = -1\text{kHz}$, $J_{13} = 2\text{kHz}$, (d) $J_{12} = -1\text{kHz}$, $J_{13} = 0.8\text{kHz}$. The components with significant probabilities are pointed out by binary numbers where $1 \rightarrow \uparrow\rangle$ and $0 \rightarrow \downarrow\rangle$. About the evolution path, first keep $B = B_0 = 10\text{kHz}$ (x direction) and increase B_z (z direction) from 0 to 1kHz within $T_1 = 0.1\text{ms}$; then keep $B_z = 1\text{kHz}$ and follow $B(t) = B_0 \exp(-t/T_2)$ with $T_2 = 0.2\text{ms}$. Only the evolution curves for the final step are shown here.	97
6.4	(a) The theoretical phase diagram (same as Fig. 6.2). Indicated by the vertical arrows are the evolution paths for case (b) to case (f). (b–f) The time evolution curves for each basis component. The scattered points correspond to the experimental data; the dashed curves correspond to the instantaneous (absolutely adiabatic) ground states, and the solid curves correspond to theoretical finite-speed evolution. (Figure from [70].)	98
6.5	Entanglement witness measurements as $ B /J$ is ramped down for (a) FM and (b) AFM regions (see Fig. 6.4). A negative value indicates entanglement. Here, $ J_{13}/J_{12} \sim 0.85$. The blue dots correspond to the experimental data for (a) the GHZ witness and (b) the W-type witness. The dashed curves correspond to the absolutely adiabatic evolution and the solid curves correspond to the theoretical finite-speed ramping. For (a), the experimental data for the GHZ fidelity F_{FM} (see Sec. 6.3) is plotted in green dots. ($F > 0.5$ indicates entanglement.) (Figure from [70].)	99
6.6	The effect of a symmetry breaking field B_z in the FM region (a–c) and AFM region (d–f). Panel (a), (b) and (d), (e) show the population in different components of the resultant state, without and with a symmetry breaking field, respectively. The probabilities P_0, P_1, P_2, P_3 corresponding the projection of the state to the σ^z eigen-component(s) of 0, 1, 2, 3 \uparrow 's (number of up-spins). Panel (c) and (d) show the instantaneous entanglement witness during the ramp. The blue (red) dots correspond to no-field (finite-field) cases. (Figure from [70].)	100
6.7	Phase diagrams of odd numbers of ions. (x-axis: the rescaled detuning μ' ; y-axis: B/J_{rms} ; color-axis: $P_{FM} - P_K$ with P_{FM} and P_K are the projection (probability) of the ground state to the FM- and kink-order components, respectively.)	104
6.8	Level crossing at the FM-Kink transition. Two FM ground states intersect with two Kink ground states with an energy gap raised by the transverse field.	105
A.1	Integration area for $\phi_{ij}(\tau)$. Each piece has a contribution weighted by the corresponding $\Omega_m \Omega_{m'}$	115
B.1	The axial position fluctuation δz_n is plotted along the ion chain, which is about $0.26\mu\text{m}$ (averaged) for the computational ions (n from 11 to 110).	118

LIST OF APPENDICES

Appendix

- A. Segmental Pulse Shaping 114
- B. Thermal position fluctuation for trapped ions along the axial direction 117

ABSTRACT

In this thesis we discuss several aspects of ultracold atomic systems and their applications to quantum simulation. These topics cover a degenerate gas near a Feshbach resonance, superfluids in an optical lattice, trapped-ion quantum computation and simulation.

We study a degenerate Fermi gas when the interaction is tuned from the Bose-Einstein Condensation (BEC) side to the Bardeen-Cooper-Schrieffer (BCS) side, investigating effects due to population and mass imbalance. We identify various phases and find that a superfluid shell can be observed within a trap because of the mass mismatch.

We study a Fermi gas in a quasi-two-dimensional geometry formed by optical lattices. A two-channel model is proposed to describe the BEC-BCS crossover physics. We find the higher-band excitations cannot be neglected and contribute to the closed channel as effective Feshbach “dressed molecules”. This model predicts a decrease in the cloud size as the interaction is tuned from the BCS side to the BEC side.

To investigate superfluidity of bosons in an optical lattice, we calculate the momentum distribution related to the time-of-flight (TOF) interference patterns at finite temperature. We find that a distinct bimodal distribution of the TOF image is presented as long as superfluids emerge, and hence can be used as a reliable signature indicating onset of superfluidity.

We propose a large-scale quantum computer architecture by stabilizing a single

large linear ion chain in a linear trap geometry. By confining ions in an anharmonic linear trap with nearly uniform spacing between ions, we show that high-fidelity quantum gates can be realized in large linear ion crystals under the Doppler temperature based on coupling to a near-continuum of transverse motional modes with simple shaped laser pulses.

Finally, we demonstrate the trapped ion quantum simulation of the Ising model. Through control of the laser detuning, various coupling networks can be realized. We give a detailed discussion of the frustrated nature in three-ion cases and show the achievable phases as the the system size grows. A comparison of our calculation and experimental data is presented.

CHAPTER I

Introduction

1.1 Motivation

For decades ultracold atomic systems have drawn intense attention for their potential applications to quantum simulation and information science. The idea of quantum simulation is motivated by R. Feynman's 1982 conjecture [1], in which he suggested that a wide range of quantum many-body phenomena might be imitated by certain classes of quantum systems, and that if so, it would be possible to construct a universal quantum computer that approximates various quantum mechanical systems and even the physical world. Atomic systems, owing to their exceptional optical or magnetic accessibility, parametric controllability, fine isolation from environment within certain time scales, and low-temperature strongly-correlated behavior, make themselves a promising candidate for quantum many-body simulation. To continue exploring possible applications and making realistic progress, it is essential for us to first understand the general behavior of such systems and how these behaviors can be manipulated and engineered.

For a many-body system to reach a regime where quantum behaviors dominate, thermal effects must be suppressed. This is the major reason why ultracold physics comes into play. In 1924, S. N. Bose and A. Einstein predicted the Bose-Einstein

Condensation (BEC) for bosons cooled below a critical temperature. Many exotic phenomena, such as superconductivity in solids and superfluidity in helium-3 and helium-4, were explored and found to be intimately related to occurrence of condensates (for general materials, see, e.g., [2]). The first BEC of an atomic gas was realized by E. Cornell and C. Wieman for rubidium ^{87}Rb atoms (bosons) in 1995 [3]. Due to the fermionic nature and weak interaction among fermion pairs, the BEC of a Fermi gas required a fairly restrictive temperature condition, and therefore was not observed until 2003 when D. S. Jin's group realized a potassium ^{40}K condensate [4] by means of the so-called Feshbach resonance [5, 6]. These achievements are good examples of quantum simulation by ultracold atomic systems, which can be appropriately manipulated in order to present condensation and superfluidity as in helium-4 for the boson cases, as well as fermion cases such as helium-3 and superconductivity in superconductors.

Optical lattices make another example showing extraordinary controllability. They are formed from the interference of one or more pairs of counter-propagating laser beams, which set up an effective periodic potential structure in space. They provide a testbed that resembles the actual crystalline solids, thus making simulation of solid-state physics possible within ultracold atoms (for reviews, see, e.g., [7, 8]). Other applications of optical lattices include realization of low-dimensional geometries [9–12] and scalable quantum computation [13].

Compared to the neutral atoms, trapped ions bear the advantage of stronger Coulomb interaction. In the context of quantum computation, they show faster gate speeds for quantum operation, longer coherence time, and better accessibility including individual ion transportation, cooling, state preparation and measurement. At present, trapped ions are regarded as the most advanced system for future implemen-

tation of a quantum computer. However, the scalability issue is still a challenging task [14, 15]. Searching for a solution is a necessary step toward practical use.

This thesis is motivated by the possibilities of using ultracold atoms and trapped ions in quantum simulation. Up to the present these systems have demonstrated convincing potential through numerous experimental findings and theoretical considerations. This field promises to remain active for decades to come, not only because continuing efforts are needed to ultimately realize a quantum computer, but also due to its close connection to many other important topics, for example, high- T_c superconductivity [16–18] and quantum Hall effects [19, 20].

1.2 Background

In this section, we set the stage for this thesis by briefly reviewing the basic concepts associated with the systems of interest, including (a) the crossover physics in a Fermi gas from the BEC regime to the Bardeen-Cooper-Schrieffer (BCS) regime, (b) optical lattices and the Hubbard model, and (c) trapped ion computation basics. More discussion can be found in corresponding chapters and references therein.

1.2.1 Quantum simulation with neutral gases: BEC-BCS crossover

This subject deals with a collection of interacting Fermi atoms being cooled to quantum degeneracy, where a macroscopic fraction of them can occupy the same quantum state. This is understood as the BEC for bosonic species. However, due to the Pauli exclusion principle, the occupancy of the same state for individual fermions is forbidden unless they form pairs and can then be considered as composite bosons. One can imagine a scenario where two fermions are tightly bound so that their two-body wavefunction can be regarded as a single wavepacket and their internal degrees of freedom are not important. This corresponds to the case where the interspacing

between wavepackets is much larger than the size of the two-body wavefunction. It can be expected that these two-body molecules condense like bosons when they are cooled below a critical temperature. We call this regime the BEC side in the language of BEC-BCS crossover physics (the left panel of Fig. 1.1). The other limiting case is that in which the fermions are only weakly attracting, a situation studied in the context of superconductivity by J. Bardeen, L. N. Cooper, and J. R. Schrieffer in 1957 [21]. In superconductivity, electrons form pairs, so-called Cooper pairs, in the presence of a weak inter-attraction mediated by crystal vibrations (phonons). According to the BCS theory, the favored ground state is that in which fermions form pairs in momentum space (and condense below the critical temperature). Their two-body wavefunctions extend in space and significantly overlap with each other. This scenario is thus called the BCS side (the right panel of Fig. 1.1).

The intermediate region is then defined when the two tightly bound fermions on the BEC side start to dissociate, or the overlap of the two-body wavefunctions on the BCS side diminishes (the middle panel of Fig. 1.1). More precisely, the BEC-BCS crossover occurs when the binding energy characterizing the molecular state is comparable to the Fermi energy associated with the (loose paired) individual fermions. At this region, called the unitary region, the crossover physics of the Fermi systems should show unique properties, neither entirely bosonic nor fermionic in nature; interesting behaviors can be expected and merit exploration.

The continuous change from the BEC side to the BCS side can be done through the Feshbach resonances, which occur when a two-particle scattering state (called an open channel) resonates with a bound state (called a closed channel). Consider two spin-1/2 fermions in a colliding process and treat them in a basis of singlet ($S = 0$) and triplet ($S = 1$) states. (In current experiments on ${}^6\text{Li}$ atoms, for example, the

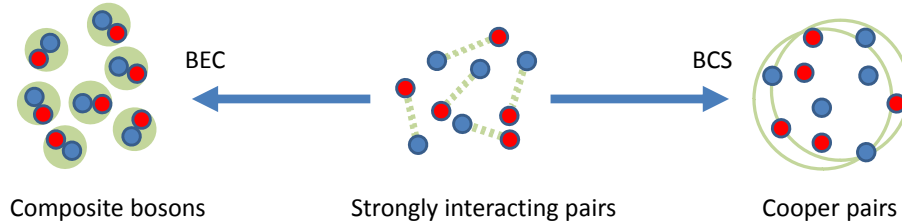


Figure 1.1: Illustration of BEC-BCS crossover. Two spin types are represented in different colors. On the BEC side, two spin species form deep-bound molecules (composite bosons). On the BCS side, the fermions are loosely bound and paired in the momentum space. In the middle region the effective scattering length diverges, signaling a strong interaction between atoms.

two spin states correspond to $|F = 1/2, m_F = 1/2\rangle$ and $|F = 1/2, m_F = -1/2\rangle$.)

Suppose there is a bound state in the $S = 0$ channel (closed channel) close to the scattering continuum in the $S = 1$ channel (open channel). The two colliding fermions, with a propagating wavefunction, have a chance to be captured in the near-resonant bound state, and then dissociate again in a time-scale $t \sim \hbar/\Delta E$, where ΔE is the energy difference between the bound state and the lowest eigenket of the scattering continuum. The interaction is thus effectively modified. Note that ΔE can be controlled continuously by an external magnetic field due to the Zeeman shift.

The interaction of atoms under consideration is through collision, and for spin-1/2 fermions can be characterized by the s -wave scattering length a_s . The magnitude and sign of a_s indicate the strength and whether the effective interaction is repulsive ($a_s > 0$) or attractive ($a_s < 0$), respectively. For a Fermi gas near a Feshbach resonance, the s -wave scattering length is given by [22, 23]

$$a_s = a_{bg} \left(1 - \frac{W}{B - B_0} \right), \quad (1.1)$$

where a_{bg} is the background scattering length, W is the resonance width, and B_0 is the magnetic field such that ΔE is exactly tuned to 0, i.e. on resonance. We can see that a_s flips sign when B passes through B_0 and diverges exactly on resonance, indicating that in this region the atoms are strongly interacting. On resonance the

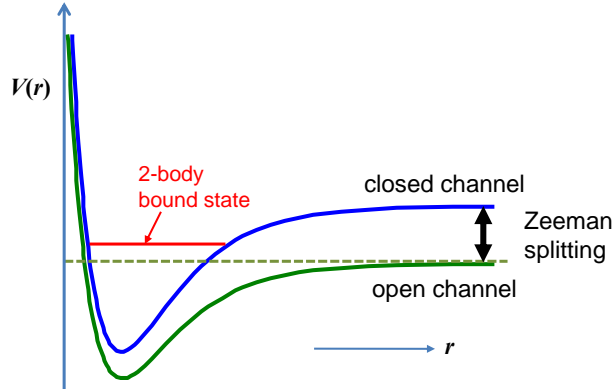


Figure 1.2: Energy diagram for a Feshbach resonance. The closed channel potential with a bound state is coupled to the scattered state continuum of the open channel. The degree of resonance can be adjusted by a magnetic field through Zeeman effects.

system shows some unique properties [24, 25] due to the singularity of the interaction range, which means the only length scale is set by the interspacing of the atoms ($\sim n^{-1/3}$, where n is the number density).

Recent efforts along this line of research focus on magnetized Fermi gas, in which the two spin species have unequal populations [26–33]. At zero temperature, it can be expected that the formation of (s -wave) pairs normally takes the same numbers of opposite spin particles and the remainder should be left unpaired. Therefore the magnetized Fermi gas usually consists of both superfluid and normal fermion parts. The actual mechanism is in fact more subtle because the discrepancy in the Fermi surfaces leads to suppression of Cooper pairing. Other possibilities of “nontrivial” pairing mechanisms have been proposed, including the breached-pair phase [31, 34, 35] and the Fulde-Ferrell-Larkin-Ovchinnikov (FFLO) state [31, 35–37], which may contribute to stable or meta-stable ground states by finite magnetization. The mass ratio of the two species serves as an additional tunable parameter, and it is introduced when two types of fermionic atoms (elements) are mixed. More details can be found in Chapter II.

1.2.2 Quantum simulation with optical lattices

Optical lattices are an important example in ultracold atomic physics. They are formed by the interference of pairs of counter-propagating laser beams at different angles. By tuning the intensity of lasers and the incident angles, one is able to control the barrier depth and the lattice constant, i.e. the site spacing. Here we briefly explain the working mechanism of optical lattices. We use a semi-classical point of view by treating the laser beams as a classical electromagnetic field. Consider an atom whose transition behavior can be described by a two-level system (Fig. 1.3) sitting in the interference pattern of the laser field, i.e. a standing wave field: $\mathbf{E}(x) = \hat{z}E_0 \cos k_0x \cos \omega t$ with \hat{z} the polarization direction and $k_0 = 2\pi/\lambda$, where λ is the laser wavelength. Classically the dipole force is given by the gradient of the optical field $\frac{d\mathbf{p}}{dt} = -\nabla V$, where $V = -\mathbf{d} \cdot \mathbf{E}$. Quantum mechanically, this corresponds to $\left\langle \frac{d\mathbf{p}}{dt} \right\rangle = -\text{tr}(\rho \nabla V) = -\hat{x}k_0 \sin k_0x \overline{2\text{Re}(\rho_{12}E_0 \langle 2|d|1 \rangle)}$, where ρ is the density matrix and the overline denotes a time average under the rotating wave approximation. For a stationary state we can use a standard quantum optics approach (see e.g. [38]), assuming the amplitude of the coherence term ρ_{12} is slowly varying in the rotating frame with the laser frequency. We obtain $\rho_{12}E_0 \langle 2|d|1 \rangle = \hbar e^{i\omega t} \frac{i\Omega_0 \cos k_0x}{i\delta + \Gamma/2} \left[\frac{1}{2(1+s)} \right]$, where $s = \frac{1}{2} \frac{\Omega_0^2 \cos^2 k_0x}{\delta^2 + (\Gamma/2)^2}$, the Rabi frequency $\Omega_0 \equiv \frac{\langle 2|d|1 \rangle E_0}{\hbar}$, and Γ is the decay rate due to spontaneous emissions and collision losses ($\Gamma \ll \delta$). Typically the detuning $\delta \equiv \omega - \omega_0$ is much greater than the Rabi frequency Ω_0 so that s is negligible as well as Γ . The force is then given by

$$\left\langle \frac{d\mathbf{p}}{dt} \right\rangle = \hat{x} \hbar k_0 \delta \sin 2k_0x \frac{\Omega_0^2}{2\delta^2}. \quad (1.2)$$

Note that the force flips sign as the detuning does. Atoms being blue (red) detuned, $\delta > 0$ ($\delta < 0$), are pushed towards the nodes (anti-nodes) of the laser field. This

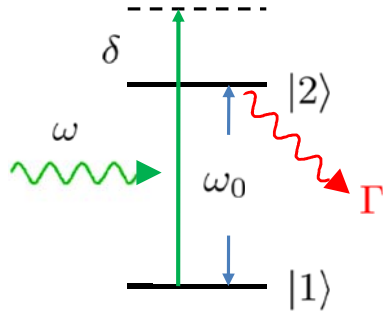


Figure 1.3: Two-level configuration for a neutral atom interacting with the laser field. In this illustration the spontaneous emission is neglected.

force is conservative, so that a potential can be defined by

$$V = -\hbar\delta\frac{\Omega_0^2}{2\delta^2}\sin^2 k_0x. \quad (1.3)$$

We have also assumed that the Doppler broadening has negligible effects, which is justified by the fact that the speed of atoms is much smaller than δ/k_0 . Otherwise, a dissipative part of the optical force arises and this mechanism contributes to so-called Doppler cooling.

As more laser beams are applied in perpendicular directions, an egg crate-shaped lattice is formed. More complicated lattices such as triangular and hexagonal ones can be formed by adjusting the axial directions of the standing waves. Further, one can increase the lattice depth along a certain direction to shut down the tunneling so that atoms can only be confined in a tube or a layer structure. This provides an ideal platform for studying the effects of dimension [9, 12, 39, 40].

Hubbard Model – Here we give a brief derivation of the famous Hubbard model, an approximation proposed by J. Hubbard to describe the physics of conduction and insulation behaviors in metals or crystals [41]. From the previous discussion we learn that in an optical lattice the periodic barrier can be described by

$$V_{op}(x) = V_0\sin^2\frac{\pi}{d}x, \quad (1.4)$$

where V_0 is the lattice depth and $d = \lambda/2$ the lattice constant. The Hamiltonian in the second quantization form reads

$$H = \int dx \psi^\dagger(x) \left[\frac{p^2}{2m} + V_{op}(x) \right] \psi^\dagger(x) + U_0 \int dx \psi^\dagger(x) \psi^\dagger(x) \psi(x) \psi(x), \quad (1.5)$$

where $\psi(x)$ is the field operator and $U_0 = \frac{4\pi\hbar^2 a}{m}$ accounts for the interaction between particles. Without the interaction, the periodic potential suggests that one make use of the Bloch state basis $\phi_{m,k}$ (k the crystal momentum and m the band index) and a set of the Wannier functions can be constructed from it. We then rewrite the field operator as $\psi(x) = \sum_{m,R} a_{m,R} w_{m,R}(x)$, where $w_{m,R}$ is the m^{th} band Wannier function centered at the site $R = nd$ (n an integer) and $a_{m,R}$ is the particle destruction operator. Note that by definition $w_{m,R} = \frac{1}{\sqrt{N}} \sum_{k \in BZ} e^{-ikR} \phi_{m,k}(x)$ (BZ denotes the first Brillouin zone). Then in the Hamiltonian (1.5) the non-interacting term $H_0 = \frac{p^2}{2m} + V_{op}$ becomes

$$\begin{aligned} H_0 &\rightarrow \sum_{m,m',R,R'} a_{m,R}^\dagger a_{m',R'} \frac{1}{N} \sum_{k,k' \in BZ} e^{ikR - ik'R'} \int dx \phi_{m,k}^*(x) H_0 \phi_{m',k'}(x) \\ &= \sum_{R,R'} a_{m,R}^\dagger a_{m,R} \frac{1}{N} \sum_k \epsilon_{m,k} e^{ik(R-R')}, \end{aligned} \quad (1.6)$$

where we have used the fact that $\int dx \phi_{m,k}^*(x) H_0 \phi_{m',k'}(x) = \epsilon_{m,k} \delta_{m,m'} \delta_{k,k'}$ with $\epsilon_{m,k}$ the eigen-spectrum of the m^{th} band.

Under certain circumstances suggested by current experiments [42–44], a simplification can be made by only taking the lowest band into consideration if higher band excitations are negligibly populated. This should be the case when (1) the gas is dilute so that the first band is not fully occupied, (2) the particle interaction is well separated from the energy bandgap, and (3) the thermal fluctuation is unable to excite population to higher bands. This first-band approximation will be used in our discussion below, and the indexing subscript m will be dropped hereafter.

Normally ϵ_k is obtained exactly by numerically solving the matrix elements of H_0 through diagonalization. However we can make a guess for the form of ϵ_k . We recall that k is the crystal momentum and therefore $\epsilon_k = \epsilon_{k+2\pi/d}$, which is supposed to be an even function. Keeping only the lowest order of the Fourier components $\epsilon_k \simeq -t \cos kd$, we get $H_0 \rightarrow -t \sum_R a_R^\dagger a_{R+1}$. This term describes a particle transferring from one site to its neighbor, a process called hopping, with energy lowered by $-t$. This guess turns out to be a fairly good approximation when compared to the numerical evaluation of ϵ_k .

The interaction term then becomes $H_1 = U \sum_R a_R^\dagger a_R^\dagger a_R a_R$ with $U = U_0 \int dx |w(x)|^4$. Here we have used the fact that the Wannier function is relatively localized so that the off-site contribution can be neglected. Combining the hopping term and the interaction yields the Hubbard model:

$$H = -t \sum_R a_R^\dagger a_{R+1} + U \sum_R a_R^\dagger a_R^\dagger a_R a_R. \quad (1.7)$$

As mentioned earlier, the Hubbard model was originally proposed to describe electron transport behaviors in solids. It shows very rich phases and has been intensively studied in the context of optical lattices both for fermions and bosons [7, 8, 42, 45]. Many studies have been made focusing on the superfluid (SF) to Mott insulator (MI) transition. At zero temperature, general features suggest that the particles condense and show superfluidity when the hopping term dominates the on-site interaction; once the interaction is much stronger, the tunneling to other sites is turned off so that each site contains only an integer number of particles, corresponding to a special insulating phase called a Mott insulator [46]. Because any experimental investigation of this system must be performed at a finite temperature, the identification of a superfluid in an optical lattice is an essential step to distinguish different phases [44, 47–49]. This is normally done by time-of-flight spectroscopy. A detailed

discussion on the time-of-flight interference patterns will be presented in Chapter IV.

1.2.3 Quantum computation and simulation with trapped ions

Ultracold neutral atoms are usually considered as an ensemble rather than individually. Because the overall Hilbert space is extremely high-dimensional, any relevant quantity, or “information” from the quantum-computing point of view, is usually treated as a continuous variable. Ions, on the contrary, can be well separated from each other due to their Coulomb interaction, and hence can be conveniently manipulated individually. They are easily stabilized in space by electrical methods and have stronger coupling through collective vibrations. For each ion, two of the electronic hyperfine states can be effectively employed as a two-level system, called a quantum bit (qubit). Meanwhile the vibrational modes, when coupled to the qubit degree of freedom by optical means, serve as a “quantum bus” that entangles distant information. Such systems provide a “digitized” version of Hilbert space for quantum information and simulation purposes. Note that any arbitrary Hamiltonian can be “digitized” to a series of fundamental k -local operations in an asymptotic sense [50, 51]. An important issue is to reach a sufficiently high fidelity while performing universal quantum gate operation. The study of the required fidelity in quantum computation is known as quantum error correction theory (see, e.g., [52]).

Ions can be contained in a varying electrical field such as a radio-frequency (RF) trap. A so-called Paul trap, which is commonly used to confine a one-dimensional ion array, typically consists of two RF wires providing transverse confinement and segmental-structured DC electrodes, in parallel with the RF wires, providing axial trapping. When ions are cooled and then stabilized around their equilibrium, small vibrations can be expected at a finite temperature and can be decomposed into the canonical normal modes.

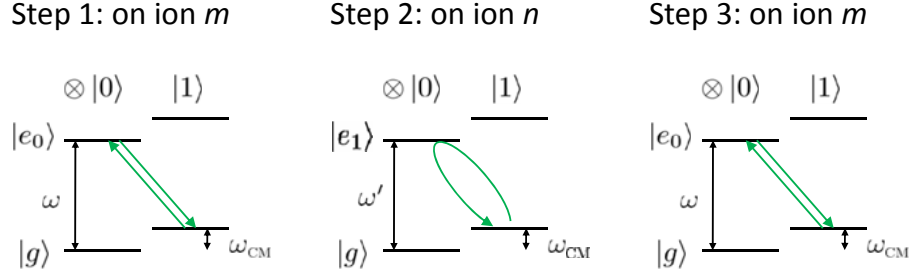


Figure 1.4: Graphical representation for a Cirac-Zoller gate.

The first proposal of a trapped ion quantum gate was by J. I. Cirac and P. Zoller in 1995 [53]. The concept is summarized as follows. Consider a trapped ion array on which individual ions can be addressed by laser beams. Suppose the qubit is encoded into two hyperfine levels $|g\rangle$ and $|e_0\rangle$ for each ion, and then the motional modes define a series of sidebands $|\text{qubit}\rangle \otimes \prod_k |n_k\rangle$ with $n_k = 0, 1, 2, \dots$ as the phonon number of the k th mode. For this protocol to work, every motional mode has to be pre-cooled to the ground state and only the center-of-mass (CM) mode will be excited by the laser beam. When the beam acting on the m th ion is turned on with its frequency detuned by $\delta = -\omega_{CM}$ from the spacing ω , a π pulse causes the populations in states $|g\rangle_m|1\rangle$ and $|e_0\rangle_m|0\rangle$ (where $|0\rangle$ and $|1\rangle$ refer to the Fock basis of the CM mode) to be inverted, leaving other states unaltered (Fig. 1.4, Step 1). A second similar procedure is applied to the n th ion except that the laser couples the state $|g\rangle_n|1\rangle$ to an auxiliary excited state $|e_1\rangle_n|0\rangle$. This can be done for example by using differently polarized lights to selectively couple different excited states. This procedure does not involve the states $|g\rangle_n|0\rangle$ and $|e_1\rangle_n|1\rangle$ (so they will be unchanged) but will cause a sign difference in the overall state of the two ions and the phonon depending on whether or not $|g\rangle_n|1\rangle$ is populated (Fig. 1.4, Step 2). A final step is to apply Step 1 again to the m th ion (Fig. 1.4, Step 3). This step destroys a phonon if any has been created during previous steps and restores the

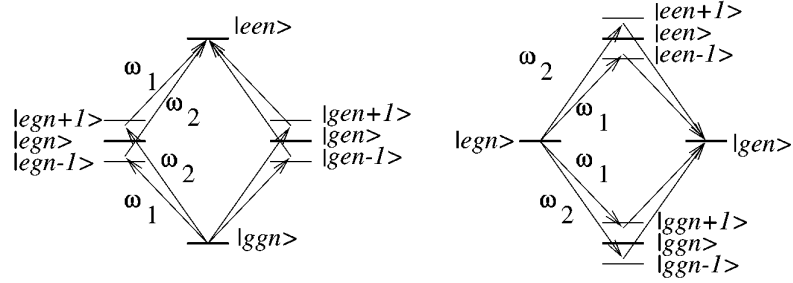


Figure 1.5: Graphical representation for a Sørensen-Mølmer gate. A bichromatic field is applied with two frequencies summed up to $2\omega_{eg}$. Because both frequencies are detuned off the energy levels, the transitions occur only when two photons are absorbed or emitted. Different paths interfere with each other and eliminate the dependence of phonon population. (Figure from [55].)

system back to the motional ground state. We explicitly show the overall operation as follows (see [53] Eq. (3)):

$$\begin{array}{ccccccc}
 & & \text{I} & & \text{II} & & \text{III} \\
 |g\rangle_m |g\rangle_n |0\rangle & \rightarrow & |g\rangle_m |g\rangle_n |0\rangle & \rightarrow & |g\rangle_m |g\rangle_n |0\rangle & \rightarrow & |g\rangle_m |g\rangle_n |0\rangle \\
 |g\rangle_m |e_0\rangle_n |0\rangle & \rightarrow & |g\rangle_m |e_0\rangle_n |0\rangle & \rightarrow & |g\rangle_m |e_0\rangle_n |0\rangle & \rightarrow & |g\rangle_m |e_0\rangle_n |0\rangle \\
 |e_0\rangle_m |g\rangle_n |0\rangle & \rightarrow & -i|g\rangle_m |g\rangle_n |1\rangle & \rightarrow & i|g\rangle_m |g\rangle_n |1\rangle & \rightarrow & |e_0\rangle_m |g\rangle_n |0\rangle \\
 |e_0\rangle_m |e_0\rangle_n |0\rangle & \rightarrow & -i|g\rangle_m |e_0\rangle_n |1\rangle & \rightarrow & -i|g\rangle_m |e_0\rangle_n |1\rangle & \rightarrow & -|e_0\rangle_m |e_0\rangle_n |0\rangle.
 \end{array} \tag{1.8}$$

This exactly corresponds to a Controlled-Phase-Flip (CPF) gate. This Cirac-Zoller gate, however, is sensitive to the temperature because it requires the ground state of the “quantum bus” motional mode. The “quantum bus” sideband must be resolved from other modes, requiring a certain amount of time and hence setting a speed limit to gate operations. Further, the gate must operate in the Lamb-Dicke regime $\eta \ll 1$, characterized by the Lamb-Dicke parameter $\eta \sim \sqrt{\hbar/(m\omega_{CM})}/\lambda$ where λ is the laser field wavelength; otherwise the needed laser intensity (Rabi frequency) will depend on the noisy motional state and result in decoherence.

In 1999, A. Sørensen and K. Mølmer proposed a two-qubit gate [54, 55] based on

a bichromatic field with frequencies $\omega_1 = \omega_{eg} - (\nu - \delta)$ and $\omega_2 = \omega_{eg} + (\nu - \delta)$, tuned close to the red and blue sidebands of a resolvable motional mode ν , respectively. As shown in Fig. 1.5, because every laser field is detuned far from those levels, only two photon processes have significant contributions. In the weak-field coupling limit (n only changing by 1), one can achieve [54]

$$\begin{aligned}
 |gg\rangle &\rightarrow \cos\theta|gg\rangle + i\sin\theta|ee\rangle \\
 |ee\rangle &\rightarrow \cos\theta|ee\rangle + i\sin\theta|gg\rangle \\
 |ge\rangle &\rightarrow \cos\theta|ge\rangle - i\sin\theta|eg\rangle \\
 |eg\rangle &\rightarrow \cos\theta|eg\rangle - i\sin\theta|ge\rangle.
 \end{aligned} \tag{1.9}$$

This can be transformed to a CPF gate up to single-qubit phase shifts when $\theta = \pi/4$. Here $\theta \equiv \tilde{\Omega}\tau/2$ with τ the gate operation time and $\tilde{\Omega} \equiv -\frac{(\Omega\eta)^2}{2\delta}$ with the Rabi frequency Ω and the Lamb-Dicke parameter η . Note that $\tilde{\Omega}$ is independent of the phonon number n shown in Fig. 1.5. This is due to a cancellation of phonon dependence that occurs when the paths indicated in the left panel of Fig. 1.5 interfere with each other, eliminating the ground-state requirement of the “quantum bus” mode. The Sørensen-Mølmer scheme can be formulated in a general field coupling case without restricting $\Delta n = \pm 1$, and understood as one of quantum gates utilizing the geometrical phase [56]. A similar idea was proposed independently by G. Milburn *et al.* in 2000 [57], in which a state-dependent force was applied to the qubits; the force displaced a qubit in the (motional) momentum/coordinate phase space and followed a closed loop back to the original situation. An additional (geometrical) phase was gained proportional to the area enclosed by the state-dependent loop. The above schemes still need to operate on a single “quantum bus” mode and hence restrict the gate speed. Several proposals have been made using fast pulses [58, 59] and faster transverse modes with pulse shaping techniques [60, 61].

Although trapped-ion quantum gates have been demonstrated, constituting a fundamental step for arbitrary “digital” quantum simulation, trapped ion systems are intrinsically suitable for spin model quantum simulation. The two-qubit gate is closely related to the Ising-type interaction $H \sim \Theta_{ij} \sigma_i^z \otimes \sigma_j^z$, where the Pauli matrix σ_i^z represents the i th spin and the coupling Θ_{ij} can be controlled for example through the state-dependent force in Milburn’s scheme [57, 62–64]. With more sophisticated laser arrangement, Heisenberg-type interaction can also be realized [62, 65]. A complete-graph network with Ising-type interaction is generated by simply shining a laser field on the ions all together. In this case, the applied laser detuning determines the strength of coupling between every pair of spins. Further, one can simulate an external field by adding a magnetization term $B_i \vec{\sigma}_i$, which can be effectively done through direct rotation of each ion’s internal state. This line of research provides a natural way to study fundamental quantum many-body problems such as Ising and Heisenberg models, which quickly become intractable to classical computing as the size grows.

1.3 Thesis Outline

This thesis consists of several studies of quantum many-body systems with ultracold atoms and trapped ions. The structure is outlined as follows.

In Chapter II, we consider an ultracold Fermi gas with population and mass imbalance between two spin species through a Feshbach resonance. The crossover behavior from the BEC to the BCS side is studied. We map out the phase diagrams in a potential trap, and find a shell structure formed by superfluid and different normal-phase layers. To provide a qualitative description for the shell structure, we calculate the in-trap population density profiles. The work presented in this chapter

is published in [66].

In Chapter III, we study the BEC-BCS crossover for a quasi-two-dimensional Fermi gas confined in a layer formed by an optical lattice across a wide Feshbach resonance. We consider two effective two-dimensional models within the mean-field level, and calculate the zero-temperature cloud size and population density profiles. The first single-channel model, using a lowest-band approximation and neglecting the molecular degree of freedom, predicts a constant cloud size for arbitrary interaction. The second two-channel model, taking the point of view that multiple-band excitations dress the effective interaction so that dressed molecules are allowed to form, shows a decrease in the cloud size from the BCS to BEC side. This qualitative discrepancy between the two models indicates that the inclusion of dressed molecules is essential for a mean-field description of quasi-two-dimensional Fermi systems, especially on the BEC side of the Feshbach resonance. The work presented in this chapter is published in [67].

Chapter IV discusses ultracold bosons in an optical lattice. We study finite temperature behaviors across the normal-superfluid transitions, for both noninteracting and strongly interacting cases. To make direct comparison with experimental outcomes of time-of-flight imaging, we calculate the momentum-space density profiles of a condensate on top of thermal contributions, including the consideration of a global harmonic trap. We show that the appearance of a clear bimodal distribution in the interference patterns sets a qualitative and universal signature for the onset of BEC. Further, the momentum distribution can also be applied to extract the condensate fraction, which may serve as a promising thermometer in such a system. The work presented in this chapter is published in [49, 68].

In Chapter V, we propose a large-scale quantum computer architecture by sta-

bilizing a large linear ion chain in a very simple trap geometry. By confining ions in an anharmonic linear trap with nearly uniform spacing between ions, we show that high-fidelity quantum gates can be realized in large linear ion crystals under the Doppler temperature based on coupling to a near-continuum of transverse motional modes with simple shaped laser pulses. The work presented in this chapter is published in [69].

In Chapter VI, we discuss a quantum Ising-magnet emulator based on trapped ions. The Ising-type network can be built by applying a bichromatic laser field with a frequency beatnote detuning. We investigate the phases of ground spin configurations for small systems by scanning the detuning through motional modes and increasing the effective external field. We demonstrate even for small systems, the trapped ion Ising network shows rich competing phases. For three ions, we present nearly-adiabatic time evolution calculations and discuss close connections between frustration and entanglement. Part of the work on three-ion calculations presented in this chapter is included in a recent paper [70] submitted for publication.

CHAPTER II

Ultracold Fermi Gas with Spin Population and Mass Imbalance

2.1 Overview

Recent advances in understanding the degenerate Fermi gas have raised strong interest in population imbalance of two spin species [26–32, 34, 35, 71–78]. The experiments suggest a phase separation picture with a superfluid core surrounded by a shell of normal gas [27–29, 32]. This picture has been confirmed by a number of theoretical calculations of the atomic density profiles in the trap [30, 71–78]. Feshbach resonances between different atomic species with unequal mass have been reported in a Bose-Fermi mixture [79, 80] and in a Fermi-Fermi mixture [81–84], motivating study of a strongly interacting Fermi gas with both mass and population imbalance between the two components. There has been a considerable amount of theoretical work in this direction [66, 85–93].

As part of these contributions, our work investigates the properties of a trapped strongly interacting Fermi gas with mass and population imbalance. We map out its zero temperature phase diagram in a harmonic trap (generally anisotropic) as a function of a few universal parameters. Compared with the equal-mass case, the two-species Fermi mixture (${}^6\text{Li}$ - ${}^{40}\text{K}$ mixture for instance) shows a very different picture of phase separation: it supports a superfluid shell state in the intermediate trap

region, with normal gases of different characters filling the center and the edge of the trap. This unusual phase separation picture with non-monotonic superfluid order parameter in space only occurs for trapped fermions with unequal mass. We provide an intuitive explanation for the phenomenon, and show how to detect it by measuring the atomic density profiles. This superfluid shell state is not simply connected in space, so it may support interesting vortex structure under rotation of the trap.

The structure of this chapter is outlined as follows. In Sec. 2.2 we briefly summarize the formalism for describing an ultracold Fermi gas, where a two-channel model and a simplified single-channel model are discussed. We adapt our formalism to include the trap effect, and then generalize our discussion by considering population and mass imbalance. In Sec. 2.3 we show the calculated phase diagrams and in-trap density profiles. For the shell structure of various phases we also present a qualitative explanation.

2.2 Formalism

2.2.1 Basic Hamiltonian: two-channel model

To describe a Fermi gas near a Feshbach resonance, the Hamiltonian should include contributions from both open and closed channels, and is thus called a two-channel model. Explicitly, it is given by [94, 95]

$$\begin{aligned}
H - \mu N &= \sum_{\sigma, \mathbf{k}} (\epsilon_{\mathbf{k}} - \mu) a_{\mathbf{k}, \sigma}^{\dagger} a_{\mathbf{k}, \sigma} + \sum_{\mathbf{q}} (\gamma + \epsilon_{\mathbf{q}}/2 - 2\mu) b_{\mathbf{q}}^{\dagger} b_{\mathbf{q}} \\
&+ \left(g/\sqrt{\mathcal{V}} \right) \sum_{\mathbf{k}, \mathbf{q}} (b_{\mathbf{q}}^{\dagger} a_{-\mathbf{k}+\mathbf{q}/2, \uparrow} a_{\mathbf{k}+\mathbf{q}/2, \downarrow} + \text{h.c.}) \\
&+ \left(U/\mathcal{V} \right) \sum_{\mathbf{k}, \mathbf{k}', \mathbf{q}} a_{\mathbf{k}+\mathbf{q}/2, \uparrow}^{\dagger} a_{-\mathbf{k}+\mathbf{q}/2, \downarrow}^{\dagger} a_{-\mathbf{k}'+\mathbf{q}/2, \downarrow} a_{\mathbf{k}'+\mathbf{q}/2, \uparrow},
\end{aligned} \tag{2.1}$$

where $\epsilon_{\mathbf{k}} \equiv \frac{\hbar k^2}{2m}$ is the kinetic energy, μ is the chemical potential, and $a_{\mathbf{k}, \sigma}$ ($b_{\mathbf{q}}$) are the annihilation operators of the open channel fermions (the closed channel molecules)

with \mathbf{k} (\mathbf{q}) the momentum of the atom (molecule) and $\sigma = \uparrow, \downarrow$ denoting the atomic hyperfine states, i.e. spins. Here $N = \sum_{\sigma, \mathbf{k}} a_{\mathbf{k}, \sigma}^\dagger a_{\mathbf{k}, \sigma} + 2 \sum_{\mathbf{q}} b_{\mathbf{q}}^\dagger b_{\mathbf{q}}$ is the total number of atoms, \mathcal{V} is the quantization volume, γ is the bare detuning determined by the magnetic field offset from the resonance point, g is the bare atom-molecule coupling rate accounting for the mixing of two channels, and the bare scattering rate U accounts for the interaction of atoms. However, we encounter a so-called ultraviolet divergence problem when dealing with the atom-atom interaction due to its spatial δ -function behavior. We need the three bare parameters to be renormalized to the physical quantities U_p, g_p, γ_p . They are related through the standard renormalization relations: $U = \Gamma U_p, g = \Gamma g_p, \gamma = \gamma_p - \Gamma g_p^2 / U_c$, where $\Gamma \equiv (1 + U_p / U_c)^{-1}$ with $U_c \equiv -\mathcal{V}^{-1} \sum_{\mathbf{k}} (2\epsilon_{\mathbf{k}})^{-1}$, $U_p = 4\pi\hbar^2 a_{bg} / m$, $g_p^2 = 4\pi\hbar^2 a_{bg} W \mu_{co} / m$, and $\gamma_p = \mu_{co}(B - B_0)$; μ_{co} is the magnetic moment difference between the two channels; a_{bg} is the background scattering length; W is the resonance width; B_0 represents the resonance point (see Eq. (1.1)).

2.2.2 Single-channel model

Several works have shown that the two-channel model can be characterized by a dimensionless parameter [33, 96]:

$$\bar{\gamma} \equiv \frac{m a_{bg}^2 W^2 \mu_{co}^2}{E_F}. \quad (2.2)$$

When $\bar{\gamma}$ is large ($\gg 1$, called wide-resonance), in accordance with current experiments with ${}^6\text{Li}$ and ${}^{40}\text{K}$, the closed channel population is negligible. Therefore, after adiabatic elimination of the molecular modes $b_{\mathbf{q}}$, the Hamiltonian can be greatly simplified to a single-channel model [96–100]

$$H - \mu N = \sum_{\sigma, \mathbf{k}} (\epsilon_{\mathbf{k}} - \mu) a_{\mathbf{k}, \sigma}^\dagger a_{\mathbf{k}, \sigma} + \left(U_{\text{eff}} / \mathcal{V} \right) \sum_{\mathbf{k}, \mathbf{k}', \mathbf{q}} a_{\mathbf{k}+\mathbf{q}/2, \uparrow}^\dagger a_{-\mathbf{k}+\mathbf{q}/2, \downarrow}^\dagger a_{-\mathbf{k}'+\mathbf{q}/2, \downarrow} a_{\mathbf{k}'+\mathbf{q}/2, \uparrow} \quad (2.3)$$

with modified parameters: $U_{\text{eff}} = U_s(1 + U_s/U_c)^{-1}$ where $U_s = 4\pi\hbar^2 a_s/m$ with $a_s = a_{bg}(1 - \frac{W}{B-B_0})$, and $N = \sum_{\mathbf{k},\sigma} a_{\mathbf{k},\sigma}^\dagger a_{\mathbf{k},\sigma}$.

2.2.3 Effects of traps and the local-density approximation

The above Hamiltonians (2.1) and (2.3) do not explicitly include consideration of external potentials. In a real experimental setup, particles are always contained in a global trap. The overall wavefunction must be modified by the spatial variation of the potential, complicating the analysis. Therefore, we adopt a semi-classical point of view, called the Thomas-Fermi approximation or the local-density approximation (LDA), to give a qualitative and approximate quantitative description accounting for the trap effect. The LDA treats every local portion (sub-system) of the entire system as a uniform gas characterized by a local chemical potential $\mu(\mathbf{r})$. Note that when a small number of particles δn is added to the sub-system associated with a local chemical potential $\mu(\mathbf{r})$, the energy gain is $\delta E = [\mu(\mathbf{r}) + V(\mathbf{r})]\delta n$. At equilibrium $\delta E/\delta n = 0$, yielding $\mu(\mathbf{r}) = \mu(\mathbf{r}_0) - V(\mathbf{r})$ with \mathbf{r}_0 the coordinate of the potential reference. This approximation is valid as long as the relevant energy scale set by the chemical potential is much greater than the potential variation, a criterion satisfied by most current experimental situations of interest. For a harmonic trap with frequency ω , this criterion means $\mu(\mathbf{r}_0) \gg \hbar\omega$ [101]. Then the number density $n(\mathbf{r})$ can be locally determined by only a single parameter $\mu(\mathbf{r}_0)$ but must satisfy the overall number constraint $N = \int d^d \mathbf{r} n(\mathbf{r})$ (the superscript $d = 3$ denotes the dimension for our present case).

From the LDA point of view, the role played by the trap is nothing but a spatial “display” of phases of the corresponding chemical potential $\mu(\mathbf{r})$. If different phases are observed within a range of μ accessible to a particular experimental condition, there must be a shell structure in space in three dimensional cases. In reality, the

clear interface between two distinct phases will be rounded off for a finite-sized system when the surface energy is considered.

2.2.4 Fermi gases with population and mass imbalance

Here we present a description of a Fermi gas that includes both population and mass imbalance between two species. The results should apply to a fermion-fermion mixture, e.g., a ${}^6\text{Li}$ - ${}^{40}\text{K}$ gas. Here we only consider the case where the heavy atoms carry one spin and the light atoms carry the opposite. For simplicity, we also assume that the resonance is wide so that a strongly interacting Fermi gas can be described by the the single-channel Hamiltonian (c.f. Eq. (2.3)):

$$\begin{aligned}
H &= \sum_{\mathbf{k},\sigma} (\epsilon_{\mathbf{k}\sigma} - \mu_\sigma) a_{\mathbf{k},\sigma}^\dagger a_{\mathbf{k},\sigma} \\
&+ \left(U_{\text{eff}}/\mathcal{V} \right) \sum_{\mathbf{q},\mathbf{k},\mathbf{k}'} a_{\mathbf{q}/2+\mathbf{k},\uparrow}^\dagger a_{\mathbf{q}/2-\mathbf{k},\downarrow}^\dagger a_{\mathbf{q}/2-\mathbf{k}',\downarrow} a_{\mathbf{q}/2+\mathbf{k}',\uparrow}
\end{aligned} \tag{2.4}$$

where $\epsilon_{\mathbf{k}\sigma} = \mathbf{k}^2/(2m_\sigma)$ with m_σ denoting the mass of species σ ($\hbar = 1$), \mathcal{V} is the quantization volume, and $a_{\mathbf{k},\sigma}^\dagger$ is the fermionic creation operator for the (\mathbf{k}, σ) mode. The effective atom-atom interaction rate U_{eff} is determined by the scattering length a_s through $1/U_{\text{eff}} = 1/U_s - \mathcal{V}^{-1} \sum_{\mathbf{k}} 1/(2\epsilon_{\mathbf{k}})$ with $U_s = 4\pi a_s/(2m_r)$ ($m_r = m_\uparrow m_\downarrow/(m_\uparrow + m_\downarrow)$ is the reduced mass). Under the LDA, $\mu_\uparrow = \mu_{\mathbf{r}} + h$, $\mu_\downarrow = \mu_{\mathbf{r}} - h$, $\mu_{\mathbf{r}} = \mu - V(\mathbf{r})$, where $V(\mathbf{r}) = \sum_{i=x,y,z} \beta_i \mathbf{r}_i^2/2$ is the harmonic trapping potential, which, without loss of generality, has been assumed to be the same for the two components. The chemical potential μ at the trap center and the chemical potential imbalance h are determined from the total atom number $N = N_\uparrow + N_\downarrow$ and the population imbalance $p = (N_\uparrow - N_\downarrow)/N$ through number equations given below.

From the mean-field approach, we set $\Delta \equiv \mathcal{V}^{-1} \sum_{\mathbf{k},\mathbf{q}} \langle a_{\mathbf{q}/2-\mathbf{k},\downarrow} a_{\mathbf{q}/2+\mathbf{k},\uparrow} \rangle \delta_{\mathbf{q}0}$, and hence the second term in the Hamiltonian (2.4) becomes $U_{\text{eff}} \left[\sum_{\mathbf{k}} (\Delta a_{\mathbf{k}}^\dagger a_{\mathbf{k}}^\dagger + \text{h.c.}) - \mathcal{V} |\Delta|^2 \right]$, allowing the Hamiltonian (2.4) to be diagonalized. In this formalism, we

neglect the FFLO state with condensation at non-zero pair momenta. (The FFLO state can be stabilized only within a narrow parameter region on the BCS side [31, 35].) The thermodynamic potential $\Omega = -T \ln[\text{tr}(e^{-H/T})]$ at the temperature T can be written as [71, 72]

$$\begin{aligned} \Omega = & -\mathcal{V}|\Delta|^2/U_{\text{eff}} + \sum_{\mathbf{k}} [\epsilon_{\mathbf{k}r} - \mu_{\mathbf{r}} - E_{\mathbf{k}}] \\ & -T \sum_{\mathbf{k}} \ln [(1 + e^{-E_{\mathbf{k}\uparrow}/T}) (1 + e^{-E_{\mathbf{k}\downarrow}/T})] \end{aligned} \quad (2.5)$$

where $E_{\mathbf{k}\uparrow,\downarrow} = E_{\mathbf{k}} \mp (h + \alpha\epsilon_{\mathbf{k}r})$ with $E_{\mathbf{k}} \equiv \sqrt{(\epsilon_{\mathbf{k}r} - \mu_{\mathbf{r}})^2 + \Delta^2}$, $\epsilon_{\mathbf{k}r} \equiv \mathbf{k}^2/(4m_r)$, and $\alpha \equiv (m_{\uparrow} - m_{\downarrow})/(m_{\uparrow} + m_{\downarrow})$.

In the case with balanced populations and masses for both spins, i.e. $h = 0$ and $\alpha = 0$, and in homogeneous space with μ constant, we recover the conventional BCS theory and can identify Δ as the excitation energy gap. The minimum of Ω can be found by solving $\partial\Omega/\partial\Delta = 0$, which leads to the famous gap equation:

$$\frac{1}{U_{\text{eff}}} = -\frac{1}{\mathcal{V}} \sum_{\mathbf{k}} \frac{1 - 2f(E_{\mathbf{k}})}{2E_{\mathbf{k}}}, \quad (2.6)$$

where the Fermi distribution $f(E) \equiv 1/(1 + e^{E/T})$.

Instead of taking the gap equation approach, we search for the global minimum of the thermodynamical potential Ω with respect to the variational parameter Δ . The reason is that with more complexity added to the question by traps and spin/mass mismatch, $\partial\Omega/\partial\Delta = 0$ does not necessarily correspond to a global minimum but also can be an unstable fixed point or a metastable state [71, 72]. The values of μ and h are determined from the two number equations $N_{\sigma} = \int d^3\mathbf{r} n_{\mathbf{r}\sigma}$ integrated over the trap. The local atomic density $n_{\mathbf{r}\sigma}$, derived from the thermodynamic potential Ω as $\partial\Omega/\partial\mu_{\sigma} = -n_{\mathbf{r}\sigma}\mathcal{V}$, has the expression

$$n_{\mathbf{r}\sigma} = \frac{1}{\mathcal{V}} \sum_{\mathbf{k}} [u_{\mathbf{k}}^2 f(E_{\mathbf{k},\sigma}) + v_{\mathbf{k}}^2 f(-E_{\mathbf{k},-\sigma})], \quad (2.7)$$

where the parameters $u_{\mathbf{k}}^2 = (E_{\mathbf{k}} + (\epsilon_{\mathbf{k}r} - \mu_r))/(2E_{\mathbf{k}})$, $v_{\mathbf{k}}^2 = (E_{\mathbf{k}} - (\epsilon_{\mathbf{k}r} - \mu_r))/(2E_{\mathbf{k}})$. The above mean-field formalism is also identical to the G_0G diagram scheme if we interpret Δ at finite temperature as the total gap including contributions from both the order parameter and the pseudogap associated with the pair fluctuations [71, 72, 78].

If one of the energies $E_{\pm, \mathbf{k}}$ has one or two zero(s) in \mathbf{k} -space, it signals the presence of the type-I or type-II breached-pair (Sarma) states [31, 34, 35, 71, 72, 102] (called the BP1 or BP2 states, respectively). The BP states represent a spatially homogeneous superfluid, but they differ from the conventional BCS states by a phase separation in the momentum space and by a topological change of the Fermi surface for the excess fermions.

2.3 Results and Discussion

We calculate the phase diagram of the trapped fermions in terms of several dimensionless universal parameters. For that purpose, the unit of energy is chosen to be the Fermi energy E_F at the center of the trap for N non-interacting fermions with an effective mass of $2m_r$ and with equal population for the two components. Under the LDA, one finds $E_F = (3N\sqrt{\beta_x\beta_y\beta_z})^{1/3}/\sqrt{2m_r}$ from this definition. The trapping potential $V(\mathbf{r})$ has the dimensionless form $V(\mathbf{r})/E_F = \sum_i \tilde{r}_i^2$, where the normalized coordinates $\tilde{r}_i \equiv r_i/R_i$ and $R_i \equiv \sqrt{2E_F/\beta_i}$ is the Thomas-Fermi radius along the i th direction. The momentum \mathbf{k} and the temperature T are measured in the units of $k_F \equiv \sqrt{2(2m_r)E_F}$ and $T_F \equiv E_F/k_B$, respectively. The system properties then only depend on four dimensionless parameters $k_F a_s$, T/T_F , the population imbalance p , and the mass mismatch α . In the following calculation, we take $\alpha = 0.74$ corresponding to the ${}^6\text{Li}$ - ${}^{40}\text{K}$ mixture. In a typical configuration with the atom number

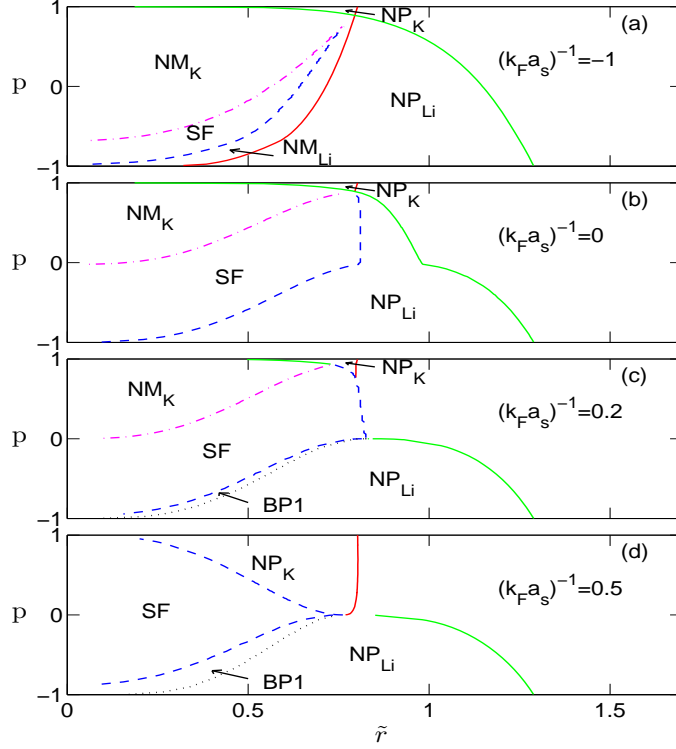


Figure 2.1: The zero temperature phase diagrams for trapped ${}^6\text{Li}$ - ${}^{40}\text{K}$ mixture near a Feshbach resonance. The phases include the BCS superfluid state (SF), the breached pair phase of type 1 (BP1), the normal mixture (NM_K or NM_{Li} , with ${}^{40}\text{K}$ or ${}^6\text{Li}$ in excess, respectively), and the normal polarized (single-component) states (NP_K or NP_{Li}). The phases are shown versus the population imbalance p and the normalized trap radius \tilde{r} .

$N = 5 \times 10^6$, $\beta_x/\hbar = \beta_y/\hbar = 49.6 \text{ Hz}/\mu\text{m}^2$, and $\beta_z/\hbar = 1.95 \text{ Hz}/\mu\text{m}^2$ [29], the above units have the values $T_F = 604 \text{ nK}$, $k_F = 5.09 \mu\text{m}^{-1}$, $R_x = R_y = 56.5 \mu\text{m}$ and $R_z = 285 \mu\text{m}$.

In Fig. 2.1, we map out the zero-temperature phase diagrams for trapped fermions as a function of the population imbalance p at several characteristic interaction strengths $k_F a_s$. The system shows a rich picture of phase separation in the trap. First, on the BCS side of resonance with $(k_F a_s)^{-1} = -1$ (Fig. 2.1(a)), even in the equal population case ($p = 0$), we cross four different phases from the trap center to the edge. The trap center is occupied by a normal mixture state with the heavy fermions (${}^{40}\text{K}$) in excess (denoted as NM_K), which is surrounded by a shell of BCS superfluid phase (denoted as SF). Farther out, there is a shell of a normal mixture

but now with the light fermions (${}^6\text{Li}$) in excess (denoted as NM_{Li}). The trap edge is occupied by the single component normal gas of light fermions (denote as NP_{Li}). The system behavior is significantly more complicated than in the equal-mass case [30, 71–78], where instead of several phases, there is only one superfluid phase over the whole trap in the corresponding configuration. Note that under the LDA, as one moves out from the trap center, the chemical potential monotonically decreases, while the superfluid order parameter is apparently not a monotonic function in the mass-imbalance case. The superfluid only occurs in an intermediate shell. We will give some explanations for this unusual phenomenon later.

Continuing with the phase diagram, if we increase the population of the heavy fermions, the central NM_{K} region grows, while the SF, NM_{Li} , and the NP_{Li} phase regions shrink and finally all disappear at a critical population imbalance. After that, the trap edge is occupied by a single component normal gas of heavy fermions (denoted as NP_{K}). If we increase the population of light fermions, the reverse happens. The central NM_{K} region shrinks and finally disappears at a critical population imbalance, and the superfluid shell evolves into a superfluid core.

On resonance (Fig. 2.1(b) with $(k_F a_s)^{-1} = 0$) the superfluid phase region becomes significantly larger. The normal mixture region NM_{Li} at the intermediate shell completely disappears, in contrast to the equal mass case where there is always such a mixed shell [71, 72]. Moving on to the BEC side of resonance with $(k_F a_s)^{-1} = 0.2$ (Fig. 2.1(c)), the type-I breached pair phase (BP1) appears at an intermediate shell between the SF and NP_{Li} phases, but only when the light fermions are in excess. Compared with the equal mass case [71, 72], the critical $k_F a_s$ for the appearance of the BP1 state is significantly shifted towards the resonance point. Another notable feature at this value of $(k_F a_s)^{-1}$ is that when the heavy fermions are in excess, the

superfluid shell is not surrounded by a normal gas anymore. All the normal components are pushed to the central core. Further into the BEC side with $(k_F a_s)^{-1} = 0.5$ (Fig. 2.1(d)), the normal mixture at the trap center finally disappears for any population imbalance, and we regain the picture of a superfluid core surrounded by a shell of normal gas. The BP1 phase region at the intermediate shell grows as one expects, but again it only appears when the light fermions are in excess.

A remarkable feature from the above phase diagrams is that the superfluid forms a shell structure in space, which separates different types of normal states at the trap center and at the edge. This feature is qualitatively different from the equal mass case. Now we would like to understand in more detail how this feature arises. We know that the phase is determined by the global minimum of the thermodynamic potential Ω as a function of the gap Δ , under certain values of the chemical potentials $\mu_{\mathbf{r}}$ and h at the trap position \mathbf{r} . As one moves out from the trap center, $\mu_{\mathbf{r}}$ monotonically decreases as $\mu_{\mathbf{r}} = \mu - \tilde{\mathbf{r}}^2$ (in units of E_F) while h remains the same. In Fig. 2.2(a), we show Ω as a function of Δ at several different values of the normalized radius \tilde{r} (thus with differing $\mu_{\mathbf{r}}$). The values of h and $\mu(\tilde{r} = 0)$ are taken to be typical ones for which there is a superfluid shell structure in the phase diagram. The potential Ω typically has a double-well structure. At the trap center (the lowest curve with $\tilde{r} = 0$), the trivial well with $\Delta = 0$ is deeper, corresponding to a normal state. As one moves out, both wells are lifted, but with different speeds. At a lower critical value of \tilde{r} (which is 0.38 for the configuration in Fig. 2.2(a)), the two wells become equally deep. Above this value, the global minimum jumps to the nontrivial well with $\Delta \neq 0$, signaling a first-order phase transition to the superfluid state. As one moves farther out, the nontrivial well approaches the trivial well, and at an upper critical value of \tilde{r} (0.81 in Fig. 2.2(a)) the two wells merge, indicating

a second-order phase transition from the superfluid to the normal state. Hence the potential Ω varies non-monotonically with $\mu_{\mathbf{r}}$, leading to the superfluid shell state only at the intermediate region.

The above picture is established from the calculation of Ω . We can also give an intuitive explanation for the superfluid shell state. Note that except in the deep BEC side with a very strong coupling, it is always more favorable for the fermions to pair up when the mismatch of the Fermi surfaces of the two components decreases. As one changes the chemical potential $\mu_{\mathbf{r}}$ by moving out from the trap center, for non-interacting fermions the radius of the Fermi surface in the momentum space $k_F^\sigma(\tilde{r})$ decreases as $k_F^\sigma(\tilde{r}) = \sqrt{2m_\sigma(\mu_\sigma - \tilde{r}^2)}$ (in the standard unit) for the component σ . So $k_F^\sigma(\tilde{r})$ for the heavy fermions decreases faster with increasing \tilde{r} . This qualitative statement should be true also for interacting fermions as interaction will not change the rough trend. Thus we can imagine two situations as depicted in Figs. 2.2(b) and (c). If at the trap center, the Fermi surface of the heavy fermions (^{40}K) has a smaller radius $k_F^\sigma(\tilde{r} = 0)$ (Fig. 2.2(b)), the mismatch of the two Fermi surfaces monotonically grows as one increases \tilde{r} . Therefore the pairing superfluid, if any, can only form a core at the center. On the other hand, if the Fermi surface of the heavy fermions has a larger radius $k_F^\sigma(\tilde{r} = 0)$ (which is the case when ^{40}K are in excess), the mismatch of the Fermi surfaces is minimized at an intermediate region (see Fig. 2.2(c)), so the superfluid only forms near that region and thus takes the shape of a spherical shell. This explains an important qualitative feature of the phase diagram in Fig. 2.1. From this qualitative picture, we expect even when the LDA ceases to be a good approximation, the topology of the superfluid shell may persist, albeit with a shape possibly distorted by the surface tension. As one moves further to the BEC side, the Fermi surface mismatch (and thus the above mechanism) becomes

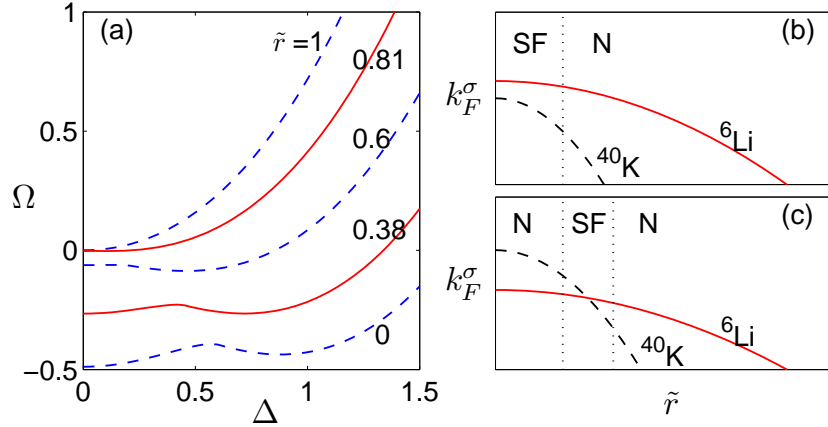


Figure 2.2: (a) The thermodynamical potential Ω shown as a function of the order parameter Δ (both in the unit of E_F) at different trap positions (different chemical potentials) characterized by the normalized radius \tilde{r} . The other parameters are $p = 0.2$, $T = 0$, and $(k_F a_s)^{-1} = 0$. The two solid curves bound a region corresponding to the SF phase, where the global minimum of Ω is at a nonzero Δ . (b) and (c) Schematic illustration of the radius of the Fermi surfaces k_F^σ for the two components as a function of the normalized trap radius \tilde{r} . In (b), one can only have a superfluid core at the trap center, while in (c), one in general has a superfluid shell in the intermediate region.

less important, and finally it becomes irrelevant which component is in excess. The superfluid then always forms a core at the trap center where there is a larger atomic density (Fig. 2.1(d)).

To detect the phase diagram of Fig. 2.1 in general and the superfluid shell state in particular, one can measure the atomic density profiles in the trap. The real-space density profiles for the polarized Fermi gas have been measured in several experiments [27–29, 32]; particularly, in [32] they show how to reconstruct the full density profile from the column integrated signal. We calculate the density profiles for several characteristic configurations of phase separation (Fig. 2.3). Fig. 2.3(a) is for the resonance case with a small population imbalance $p = 0.2$ and at zero temperature. The superfluid shell (where the densities for the two components are equal) is clearly visible, separating two normal regions. From the inside normal state to the superfluid, the heavy (light) fermion densities jump down (up). This jump is consistent with the first-order phase transition picture established from the

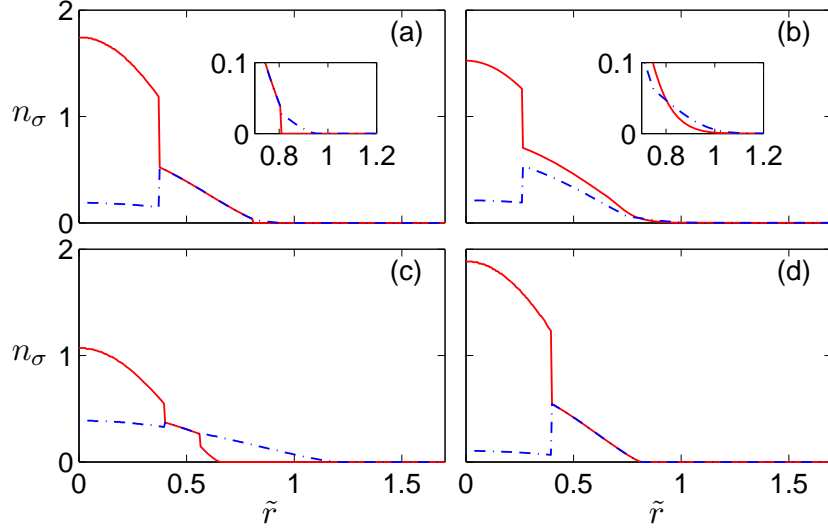


Figure 2.3: The atomic number densities n_σ (in the unit of $n_F \equiv k_F^3/(3\pi^2)$) shown versus the normalized trap radius \tilde{r} . The solid (dashed) curves are for the ^{40}K (^6Li) atoms, respectively. The inserts of (a) and (b) show the amplified tails of the density profiles. The other parameters are: (a) $T = 0$, resonance, and $p = 0.2$, (b) $T = 0.1T_F$, resonance, and $p = 0.2$, (c) $T = 0$, $(k_F a_s)^{-1} = -1$ (BCS side), $p = -0.4$, (d) $T = 0$, $(k_F a_s)^{-1} = 0.2$ (BEC side), $p = 0.3$.

thermodynamic potential Ω shown in Fig. 2.2(a). From the superfluid shell to the outside normal regions, the atomic densities drop continuously (consistent with the second-order phase transition picture in Fig. 2.2(a)). There is a small region in the NM_{Li} state, and outside is a tail for the NP_{Li} region. In Fig. 2.3(b), we show the finite temperature density profiles ($T = 0.1T_F$) with otherwise the same parameters as in Fig. 2.3(a). The profiles become slightly more smooth (as one expects), but the jump from the inside normal to the superfluid shell is still clearly visible. Note that as pointed out in [71, 72], the densities are no longer equal for the BCS superfluid state at finite T since quasiparticle excitations carry population imbalance. Fig. 2.3(c) shows the density profiles on the BCS side. There are jumps in the density profiles from the superfluid shell to both the inside and outside regions of normal states. Fig. 2.3(d) shows the profiles on the BEC side, still with a superfluid shell, but no normal region outside the shell (no tails with unequal densities). On the BEC side, there is also a region of the BP1 state when the light atoms are in excess. The BP1 state

is difficult to detect from the real-space density profile, but can be unambiguously observed using the momentum-space profile of the minority component [102].

2.4 Chapter Summary

In this chapter, we have discussed the BEC-BCS crossover in an ultracold Fermi gas across a Feshbach resonance with unequal populations and masses. The gas shows various phases such as superfluids, normal fully polarized phases, normal mixtures, and breached-pair phases. Different phases separate by forming shell structures within a trap. The formation of superfluid cores or shells can be intuitively understood by considering the intersection of Fermi surfaces. We calculate the in-trap density profiles, which should be experimentally detectable quantities. We also anticipate that the formation of a superfluid shell will lead to interesting vortex behaviors. Our prediction of superfluid shells is also supported by other work [89–91].

CHAPTER III

BCS-BEC Crossover in a Quasi-two-dimensional Fermi Gas

3.1 Overview

Interest in low-dimensional Fermi systems has recently revived due to experimental developments of cooling and trapping atoms in optical lattices [9–12, 44, 103, 104] and on atom chips [105]. With the aid of magnetic Feshbach resonances, these techniques provide a fascinating opportunity of creating quasi-low-dimensional Fermi systems with controllable atomic interaction. This opens a possibility for BEC-BCS crossover behavior to be investigated in lower dimensions. This line of research has potential applications closely connected to high- T_c superconductivity [106, 107] and the quantum Hall effect [19, 20].

In three-dimensional (3D) Fermi systems, a single-channel model [97–99] and a two-channel model [94, 95] are employed to describe degenerate behaviors, and both give a consistent description around a wide Feshbach resonance (see Chapter II). This agreement between single- and two-channel models is rooted in the fact that the closed-channel (Feshbach molecule) population is negligible near a wide resonance, so that it makes no significant difference to explicitly include (as in the two-channel model) or neglect (as in the single-channel model) the molecular degree of freedom. In this chapter, we first start with a single-channel point of view, using an effective two-

dimensional (2D) Hamiltonian with renormalized atom-atom interaction (model 1) [39, 108, 109]. Next, a more general model is proposed with renormalized interaction between atoms and dressed molecules (model 2) [110]. The dressed molecules mainly come from population of atoms in the excited levels along the strongly confined axial direction near a Feshbach resonance [110, 111].

In this work, we consider a quasi-2D gas contained in a weak radial trap, i.e., an inhomogeneous (harmonic) layer under the mean-field (MF) approximation and the local density approximation (LDA). The above two models are employed to calculate the in-trap density profiles and the cloud size at zero temperature. We compare the results of the two models and find significant differences. For model 2, we show that the cloud size continuously decreases from the BCS side to the BEC side as one tunes across the Feshbach resonance. This picture is in agreement with the intuition that fermions form composite bosons on the BEC side: the bosonic wavefunctions allow spatial overlapping, so that the cloud should shrink in size. On the contrary, model 1 fails to describe this crossover behavior by predicting a constant cloud size and identical density profile for all magnetic field detunings. This discrepancy implies that the MF results given by model 1 are unreliable, even at a qualitative level. Given this qualitative discrepancy and the problem associated with model 1 for description of the two-body ground state of the system [112], it is likely that the oversimplification is rooted in the model itself instead of the MF approximation.

The quasi-2D geometry can be realized by strongly confining the fermions along the axial (z) direction in an optical lattice. They form a series of quasi-2D pancake-shaped clouds when a weak harmonic trapping potential is applied on the radial (x - y) plane [12, 104]. Each such pancake-shaped cloud can be considered as a quasi-2D Fermi gas when the axial confinement is strong enough to turn off inter-cloud

tunneling. The strong anisotropy of trapping potentials introduces two different orders of energy scales, with one characterized by $\hbar\omega_z$ and the other by $\hbar\omega_\perp$, where ω_z (ω_\perp) are the trapping frequencies in the axial (radial) directions. The separation of these two energy scales ($\omega_z \gg \omega_\perp$) allows us to first deal with the axial degrees of freedom and derive an effective 2D Hamiltonian, leaving the radial degrees of freedom for later treatment.

The structure of this chapter is outlined as follows. In Sec. 3.2 and Sec. 3.3 we present a single-channel model and a more general two-channel model, respectively, as well as the calculation results, which are compared and discussed at the end of Sec. 3.3.

3.2 Model 1 with Renormalized Atom-atom Interaction

The effective 2D Hamiltonian for model 1 is obtained by assuming that the renormalized atom-atom interaction can be characterized with an effective 2D scattering length, with the latter derived from the exact two-body scattering physics [39, 108, 109]. Thus, for a wide Feshbach resonance where the Feshbach-molecule population is negligible, we can write down an effective Hamiltonian only in terms of 2D fermionic operators $a_{\mathbf{k},\sigma}$ and $a_{\mathbf{k},\sigma}^\dagger$, with (pseudo) spin σ and transverse momentum $\mathbf{k} = (k_x, k_y)$. The model 1 Hamiltonian takes the form [39, 106–109]

$$\begin{aligned}
 H_1 &= \sum_{\mathbf{k},\sigma} (\epsilon_{\mathbf{k}} - \mu) a_{\mathbf{k},\sigma}^\dagger a_{\mathbf{k},\sigma} \\
 &+ \frac{V_1^{\text{eff}}}{L^2} \sum_{\mathbf{k},\mathbf{k}',\mathbf{q}} a_{\mathbf{k},\uparrow}^\dagger a_{-\mathbf{k}+\mathbf{q},\downarrow}^\dagger a_{\mathbf{k}',\downarrow} a_{-\mathbf{k}'+\mathbf{q},\uparrow},
 \end{aligned} \tag{3.1}$$

where $\epsilon_{\mathbf{k}} = \hbar^2 k^2 / (2m)$ is the 2D dispersion relation of fermions with mass m , μ is the chemical potential, and L^2 is the quantization area. The bare parameter V_1^{eff} is connected with the physical one V_{1p}^{eff} through the 2D renormalization relation

$[V_1^{\text{eff}}]^{-1} = [V_{1p}^{\text{eff}}]^{-1} - L^{-2} \sum_{\mathbf{k}} (2\epsilon_{\mathbf{k}} + \hbar\omega_z)^{-1}$ ($\hbar\omega_z$ is from the zero-point energy), and $V_{1p}^{\text{eff}} = V_{1p}^{\text{eff}}(a_s, a_z)$ depends on the 3D scattering length a_s and the characteristic length scale for axial motion $a_z \equiv \sqrt{\hbar/(m\omega_z)}$ according to the expression given in [39, 108–110]. Notice that the chemical potential μ can be a function of the radial coordinate $\mathbf{r} = (x, y)$ under LDA. In the following discussion, we choose $\hbar\omega_z$ as the energy unit so that μ , V_1^{eff} , and $\epsilon_{\mathbf{k}} = a_z^2 k^2/2$ become dimensionless.

By introducing a dimensionless BCS order parameter (normalized by $\hbar\omega_z$) $\Delta \equiv (V_1^{\text{eff}}/L^2) \sum_{\mathbf{k}} \langle a_{\mathbf{k},\downarrow} a_{-\mathbf{k},\uparrow} \rangle$, we get the zero temperature thermodynamic potential density

$$\Omega = -\frac{\Delta^2}{V_1^{\text{eff}}} + \frac{1}{L^2} \sum_{\mathbf{k}} (\epsilon_{\mathbf{k}} - \mu - E_{\mathbf{k}}), \quad (3.2)$$

where $E_{\mathbf{k}} = \sqrt{(\epsilon_{\mathbf{k}} - \mu)^2 + \Delta^2}$ is the quasi-particle excitation spectrum. The ultra-violet divergence of the summation over \mathbf{k} cancels with the renormalization term in $[V_1^{\text{eff}}]^{-1}$. The gap and number equations can be obtained respectively from $\partial\Omega/\partial\Delta^2 = 0$ and $n = -\partial\Omega/\partial\mu$ ($n = N/L^2$ is the density of particles), leading to

$$\frac{1}{V_{1p}^{\text{eff}}(a_s, a_z)} = \frac{\ln(-\mu + \sqrt{\mu^2 + \Delta^2})}{4\pi a_z^2}, \quad (3.3)$$

$$n = \frac{\mu + \sqrt{\mu^2 + \Delta^2}}{2\pi a_z^2}. \quad (3.4)$$

Notice that Eq. (3.3) can be rewritten as $F(a_s, a_z) = -\mu + \sqrt{\mu^2 + \Delta^2}$, where the function F absorbs all the dependence on a_s and a_z . Thus, by substituting this expression into Eq. (3.4), we get a closed form for the number equation,

$$n = \frac{1}{\pi a_z^2} \left[\frac{F(a_s, a_z)}{2} + \mu \right]. \quad (3.5)$$

Now we take into account the harmonic trapping potential $U(\mathbf{r}) = (\omega_{\perp}/\omega_z)^2 r^2/(2a_z^2)$ in the radial plane by writing down the position-dependent chemical potential $\mu(\mathbf{r}) =$

$\mu_0 - U(\mathbf{r})$, where μ_0 is the chemical potential at the trap center. It can be easily shown that the spatial density profile is now a parabola, $n(\mathbf{r}) = (\omega_\perp/\omega_z)^2(R_{\text{TF}}^2 - r^2)/(2\pi a_z^4)$, with the Thomas-Fermi cloud size $R_{\text{TF}} = \sqrt{2\mu_0}a_z(\omega_z/\omega_\perp)$. Assigning the condition that the total number of particles in the trap is fixed at $N = \int n(\mathbf{r})d^2\mathbf{r}$, the cloud size takes the constant value $R_{\text{TF}} = R_{\text{BCS}} \equiv \sqrt{2\omega_z/\omega_\perp}N^{1/4}a_z$, which is independent of the 3D scattering length a_s . In fact, as one varies the scattering length a_s , the chemical potential at the trap center μ_0 is adjusted accordingly such that an identical density profile is maintained.

This result of a constant cloud size is obviously inconsistent with the picture of a BCS-BEC crossover in quasi-two dimensions. In fact, in a typical experiment with a_z ($\sim \mu\text{m}$) much greater than the atom-atom interaction potential R_e ($\sim \text{nm}$), the scattering of atoms in this quasi-2D geometry is still 3D in nature. In particular, fermions will form tightly bound pairs on the BEC side of the Feshbach resonance as they do in 3D. Thus, in the BEC limit when fermion pair size $a_{\text{pair}} \ll a_z$ and binding energy $|E_b| \gg \hbar\omega_z$, the system essentially behaves like a weakly interacting gas of point-like bosons, for which one would expect a vanishingly small cloud size in the loosely confined radial plane [108, 113].

The MF result of a finite cloud size in the BEC limit from model 1 indicates a finite interaction strength between paired fermions, no matter how small they are in size. This conclusion can be extracted directly from the number equation (3.5), which can be written in the form $\mu = n\pi a_z^2 - F(a_s, a_z)/2$. In the BEC limit, the second term on the right-hand side represents one half of the binding energy, while the first term indicates a finite interaction energy per fermion pair since it is proportional to the number density. As a comparison, the actual equation of state one should expect for fermion pairs must take the form as for a quasi-2D Bose gas in the weakly interacting

limit [108]

$$\mu_B \approx 3na_z a_s, \quad (3.6)$$

in which case the quasi-2D gas is treated as a 3D condensate with the ground state harmonic oscillator wave function in the z -direction.

The interaction strength between paired fermions can also be derived by writing a Bose representation for this system, where the fermionic degrees of freedom are integrated out in the BEC limit [114]. This Bose representation leads to a 2D effective Hamiltonian for bosonic field $\phi(\mathbf{r})$,

$$H_{\text{eff}} = \int d\mathbf{r} \left[\phi^\dagger(\mathbf{r}) \left(-\frac{\hbar^2 \nabla^2}{4m} + 2U(\mathbf{r}) \right) \phi(\mathbf{r}) - \frac{g_2}{2} |\phi(\mathbf{r})|^4 \right], \quad (3.7)$$

where the quartic term characterizes the bosonic interaction. Within the stationary phase approximation, the interaction strength g_2 is calculated by the leading diagram of a four-fermion process with four external boson lines and four internal fermion propagators, leading to [114]

$$g_2 = 2 \sum_{\mathbf{p}, \omega} \Lambda_0^4(\mathbf{p}) G_0^2(\mathbf{p}, \omega) G_0^2(-\mathbf{p}, -\omega). \quad (3.8)$$

Here $\Lambda_0 = (-p^2/m + |E_b|)\chi_0(\mathbf{p})$ is the boson-fermion vertex, $\chi_0(\mathbf{p})$ is the Fourier transform of the relative wave function $\chi_0(\mathbf{r})$ of two colliding fermions in the s -wave channel, and $G_0(\mathbf{p}, \omega) = (i\omega - p^2/2m - |E_b|/2)^{-1}$ is the free propagator for fermions. After summing over momentum \mathbf{p} and Matsubara frequency ω , we can directly show that g_2 indeed takes a constant value, being independent of the binding energy $|E_b|$ of paired fermions and hence the 3D scattering parameter a_s . Thus, we conclude that the MF theory based on model 1 fails to recover the picture of a weakly interacting Bose gas of paired fermions in the BEC limit, and cannot be directly applied to describe the BCS-BEC crossover in quasi-two dimensions.

3.3 Model 2 with Inclusion of Dressed Molecules

Having shown the problem associated with model 1, we next consider model 2 by taking into account the axially excited states via inclusion of dressed molecules. As derived in [110], the effective 2D Hamiltonian takes the form (also in units of $\hbar\omega_z$),

$$\begin{aligned}
H_2 &= \sum_{\mathbf{k},\sigma} (\epsilon_{\mathbf{k}} - \mu) a_{\mathbf{k},\sigma}^\dagger a_{\mathbf{k},\sigma} + \sum_{\mathbf{q}} \left(\frac{\epsilon_{\mathbf{q}}}{2} + \lambda_b - 2\mu \right) d_{\mathbf{q}}^\dagger d_{\mathbf{q}} \\
&+ \frac{\alpha_b}{L} \sum_{\mathbf{k},\mathbf{q}} \left(a_{\mathbf{k},\uparrow}^\dagger a_{-\mathbf{k}+\mathbf{q},\downarrow}^\dagger d_{\mathbf{q}} + \text{h.c.} \right) \\
&+ \frac{V_b}{L^2} \sum_{\mathbf{k},\mathbf{k}',\mathbf{q}} a_{\mathbf{k},\uparrow}^\dagger a_{-\mathbf{k}+\mathbf{q},\downarrow}^\dagger a_{-\mathbf{k}',\downarrow} a_{\mathbf{k}'+\mathbf{q},\uparrow},
\end{aligned} \tag{3.9}$$

where $d_{\mathbf{q}}^\dagger$ ($d_{\mathbf{q}}$) denotes the creation (annihilation) operator for dressed molecules with radial momentum \mathbf{q} , and λ_b , α_b , and V_b are the 2D effective bare detuning, atom-molecule coupling rate, and background interaction, respectively. These parameters can be related to the corresponding 3D parameters by matching the two-body physics [110]. By introducing the order parameter $\Delta \equiv \alpha_b \langle d_0 \rangle / L + (V_b/L^2) \sum_{\mathbf{k}} \langle a_{\mathbf{k},\downarrow} a_{-\mathbf{k},\uparrow} \rangle$, we obtain the MF gap and number equations,

$$\frac{1}{V_{2p}^{\text{eff}}(2\mu)} = \frac{\ln \left(-\mu + \sqrt{\mu^2 + \Delta^2} \right)}{4\pi a_z^2}, \tag{3.10}$$

$$n = \frac{\mu + \sqrt{\mu^2 + \Delta^2}}{2\pi a_z^2} + 2\Delta^2 \frac{\partial [V_{2,p}^{\text{eff}}(x)]^{-1}}{\partial x} \Bigg|_{x=2\mu}, \tag{3.11}$$

where the inverse of effective interaction is connected with the 3D physical parameters through [110]

$$\begin{aligned}
[V_{2p}^{\text{eff}}(x)]^{-1} &= \left[V_b + \frac{\alpha_b^2}{x - \lambda_b} \right]^{-1} + \frac{1}{L^2} \sum_{\mathbf{k}} \frac{1}{2\epsilon_{\mathbf{k}} + \hbar\omega_z} \\
&= \frac{\sqrt{2\pi}}{a_z^2} \left[\left(U_p + \frac{g_p^2}{x - \gamma_p} \right)^{-1} - S_p(x) + \sigma_p(x) \right].
\end{aligned} \tag{3.12}$$

Here $U_p = 4\pi a_{bg}/a_z$, $g_p^2 = \mu_{co} W U_p / (\hbar\omega_z)$, and $\gamma_p = \mu_{co}(B - B_0) / (\hbar\omega_z)$ are 3D dimensionless physical parameters, where a_{bg} is the background scattering length, μ_{co}

is the difference in magnetic moments between the two channels, W is the resonance width, and B_0 is the resonance point. The functions in Eq. (3.12) take the form

$$S_p(x) = \frac{-1}{4\sqrt{2\pi}} \int_0^\infty ds \left[\frac{\Gamma(s - x/2)}{\Gamma(s + 1/2 - x/2)} - \frac{1}{\sqrt{s}} \right], \quad (3.13)$$

$$\sigma_p(x) = \frac{\ln|x|}{4\pi\sqrt{2\pi}}, \quad (3.14)$$

where $\Gamma(x)$ is the gamma function.

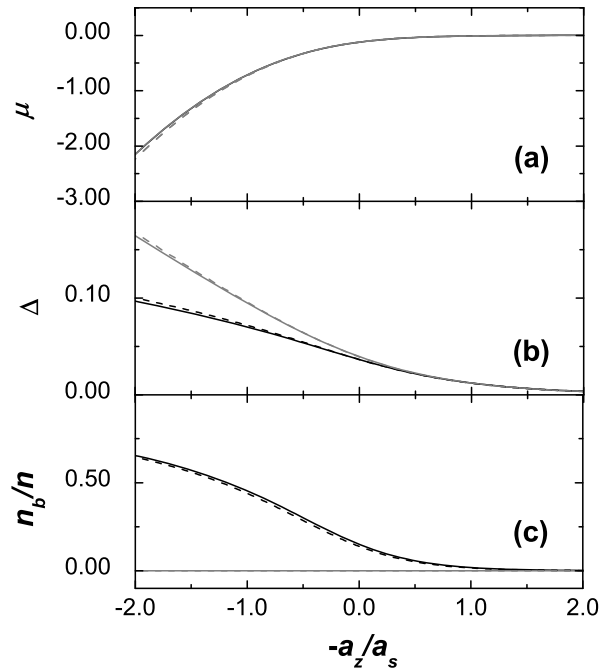


Figure 3.1: The BCS-BEC crossover behavior of a uniform quasi-2D Fermi gas at zero temperature, showing (a) the chemical potential μ , (b) the gap Δ , both in unit of $\hbar\omega_z$, and (c) the dressed-molecule fraction n_b/n . Notice that the results for ${}^6\text{Li}$ (solid) and those for ${}^{40}\text{K}$ (dashed) almost coincide as plotted as functions of a_z/a_s , indicating a universal behavior around the resonance point. Furthermore, significant difference between model 1 (gray) and model 2 (black) can be observed in (b) and (c), which shows that model 1 is oversimplified at unitary and on the BEC side of the resonance. The parameters used in these plots are $\omega_z = 2\pi \times 62$ kHz, and $na_z^2 = 0.001$.

Using this model 2 Hamiltonian, we first consider a uniform quasi-2D Fermi gas with a fixed number density n , where the inhomogeneity in the radial plane is neglected. In this case, the gap and number equations (3.10) and (3.11) need to be solved self-consistently for a given magnetic field. A typical set of results for both ${}^6\text{Li}$

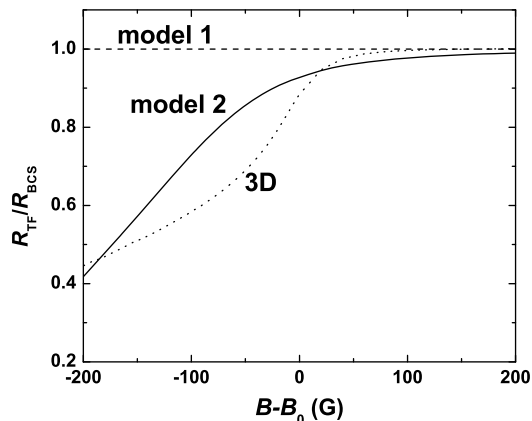


Figure 3.2: The Thomas-Fermi cloud size of a quasi-2D Fermi gas of ${}^6\text{Li}$ over a wide BCS-BEC crossover region. Here, results from model 2 (solid) are compared with those from model 1 (dashed). All curves are normalized to the cloud size of a noninteracting Fermi gas R_{BCS} . Notice that the results of model 2 recover the correct pictures in the BCS and BEC limits, in clear contrast to the model 1 prediction of a flat line. Parameters used for these two plots are $\omega_z = 2\pi \times 62$ kHz, $\omega_\perp = 2\pi \times 20$ Hz, and the total particle number $N = 10^4$. For reference, the results for an isotropic 3D Fermi gas with the same total particle number is also plotted (dotted), where a single-channel model and a two-channel model are both incorporated to give indistinguishable predictions.

and ${}^{40}\text{K}$ are shown in Fig. 3.1, indicating a smooth crossover from the BCS (right) to the BEC (left) regimes. Here results obtained from model 2 (black) are compared with those from model 1 (gray). In this figure and the following calculation, we use the parameters $a_{bg} = -1405a_0$, $W = 300$ G, $\mu_{co} = 2\mu_B$ for ${}^6\text{Li}$, and $a_{bg} = 174a_0$, $W = 7.8$ G, $\mu_{co} = 1.68\mu_B$ for ${}^{40}\text{K}$, where a_0 and μ_B are Bohr radius and Bohr magneton, respectively.

There are two major points that need to be emphasized in Fig. 3.1. First, when plotted as functions of the inverse of 3D scattering length a_z/a_s , the results for ${}^6\text{Li}$ (solid) and ${}^{40}\text{K}$ (dashed) are very close, manifesting the near resonance universal behavior. Second, the results from model 1 and model 2 are significantly different, especially on the BEC side of the resonance. In particular, the dressed-molecule fraction in model 2 is already sizable (~ 0.16) at unitary, and becomes dominant on the BEC side of the resonance (see Fig. 3.1(c)). This result is another indication of

the inadequacy of model 1, where the dressed-molecule population is always assumed to be negligible.

Next, we impose a radial harmonic trap $U(\mathbf{r})$ and calculate the Thomas-Fermi cloud size for a fixed number of particles in the trap $N = \int 2\pi n(r)rdr$, as shown in Fig. 3.2. The most important feature of Fig. 3.2 is that the cloud size given by model 2 (solid) is no longer a constant as predicted by model 1 (dashed). On the contrary, by crossing the Feshbach resonance, the cloud size decreases from the limiting value R_{BCS} of a noninteracting Fermi gas in the BCS limit, and approaches to the 3D results (dotted) in the BEC limit. This trend successfully recovers the corresponding physics in both the BCS and the BEC limits. In addition, we also find that for a given number of particles in the trap, the curve trend is insensitive to the radial trapping frequency ω_{\perp} within the experimentally accessible region. (The $\omega_{\perp} = 2\pi \times 10$ Hz and $2\pi \times 50$ Hz results, not shown, coincide with the $2\pi \times 20$ Hz line and are hardly distinguishable within the figure resolution.) Considering the fact that there is a scaling relation between ω_{\perp} and N such that the physics is only determined by $N(\omega_{\perp}/\omega_z)^2$, this insensitivity to the radial trapping frequency suggests that the experimental measurement has a rather wide range of tolerance on the number of atoms.

In Fig. 3.3 we show the number density and the dressed-molecule fraction distribution along the radial direction for various values of a_z/a_s . A typical case in the BCS regime is shown in the top panel of Fig. 3.3, where the dressed-molecule fraction is vanishingly small, and model 1 and model 2 predict similar cloud sizes and number density distributions. The middle panel shows the case at unitary. As compared with model 1, notice that the cloud is squeezed in model 2, and the dressed-molecule fraction increases to a sizable value. The bottom panel shows a typical case in the

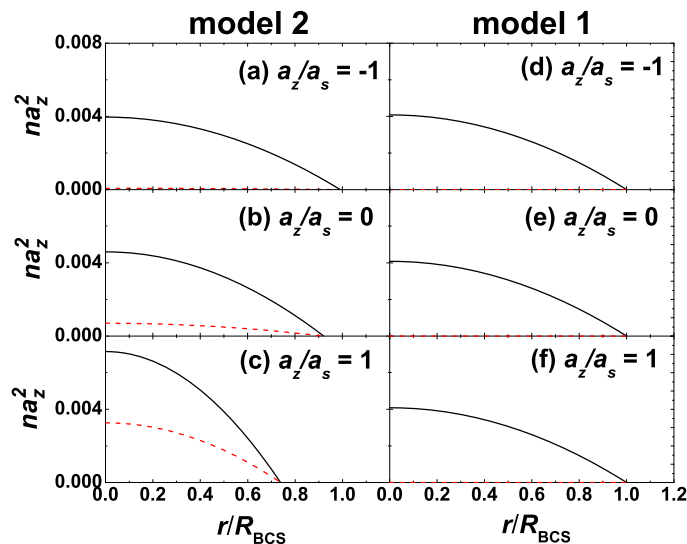


Figure 3.3: The in-trap number density (the solid lines) and dressed-molecule fraction (the dashed lines) distribution along the radial direction of a quasi-2D Fermi gas of ${}^6\text{Li}$, obtained from model 2 (a-c) and model 1 (d-f). The top panels correspond to the case of $a_z/a_s = -1$ (BCS side), the middle panels to the case of $a_z/a_s = 0$ (unitary), and the bottom panels to the case of $a_z/a_s = 1$ (BEC side). The parameters are $\omega_z = 2\pi \times 62$ kHz, $\omega_\perp = 2\pi \times 20$ Hz, and $N = 10^4$.

BEC regime, where the cloud is squeezed further in model 2 as the dressed-molecule fraction becomes significant. Notice that the results of model 2 successfully describe the BCS-BEC crossover, in clear contrast to the outcome of model 1.

3.4 Chapter Summary

In summary, we have considered the BCS-BEC crossover of a quasi-2D Fermi gas across a wide Feshbach resonance. We have analyzed two effective Hamiltonians and compared predictions of zero temperature cloud size and in-trap number density distribution from the MF approach and LDA. Using model 1 with renormalized atom-atom interaction, we show that the cloud size remains a constant value through the entire BCS-BEC crossover, which is inconsistent with the picture of a weakly interacting Bose gas of fermion pairs in the BEC limit. On the other hand, model 2 with renormalized interaction between atoms and dressed molecules predicts the

correct trend of cloud size change. Based on this qualitative comparison, it can be concluded that the inclusion of dressed molecules is essential to describe the BCS-BEC crossover in quasi-low dimensions [110, 111].

CHAPTER IV

Characteristics of Bose-Einstein Condensation in an Optical Lattice

4.1 Overview

During recent years there has been significant interest in ultracold atomic gases in optical lattices, partly stimulated by the possibility of simulating strongly correlated many-body systems [8, 115]. With extraordinary controllability, ultracold atomic gases in lattices provide a promising experimental platform to help tackle important problems across multiple disciplines. A problem which has drawn great attention over the past decade is the emergence of condensation and superfluid order in an optical lattice, as well as how the superfluid order transfer into other ordered states. With current technology, condensation and superfluidity are obtained for both Bose and Fermi gases in optical lattices, so that various phase transitions can be investigated [42, 44].

To experimentally investigate these phase transitions, present techniques with ultracold atomic gases rely heavily on detection based on the time-of-flight imaging, where the interference pattern and its visibility appear to be signatures of Bose condensation within an optical lattice [42]. Recent studies show that even for a thermal lattice gas above the BEC transition temperature T_c , interference peaks with observable visibility are still present [47–49]. This thermal visibility can be large for

an ideal Bose gas in a homogeneous lattice, which could make the condensation signal ambiguous [47]. However, for practical systems with atomic interaction and an inhomogeneous global trap, the thermal visibility becomes significantly smaller [48, 49], and the appearance of sharp interference peaks is still associated with the BEC transition. It is also suggested [49] that the bimodal structure of the atomic momentum distribution in the first Brillouin zone, combined with the interference peaks, provides an additional unambiguous signal for Bose condensation in an optical lattice. A very recent experiment used the onset of the bimodal distribution and the associated condensate fraction to identify the superfluid-to-Mott-insulator transition point [40].

In this chapter, we provide a detailed study of a Bose gas in a three-dimensional (3D) inhomogeneous optical lattice, both below and above the BEC transition temperature. We discuss several properties including the visibility, the width of the interference peak, and the momentum distribution of the resulting interference pattern. The main results are as follows. First, all the quantities mentioned above can characterize the BEC transition for experimental systems with interacting atoms in an inhomogeneous optical lattice. The large thermal visibility applies only to some particular parameters which are not directly responsible for current experiments. In the case when the thermal visibility is large, a substantial variation of the peak width or the appearance of a bimodal structure for the atomic momentum distribution may work as a better signature for the condensation transition. Second, below the BEC transition temperature, the visibility and the peak width become insensitive to the system temperature, and hence cannot be applied as a practical thermometer. To fill this gap, the bimodal structure of the atomic momentum distribution gives a way to extract the condensate fraction through the bimodal fitting. The resulting

condensate fraction provides a sensitive indicator of the system temperature, and hence may serve as a potential thermometer for this important system.

The structure of this chapter is organized as follows. In Sec. 4.2, we first consider the situation of free bosons in an optical lattice within a global harmonic trap, and investigate the general behavior of the interference visibility and the atomic momentum distribution. In the absence of interaction, the problem is significantly simplified such that exact solutions are available. These exact solutions are valuable first for qualitative understanding of the system and its properties, and secondly for direct comparison with experiments when the Feshbach resonance technique is applied to turn off the atomic interaction. After studying the free Bose gas, we extend our discussion in Sec. 4.3 to the case of interacting bosons, where effects of the global harmonic trap and the interaction have to be taken into account together. In order to deal with the trap, we adopt the local density approximation (LDA), which works well when the interaction energy scale is significantly larger than the trapping energy scale (this condition is typically valid for current experiments). Restricting our discussion to weakly interacting bosons away from the Mott region, we apply the Hartree-Fock-Bogoliubov-Popov (HFBP) approximation to deal with the atomic interaction [45, 116, 117]. The HFBP method can provide a reliable description except in a narrow region around the BEC transition temperature [116, 118]. Taking into account the effect of the global trap, this questionable region only corresponds to a thin shell in three dimensions, and its influence on the global properties is small. Therefore, we expect that the HFBP method can give reliable results for the atomic momentum distribution and the condensate fraction.

4.2 Ideal Bose Gas in an Inhomogeneous Optical Lattice

4.2.1 Formalism

In this section, we discuss an ideal Bose gas in an inhomogeneous optical lattice with a global harmonic trap. For completeness, we briefly review the formalism [49] before presenting detailed results. We consider atoms in a cubic lattice with an additional spherically symmetric harmonic trap [119]. The Hamiltonian takes the form

$$H = \int d^3\mathbf{r} \Psi^\dagger(\mathbf{r}) \left[-\frac{\hbar^2 \nabla_{\mathbf{r}}^2}{2m} + V_{\text{op}}(\mathbf{r}) + V(\mathbf{r}) \right] \Psi(\mathbf{r}), \quad (4.1)$$

where Ψ represents the bosonic field operator, m is the atomic mass, $V_{\text{op}}(\mathbf{r}) \equiv V_0 \sum_{i=x,y,z} \sin^2(\pi r_i/d)$ is the optical lattice potential with lattice spacing d , and $V(\mathbf{r}) \equiv m\omega^2 r^2/2$ is the global harmonic trapping potential. In practice, the global harmonic trap $V(\mathbf{r})$ typically varies much more slowly than the optical lattice potential $V_{\text{op}}(\mathbf{r})$, so the Hamiltonian can be separated into two parts with fast and slow variations, respectively. The fast-varying part can be diagonalized by introducing the expansion of bosonic field operators

$$\Psi(\mathbf{r}) = \sum_{\mathbf{R}} w(\mathbf{r} - \mathbf{R}) a_{\mathbf{R}}, \quad (4.2)$$

where $w(\mathbf{r})$ is the Wannier function associated with the lattice potential $V_{\text{op}}(\mathbf{r})$, $a_{\mathbf{R}}$ is the annihilation operator on site \mathbf{R} , and the summation is over all lattice sites. After transforming to momentum space, the Fourier components of $\Psi(\mathbf{r})$, $w(\mathbf{r})$, and $a_{\mathbf{R}}$ satisfy the following relation

$$\Psi(\mathbf{k}) = w(\mathbf{k}) a_{\mathbf{k}}. \quad (4.3)$$

Representing the fast- and slow-varying components of H in terms of $a_{\mathbf{k}}$ and $a_{\mathbf{R}}$, respectively, the original Hamiltonian Eq. (4.1) can be written as

$$H = \sum_{\mathbf{k} \in 1\text{BZ}} \epsilon_{\mathbf{k}} a_{\mathbf{k}}^{\dagger} a_{\mathbf{k}} + \sum_{\mathbf{R}} V(\mathbf{R}) a_{\mathbf{R}}^{\dagger} a_{\mathbf{R}}, \quad (4.4)$$

where the summation over quasi-momentum \mathbf{k} is restricted to the first Brillouin zone (1BZ). Here we assume that the lattice depth V_0 is strong enough that the band gap is large and atoms are confined to the lowest band with dispersion relation $\epsilon_{\mathbf{k}} = -2t \sum_{i=x,y,z} \cos(k_i d)$. The tunneling rate t can be well estimated by $t \approx (3.5/\sqrt{\pi}) V_0^{3/4} \exp(-2\sqrt{V_0})$, where the recoil energy $E_{\text{R}} \equiv \hbar^2 \pi^2 / (2md^2)$ is used as the energy unit [111].

In principle, the resulting Hamiltonian Eq. (4.4) can be directly diagonalized for arbitrary $V(\mathbf{R})$. However, the numerical calculation is usually very heavy in three dimensions due to the presence of a large number of lattice sites. In this case, the diagonalization process can be significantly simplified by noticing that the indices \mathbf{k} and \mathbf{R} in Eq. (4.4) are reminiscent of the coordinate and the momentum variables in quantum mechanics. This observation allows us to write down a first quantization Hamiltonian corresponding to Eq. (4.4) in momentum space, where \mathbf{R} is replaced by the momentum gradient $-i\nabla_{\mathbf{k}}$ [49, 120–122]. The resulting effective Hamiltonian thus takes the form

$$H_{\text{eff}} = -\frac{1}{2} m \omega^2 \nabla_{\mathbf{k}}^2 + \epsilon_{\mathbf{k}}, \quad (4.5)$$

which represents free bosons with effective mass $m^* \equiv \hbar^2 / (m\omega^2)$ in a periodic potential $\epsilon_{\mathbf{k}}$ with period $|\mathbf{G}| = 2\pi/d$ along all three principal directions. Furthermore, since $\nabla_{\mathbf{k}}^2$ and $\epsilon_{\mathbf{k}}$ are separable, this Hamiltonian can be reduced to three one-dimensional problems which require much less effort to solve. Notice that the properties of this effective Hamiltonian depend only on the ratio $\hbar^2 \omega^2 / (tE_{\text{R}})$, which suggests that the

variation of ω and V_0 can be scaled to each other by fixing the dimensionless parameter $\hbar^2\omega^2/(V_0^{3/4}e^{-2\sqrt{V_0}})$, where E_R is used as the energy unit. In this section, we will keep V_0 fixed ($V_0 = 10E_R$) and look at changes in the system properties under variation of the global trapping frequency ω . With different lattice barriers V_0 , one can directly read out the result by simply re-scaling ω to keep $\hbar^2\omega^2/(V_0^{3/4}e^{-2\sqrt{V_0}})$ fixed (a smaller barrier thus corresponds to a larger effective trapping frequency).

The quasi-momentum distribution $\langle a_{\mathbf{k}}^\dagger a_{\mathbf{k}} \rangle$ is then given by the square of the eigenstate wave functions $\phi_{\mathbf{n}}(\mathbf{k})$ of H_{eff} , where the expectation value is obtained by averaging over all eigenstates \mathbf{n} with a Bose distribution factor $g(E_{\mathbf{n}}) = 1/\exp[\beta(E_{\mathbf{n}} - \mu) - 1]$. Here, $E_{\mathbf{n}}$ is the corresponding eigenenergy, μ is the chemical potential, and $\beta = 1/(k_B T)$ is the inverse temperature. Taking into account the presence of the Wannier function in Eq. (4.3), the atomic *real* momentum distribution is

$$\begin{aligned} n(\mathbf{k}) &= \langle \Psi^\dagger(\mathbf{k})\Psi(\mathbf{k}) \rangle = |w(\mathbf{k})|^2 \langle a_{\mathbf{k}}^\dagger a_{\mathbf{k}} \rangle \\ &= |w(\mathbf{k})|^2 \sum_{\mathbf{n}} g(E_{\mathbf{n}}) |\phi_{\mathbf{n}}(\mathbf{k})|^2. \end{aligned} \quad (4.6)$$

For a free gas, this momentum distribution remains unchanged during expansion, so that the signal from the time-of-flight image taken along a crystallographic axis, say z direction, is just the columnar density

$$n_{\perp}(k_x, k_y) = \int n(\mathbf{k}) dk_z. \quad (4.7)$$

4.2.2 Interference patterns

Using the technique sketched above, we show in Fig. 4.1 the calculation results for the column-integrated momentum distribution as recorded by the time-of-flight images, both below and above the BEC transition temperature T_c . In these plots, we choose parameters close to those for a typical experiment of ^{87}Rb atoms, where the

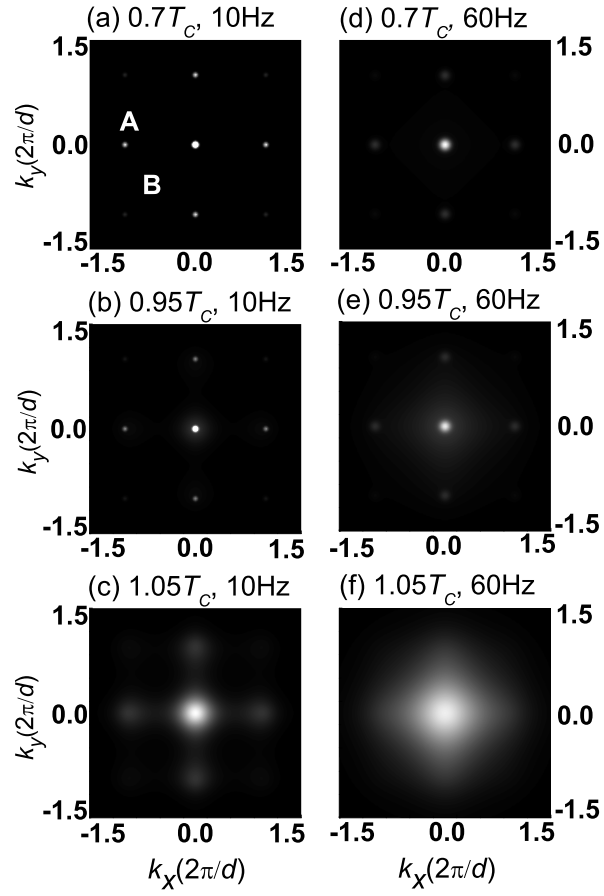


Figure 4.1: Calculated column-integrated momentum density profile near the first Brillouin zone measured through the time-of-flight imaging, taking for two different trapping frequencies at various temperatures. Parameters chosen in these plots are close to those for a typical experiment of ^{87}Rb , with lattice depth $V_0 = 10E_R$ and a total number of particles $N = 10^5$. The global harmonic trapping frequencies are $\omega = 2\pi \times 10$ Hz for (a)-(c), and $2\pi \times 60$ Hz for (d)-(f).

lattice depth $V_0 = 10E_R$, and the total number of particles $N = 10^5$. For this finite system, the transition temperature T_c is determined by requiring that the number of atoms in the ground state is of the order of 1 when $T > T_c$ and increases by orders of magnitude when T crosses T_c . Since the total atom number satisfies $N \gg 1$, the transition is actually very sharp, and T_c is well defined by the requirement above.

From Fig. 4.1, it is apparent that for the case of a very weak global trap ($\omega = 2\pi \times 10$ Hz), the interference peaks are clearly visible even above the transition temperature. However, the BEC transition is still evident from the time-of-flight images, as the interference peaks become much sharper when T falls below T_c . For the case with a stronger global trap ($\omega = 2\pi \times 60$ Hz, which is close to the value in experiments), the interference peaks become blurred when $T > T_c$ (although one can still read some pattern). Once the temperature is tuned below T_c , the interference patterns undergo a dramatic change and regain sharp peaks.

These figures show qualitatively that a Bose condensation transition should be visible with the time-of-flight images. To obtain a more quantitative description, however, it is desirable to have some single-value indicators which change sharply across the BEC transition so that one can characterize this phase transition by measuring the indicators. As possible candidates, we next discuss in detail two quantities: including the visibility of the interference pattern (Sec. 4.2) and the peak width associated with the atomic momentum distribution (Sec. 4.2.4). While both quantities can signal the BEC transition in a reasonably strong global trap, the peak width is a more accurate indication when the global trap becomes weaker. After the condensation transition, both of these two indicators become very insensitive to the variation of the system temperature, so they do not provide a good thermometer. Instead, we suggest measuring the condensate fraction from the bimodal fitting to

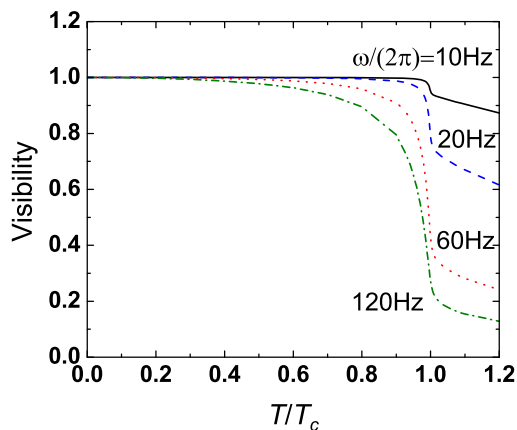


Figure 4.2: The visibility as a function of temperature around the BEC transition temperature T_c for various values of trapping frequencies. Other parameters are the same as those used in Fig. 4.1 with $V_0 = 10E_R$ and $N = 10^5$. Remind that the variation of V_0 is equivalent to that of ω , with a fixed value of $\hbar^2\omega^2/(V_0^{3/4}e^{-2\sqrt{V_0}})$.

the central interference peak, as discussed in Sec. 4.2.5. The measured condensate fraction changes continuously with the temperature, thus giving a good indicator for estimation of temperature in this important system.

4.2.3 Visibility

The visibility of the interference pattern is introduced in [43]. It is defined as the intensity contrast of two characteristic points on the interference pattern [43]

$$v = \frac{n_{\perp}^A - n_{\perp}^B}{n_{\perp}^A + n_{\perp}^B}, \quad (4.8)$$

where n_{\perp}^A and n_{\perp}^B are (column-integrated) atomic intensities at sites A and B , respectively, as shown in Fig. 4.1(a). The point A represents the position of the secondary peak while B is along the circle of the secondary peaks where the intensity takes its minimum value. The visibility defined in this way is clearly independent of the Wannier function [the pre-factor in Eq. (4.3)].

The temperature dependence of the visibility v , especially crossing the BEC transition, is shown in Fig. 4.2 for various values of trapping frequencies. For a very weak

trap ($\omega = 2\pi \times 10$ Hz), the visibility is fairly high ($v > 0.8$) even with temperature considerably larger than T_c . Thus in the limit of a vanishing ω , our result is consistent with those in [47] for free bosons in a homogeneous lattice (without the global trap). However, for large trapping frequencies, as pointed out in [48], the visibility becomes significantly smaller when $T > T_c$, leading to a more substantial drop across the BEC transition. With a trapping frequency around $\omega = 2\pi \times 60$ Hz, the visibility jumps should be evident to observe, as shown in Fig. 4.2. However, the transition is stretched over a wide range of temperatures (the visibility begins to drop starting from a temperature significantly below T_c , see Fig. 4.2), which may make the determination of the transition point from the visibility less accurate. Notice that with the scaling relation, a smaller barrier V_0 corresponds to a larger effective trapping frequency ω . Therefore with a shallower lattice, the change in visibility across the BEC transition becomes larger for free bosons.

For the system temperature above T_c , there is no long-range coherence in the atomic cloud, so the finite visibility of the interference pattern is induced by residual short-range thermal correlations. To understand the different behavior of the visibility, we calculate the short-range thermal correlation function around the trap center with different global trapping potentials. The real space correlation function is defined as

$$C(\mathbf{R}) = \frac{\langle \Psi^\dagger(\mathbf{0})\Psi(\mathbf{R}) \rangle}{\sqrt{\langle \Psi^\dagger(\mathbf{0})\Psi(\mathbf{0}) \rangle \langle \Psi^\dagger(\mathbf{R})\Psi(\mathbf{R}) \rangle}}, \quad (4.9)$$

with $\mathbf{R} = \mathbf{0}$ indicating the trap center. In Fig. 4.3, we show the correlation functions both below and above T_c for different trapping frequencies. Notice that for weak trapping potentials [see, e.g., Fig. 4.3(a)], the correlation function extends to several lattice sites at temperatures above T_c , indicating the presence of thermal short-range coherence. As the trapping frequency increases, the correlation length for a

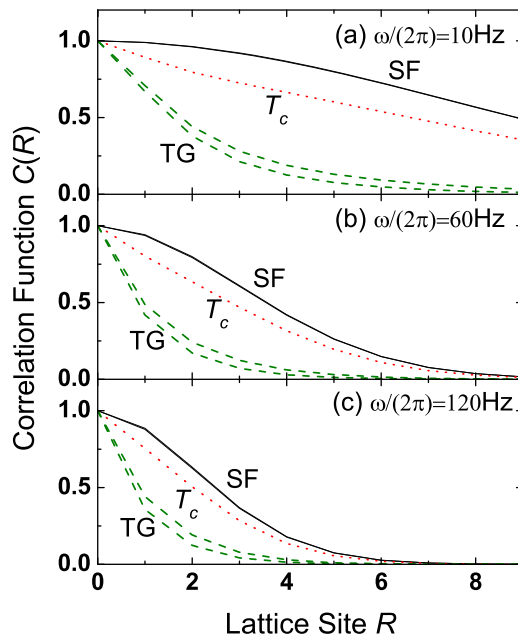


Figure 4.3: Correlation functions around the trap center indicating real space coherence below (for a superfluid, SF) and above (for a thermal gas, TG) the BEC transition temperature, with trapping frequencies (a) $\omega = 2\pi \times 10$ Hz, (b) $2\pi \times 60$ Hz, and (c) $2\pi \times 120$ Hz. Curves in each panel are taken at, from top to bottom, $0.9T_c$ (solid), $0.95T_c$ (solid), $1.0T_c$ (dotted), $1.05T_c$ (dashed), and $1.1T_c$ (dashed), respectively. Parameters used in these plots are $V_0 = 10E_R$ and $N = 10^5$. For reference, the characteristic length of the single particle ground state wavefunction adjusted by effective mass ($L \equiv \sqrt{\hbar/m^*\omega}$) are (in unit of the lattice constant) (a) $L = 3.80$, (b) $L = 1.55$, and (c) $L = 1.09$, respectively.

thermal gas decreases as presented in Fig. 4.3(b) and 4.3(c), consistent with the disappearance of interference peaks as shown in Fig. 4.2(f).

4.2.4 Momentum-space density profile and the peak width

Up to now, we have discussed the visibility characterizing the contrast of the interference pattern. In this subsection, we introduce another single-value quantity, the peak width, which characterizes the sharpness of the interference peak. We notice that while the visibility does not undergo a sudden change across the BEC

transition when the global trap is weak, the width of the central interference peak, by contrast, always shrinks sharply when the condensation takes place. Therefore, the peak width is always a good indicator of the BEC transition independent of the strength of the global trap.

To introduce the peak width, we first look at the atomic momentum distribution, which gives detailed information about the system. From Eq. (4.3), the momentum distributions in other Brillouin zones are simply copies of the distribution in the first Brillouin zone weighted by the given Wannier function, so it suffices to study the atomic momentum profile in the first Brillouin zone. In Fig. 4.4, we plot the column-integrated momentum distribution along one crystallographic axis (e.g., the x -axis) passing through the center of the first Brillouin zone. It is clear that while the density profile is a thermal distribution when $T > T_c$, a bimodal structure starts to appear when a non-zero condensate fraction emerges in the lattice, characterized by a sharp peak at the center of the momentum space surrounded by a flat thermal distribution. The signal of this structural change becomes significant as soon as the system crosses the BEC transition [see Fig. 4.4(b) and (e)].

In order to characterize the sharpness of the atomic momentum distribution in the first Brillouin zone, we introduce the peak width as a single-value parameter. For this purpose, we first define the middle value of $n_{\perp}(k_x, k_y)$ within the first Brillouin zone:

$$n_{\text{mid}} \equiv \frac{1}{2} \left[\max_{(k_x, k_y) \in \text{1BZ}} + \min_{(k_x, k_y) \in \text{1BZ}} \right] n_{\perp}(k_x, k_y). \quad (4.10)$$

In the simplest terms, the peak width w is measured as the radius in momentum space where the (column-integrated) atomic density $n_{\perp}(k_x, k_y)$ first falls to this middle value n_{mid} . In Fig. 4.5, we show the peak width as a function of temperature for various trapping frequencies. Notice that the central peak width decreases monoton-

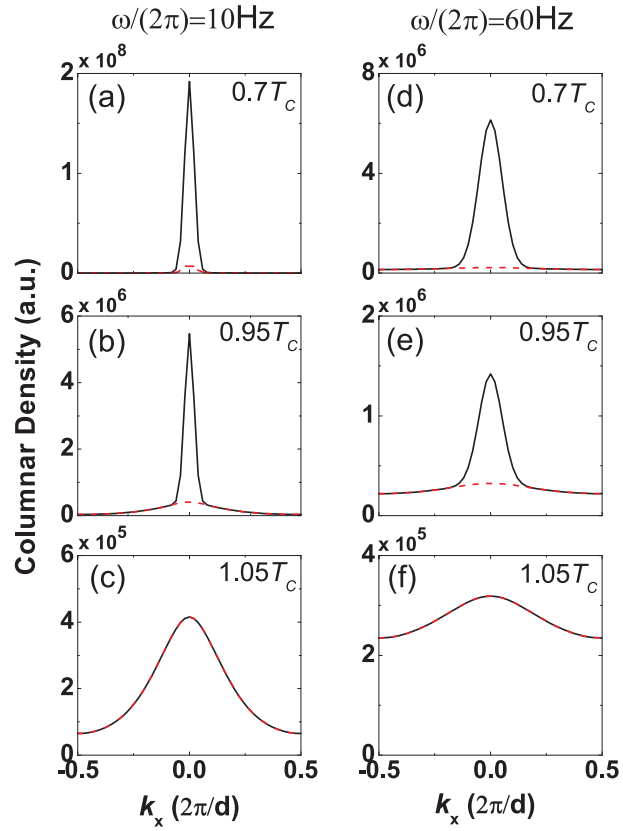


Figure 4.4: Momentum space columnar density along the x -axis in the first Brillouin zone. The left and right panels correspond to the cases of trapping frequencies $\omega = 2\pi \times 10\text{Hz}$ and $2\pi \times 60\text{Hz}$, respectively. Notice that while a thermal distribution is present above T_c [(c) and (f)], a clear bimodal structure starts to appear for temperatures slightly below T_c with only precentral condensate fractions [$n_0 \sim 0.14$ in (b) and ~ 0.09 in (e)]. Here, the solid curves represent the total momentum density profile, and the dashed curves represent the momentum density profile of the normal component. Parameters used in these plots are $V_0 = 10E_R$ and $N = 10^5$.

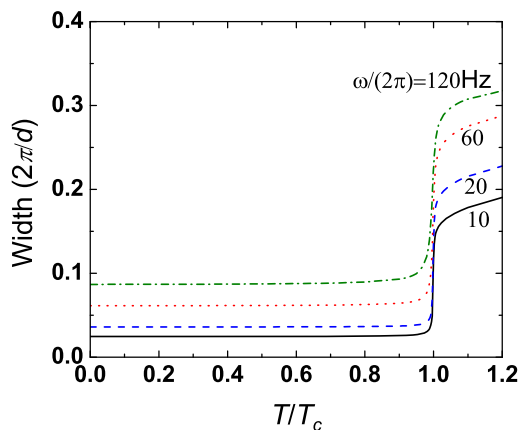


Figure 4.5: The peak width (defined in the text) within the first Brillouin zone, taking across the transition temperature for various values of trapping frequencies. Notice that the sharp and substantial change around T_c occurs for all cases hence serves as a distinctive signature of BEC transition. Parameters used in these plots are $V_0 = 10E_R$ and $N = 10^5$.

ically with temperature, and most importantly undergoes a sharp and substantial change when crossing the transition temperature. This distinct feature is universal for all trapping frequencies, and hence can provide a clear criterion for the phase transition. However, as will be discussed later, the sharpness of the change of central peak width around T_c is guaranteed only for ideal Bose gases. In the presence of atomic interaction, the variation of central peak width may be more flat and extended over a wider range of temperatures.

4.2.5 The condensate fraction as a measure of temperature

From the discussion above, we notice that after the condensation transition, both the visibility and the peak width become almost flat with variation in temperature, as evident in Figs. 4.2 and 4.5. This means that it is hard to get any information about the temperature of the system from the measured values of visibility and peak width. Since temperature is one of the most important quantities for the thermodynamics of the system, it is desirable to have some experimentally measurable indicator which gives a good estimate of the temperature. The momentum density

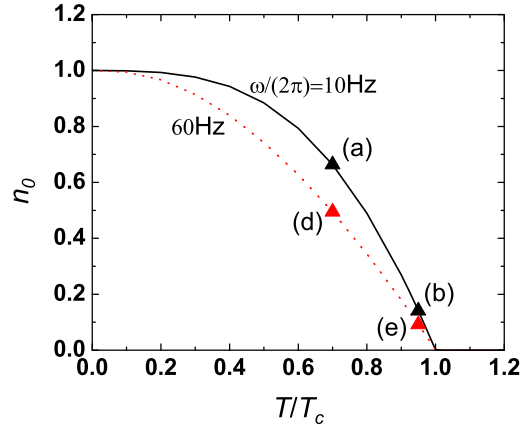


Figure 4.6: The condensate fraction as a function of temperature below the BEC transition. By extracting n_0 from the momentum distribution as shown in Fig. 4.4(a-b) and (d-e), temperatures of such cases can be determined correspondingly (triangles). Parameters used in this figure are $V_0 = 10E_R$ and $N = 10^5$.

profile in principle gives a great deal of information, but it is not a single-value quantity, making it less suitable for direct comparison at different temperatures or for different systems. To overcome this drawback, we note that below T_c , the atomic momentum distribution in the first Brillouin zone always shows a bimodal structure, which actually gives a robust signal for the condensation transition. Furthermore, from the measured momentum density profile, one can always do a bimodal fitting to deduce the atomic fractions in the condensate and in the thermal parts, respectively. The measured condensate fraction can thus serve as a good estimate for the system temperature. In Fig. 4.6, we show the calculated condensate fraction as a function of temperature for this system with two different global trapping frequencies. Notice that the condensate fraction n_0 changes steadily and monotonically as the temperature T varies. From the curve $n_0(T)$ (Fig. 4.6), one can estimate the temperature T through the experimentally measurable n_0 . Therefore, the condensate fraction n_0 gives a single-value quantity which can serve as a criterion for the condensation transition (with $n_0 > 0$), as well as an indicator of the system temperature.

4.3 Interacting Bose Gas in an Inhomogeneous Optical Lattice

In this section, we discuss the more general and practical case where the atoms in an inhomogeneous optical lattice have collisional interactions with each other. Many qualitative features discussed in the last section remain valid in the interacting case. However, the atomic interaction indeed brings up several different properties at a quantitative level. In this section, the emphasis of our discussion is on these differences.

Taking the interaction into account, the time-of-flight images are expected to be modified in two major ways. First, the repulsive interaction between atoms will tend to broaden their spatial distribution in a trap, and hence narrow the corresponding momentum distribution. Second, during the time-of-flight expansion, the remnant atomic interaction transforms the interaction energy into kinetic energy, in particular in the early stage of expansion. As a consequence, the momentum distribution tends to be wider in the final images. The images also become slightly blurred due to the scattering of different interference peaks in momentum space during the expansion. In this section, we will discuss both these points.

For an interacting Bose gas in an inhomogeneous optical lattice, exact solutions as in the non-interacting case can no longer be constructed. Instead, we use the local density approximation (LDA) to treat the inhomogeneity induced by the global trap. When the interaction energy is much larger than the trap energy, each local region of the global trap behaves like a homogeneous system with interacting atoms in a pure optical lattice. The interaction in this local homogeneous lattice is then analyzed under the Hartree-Fock-Bogoliubov-Popov (HFBP) scheme [116, 118]. The validity of this approach is supported by the following considerations. First, the LDA works

well for a large number of atoms in a weak harmonic trap, which is the case for the parameter ranges considered below. Second, the HFBP method should be able to provide a reliable description of weakly interacting Bose systems, except for the region close to a phase transition (associated with the BEC or the Mott transition). For an atomic gas in a global harmonic trap away from the Mott transition, such a questionable region corresponds only to a thin shell in space, and its contribution to the global properties is far less significant.

Under the LDA, we consider an interacting Bose system with a spatially dependent Hamiltonian

$$H = \sum_{\mathbf{k}} (\epsilon_{\mathbf{k}} - \mu) a_{\mathbf{k}}^{\dagger} a_{\mathbf{k}} + \frac{U}{2} \sum_{\mathbf{k}, \mathbf{k}', \mathbf{q}} a_{\mathbf{k}+\mathbf{q}}^{\dagger} a_{-\mathbf{k}}^{\dagger} a_{\mathbf{k}'+\mathbf{q}} a_{-\mathbf{k}'}, \quad (4.11)$$

where $\epsilon_{\mathbf{k}}$ is the dispersion relation defined above, $\mu \equiv \mu(\mathbf{r})$ is the local chemical potential, and $U \equiv U_{\text{bg}} \int |w(\mathbf{r})|^4 d^3\mathbf{r}$ is the on-site interaction rate. For a typical experiment with ^{87}Rb , U_{bg} is related to the s -wave background scattering length $a_s = 5.45 \text{ nm}$ by $U_{\text{bg}} = 4\pi\hbar^2 a_s/m$, and U takes the approximate form $U \approx 3.05 V_0^{0.85} (a_s/d)$, with energy units of the recoil energy E_R [43]. According to the standard HFBP approach, we separate the bosonic operators into two parts:

$$a_{\mathbf{k}} = \psi_0 + \delta_{\mathbf{k}}; \quad a_{\mathbf{k}}^{\dagger} = \psi_0 + \delta_{\mathbf{k}}^{\dagger}, \quad (4.12)$$

where $\psi_0 \equiv \langle a_{\mathbf{0}}^{\dagger} \rangle \equiv \langle a_{\mathbf{0}} \rangle$ represents the condensate component, and $\delta_{\mathbf{k}}$ is the fluctuation around it. After performing the substitution for $a_{\mathbf{k}}$ and $a_{\mathbf{k}}^{\dagger}$ into the original Hamiltonian Eq. (4.11), terms that are cubic and quartic in $\delta_{\mathbf{k}}^{\dagger}$ and $\delta_{\mathbf{k}}$ will be present. These terms are reduced to quadratic forms under the HFBP approximation by employing Wick's theorem. As a result, we obtain a quadratic effective Hamiltonian

H_{eff}

$$\begin{aligned}
H_{\text{eff}} \approx & \left(\epsilon_0 - \mu + \frac{Un_0}{2} \right) n_0 \\
& + \sum_{\mathbf{k}} [\epsilon_{\mathbf{k}} - \mu + 2U(n_{\text{tot}} - n_0)] \delta_{\mathbf{k}}^\dagger \delta_{\mathbf{k}} \\
& + \frac{Un_0}{2} \sum_{\mathbf{k}} \left(\delta_{\mathbf{k}}^\dagger \delta_{-\mathbf{k}}^\dagger + \delta_{\mathbf{k}} \delta_{-\mathbf{k}} + 4\delta_{\mathbf{k}}^\dagger \delta_{\mathbf{k}} \right). \tag{4.13}
\end{aligned}$$

Here, $\epsilon_0 = -6t$ is the energy at the band bottom with t the tunneling rate defined above, $n_0 = \psi_0^2$ is the per site density of the condensate fraction, and n_{tot} is the total number of particles per site. In order to derive the expression above, the saddle point condition is employed to make the coefficients of terms linear in δ vanish, leading to the saddle point equation

$$\mu(\mathbf{r}) = \epsilon_0 - Un_0 + 2Un_{\text{tot}}. \tag{4.14}$$

This equation must be solved self-consistently with the number constraint $n_{\text{tot}} = -\partial\Omega/\partial\mu$, where $\Omega = -(1/\beta) \ln \text{Tr}(e^{\beta H_{\text{eff}}})$ is the thermodynamic potential. This constraint leads to the number equation

$$n_{\text{tot}} = n_0 + \sum_{\mathbf{k} \neq \mathbf{0}} \frac{1}{2} \left[\frac{\epsilon_{\mathbf{k}} - \epsilon_0 + Un_0}{E_{\mathbf{k}}} \coth \left(\frac{\beta E_{\mathbf{k}}}{2} \right) - 1 \right], \tag{4.15}$$

where $E_{\mathbf{k}} = \sqrt{(\epsilon_{\mathbf{k}} - \epsilon_0 + Un_0)^2 - U^2 n_0^2}$ is the quasiparticle dispersion relation.

By fixing the number density per site at the trap center, we can solve Eqs. (4.14) and (4.15) self-consistently to obtain the chemical potential at the trap center μ_0 . This result, together with the LDA relation $\mu(\mathbf{r}) = \mu_0 - V(\mathbf{r})$, allows us to calculate $\mu(\mathbf{r})$, and hence the condensate fraction $n_0(\mathbf{r})$ and quasi-momentum distribution of the non-condensate part $n_{\mathbf{k} \neq \mathbf{0}}(\mathbf{r})$ at arbitrary position in the trap. The overall non-condensate quasi-momentum distribution can thus be obtained by integrating over the whole global trap. For the condensate component, it should be emphasized that

n_0 leads to a delta function at zero momentum, which is an artificial result of LDA. In order to overcome this artifact, one needs to consider explicitly the broadening of the condensate momentum distribution due to the presence of the harmonic trap. This can be done by the following procedure. First, we calculate the condensate fraction distribution $n_0(\mathbf{r})$ over the trap. The condensate wave function then can be well approximated by $\psi_0(\mathbf{r}) = \sqrt{n_0(\mathbf{r})}$ under the Thomas-Fermi approximation [123]. The condensate component of the quasi-momentum distribution is thus given by the Fourier transform of the wave function $\psi_0(\mathbf{r})$. Second, by adding this condensate contribution to that from the normal part, and multiplying by the Wannier function square $|w(\mathbf{k})|^2$ as in Eq. (4.6), we get the resulting momentum-space density distribution.

As in the case of an ideal Bose gas, we next discuss several characteristics of the momentum-space density distribution. In Sec. 4.3.1 and 4.3.2, we discuss the influence of interaction on the atomic momentum distribution inside the trap, especially the associated visibility and the peak width. Then, we calculate in Sec. 4.3.3 the condensate fraction as a quantitative measure of the system temperature. Lastly, in Sec. 4.3.4, we analyze the interaction effect during the time-of-flight expansion, and conclude that this effect does not significantly change the characteristics discussed above.

4.3.1 Visibility of the interference pattern

We show in Fig. 4.7 the visibility of the interference pattern as a function of temperature across the BEC transition. Since the presence of interaction sets another energy scale, the system is not determined by the single parameter of $\hbar^2\omega^2/(tE_R)$, as in the ideal gas case. Instead, we consider various combinations of lattice barriers and trapping frequencies.

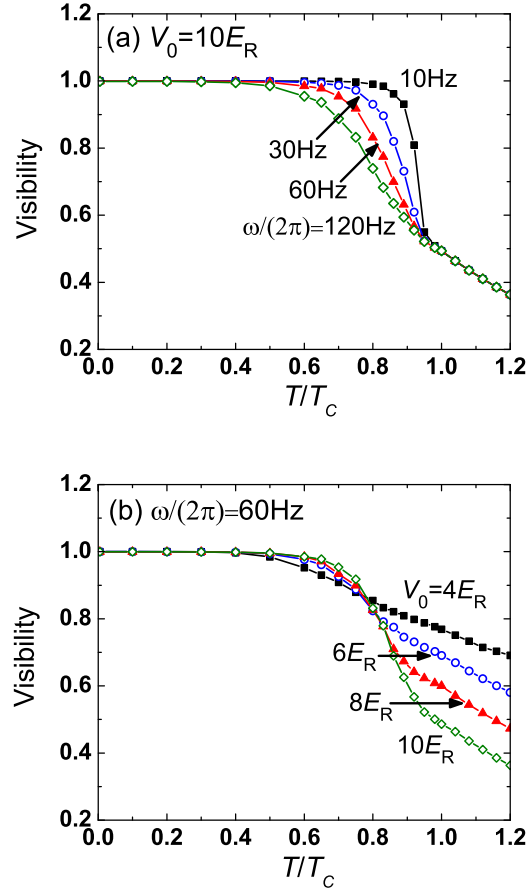


Figure 4.7: The visibility as a function of temperature around the BEC transition temperature T_c for (a) $V_0 = 10E_R$ and (b) $\omega = 2\pi \times 60$ Hz. The number density per site at the trap center is set as $n_{\text{tot}} = 1$, and the total number of particles in the trap is $N \sim 10^4$.

From Fig. 4.7(a), we observe that independent of the strength of the global trap, the thermal visibility with $T \gtrsim T_c$ remains small (with v around or below 0.4). This result is significantly different from the case of an ideal Bose gas, where the thermal visibility can be close to unity for a very weak global trap. After crossing the BEC transition, the visibility clearly increases so that for an interacting Bose gas, a high visibility signifies that the atomic cloud is in the condensate region. However, for a strong global trap (with $\omega \sim 2\pi \times 120$ Hz for instance), the variation of the visibility is not sharp at the transition point, but continues into a fairly wide region below T_c . Thus in this case it becomes less accurate to use the jump in visibility to determine the BEC transition temperature.

Another feature we can read from Fig. 4.7(a) is the convergent behavior of visibility for a thermal gas with the same lattice potential but various values of trapping frequency. This behavior can be understood from the overall quasi-momentum distribution

$$n_{\mathbf{k}} = \int d^3\mathbf{r} n_{\mathbf{k}}(\mathbf{r}) = 4\pi \int_0^\infty dr n_{\mathbf{k}}(r) r^2, \quad (4.16)$$

where the integration is over the whole trap. Under the LDA, the spatial dependence on number density is only through the chemical potential $n_{\mathbf{k}}(\mathbf{r}) = \tilde{n}_{\mathbf{k}}(\mu(\mathbf{r}))$; hence the integration can be rewritten as

$$n_{\mathbf{k}} = 4\pi \left(\frac{m}{2\omega^2} \right)^{3/2} \int_{\mu_0}^0 \varepsilon \tilde{n}_{\mathbf{k}}(\varepsilon) d\sqrt{\varepsilon}. \quad (4.17)$$

For a thermal gas with a certain number density and chemical potential at the trap center, the function $\tilde{n}_{\mathbf{k}}(\varepsilon)$ and hence the integration over ε in the equation above is fixed. Thus all the trap can do is to re-scale the quasi-momentum distribution by a factor of ω^{-3} . For a given optical lattice characterized by a Wannier function, the momentum-space density profile of a thermal gas for various values of ω takes

the same shape; hence all signatures we can read from it must remain unchanged. Notice that since the LDA approach is reliable for all parameter ranges discussed here (with $\omega \lesssim 2\pi \times 120$ Hz), we conclude that this result is the effect of a strong interaction compared to the trapping potential, which cannot be smoothly connected to the non-interacting results.

In Fig. 4.7(b), we show the visibility for different lattice depths with a fixed strength of the global trap. With lower lattice depths, the thermal visibility increases. For $V_0 = 4E_R$, for instance, the visibility varies almost linearly with temperature near the condensation transition (for T from $0.5T_c$ to $1.2T_c$), and a high thermal visibility remains (with $v \sim 0.7 - 0.8$) even when T crosses T_c . This flat behavior makes it difficult to use visibility to detect the condensate region and to identify the transition point for interacting atoms in a shallow lattice.

4.3.2 Momentum-space density profile and the peak width

Having discussed the visibility of interference peaks, we next focus on the momentum distribution in the first Brillouin zone. In Fig. 4.8, we show the column-integrated momentum density profile along one of the crystallographic axes (say, the x -axis). Similar to the case of an ideal Bose gas, a clear bimodal structure appears for temperatures below T_c even when the condensate fraction is still small [see Fig. 4.8(b) with $n_0 \sim 9\%$]. Therefore, the momentum distribution and its bimodal structure sets an unambiguous criterion for the BEC transition, especially when supplemented with the interference pattern from the lattice structure.

To characterize the sharpness of the central peak, we still use the peak width defined above as a single-value parameter. As shown in Fig. 4.9, the peak width significantly reduces across the BEC transition, so a sharp peak with a small width sets a clear indicator that the system is in the condensate region. This conclusion is

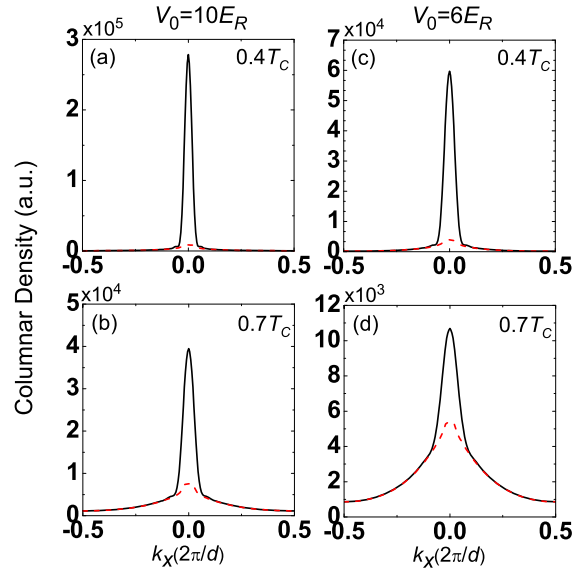


Figure 4.8: Momentum space columnar density along the x -axis in the first Brillouin zone, where clear bimodal structures appear for temperatures below T_c . Here, the solid curves are the total momentum density profile, and the dashed curves are the momentum density profile of the normal component. The trapping frequency used in these plots is $\omega = 2\pi \times 60$ Hz, and the number density per site is unity at the trap center.

qualitatively consistent with the case of an ideal Bose gas as discussed in Sec. 4.2.4. For an ideal Bose gas, the peak width always has a sharp and large jump at the BEC transition point. For an interacting Bose gas, this jump becomes less sharp under certain circumstances. From Fig. 4.9, we notice that the jump of the peak width remains sharp across T_c for weak global traps or for lower lattice depths. However, in a stronger global trap with a higher lattice depth, the decrease of the peak width takes place over a wider range of temperatures, which makes it less accurate for locating the transition point. If one compares Figs. 4.7 and 4.9, it is interesting to note for that for a weak optical lattice, even when the visibility becomes too flat to show a phase transition, the variation of the peak width remains fairly sharp enough to serve as an indicator of the condensation transition.

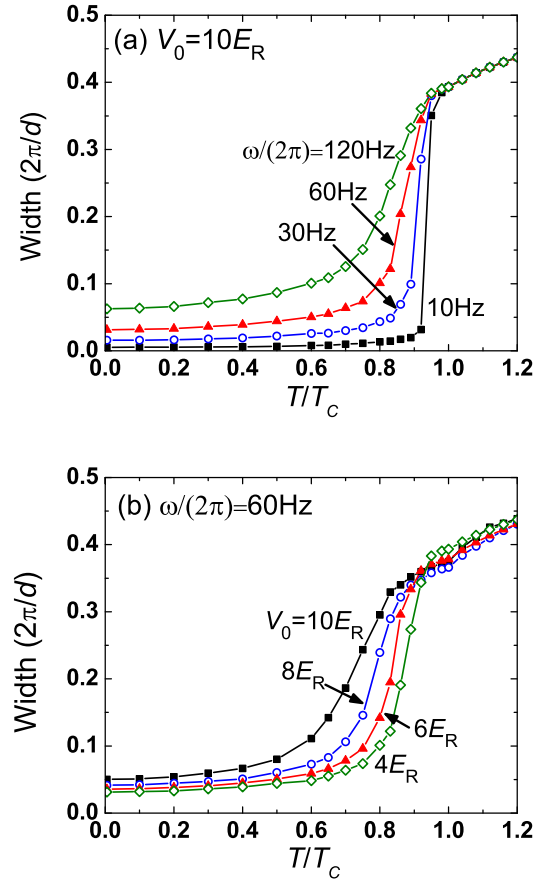


Figure 4.9: The peak width within the first Brillouin zone, taking across the transition temperature for (a) $V_0 = 10E_R$ and (b) $\omega = 2\pi \times 60$ Hz. The number density per site is unity at the trap center.

4.3.3 The condensate fraction

Similar to the ideal Bose gas, when one moves into the condensate region, the visibility and the peak width become insensitive to the variation of temperature. However, the condensate fraction appears to be a monotonic function of temperature and can be used as a convincing thermometer (Fig. 4.10). In experiments, the condensate fraction can be measured through direct bimodal fitting to the momentum density profiles. In Fig. 4.10 we show the condensation fraction as a function of temperature under different lattice barriers. First note that the condensate fraction does not approach unity even when the temperature is down to zero. This result is significantly different from the case of an ideal Bose gas, where at zero temperature all the atoms form a pure condensate. This discrepancy at zero temperature is due to quantum depletion (of the ground state), which always plays a role in an interacting gas. In the zero temperature limit the HFBP approximation used here reduces to the Bogoliubov approach, which has intrinsically taken into account the contribution of quantum depletion. In Fig. 4.11, we show the in-trap zero temperature quantum depletion fraction for various lattice barrier depths. With a higher lattice barrier V_0 , we find that the quantum depletion fraction becomes more significant, consistent with our expectation. In fact, in the case with no optical lattice, the condensate fraction should be small at zero temperature for a weakly interacting dilute gas (with a small gas parameter). In the opposite limit, when the lattice barrier tends to the critical value for the Mott transition, the condensate fraction should deplete to zero. When the quantum depletion is dramatic, the HFBP is no longer a good approximation. However, for the parameter ranges discussed above, even with $V_0 = 12E_R$, the condensate fraction ($\sim 70\%$) still dominates at zero temperature, assuring the validity of the HFBP approximation used throughout this section.

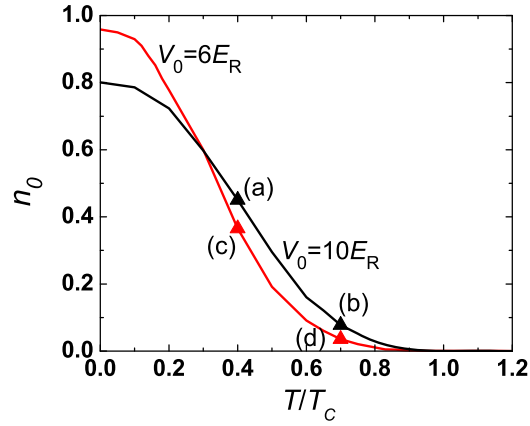


Figure 4.10: The condensate fraction as a function of temperature below the BEC transition, for an interacting Bose gas in an optical lattice with $\omega = 2\pi \times 60$ Hz and different lattice barriers V_0 . The number density per site is unity at the trap center. By comparing with the momentum distribution as shown in Fig. 4.8, temperatures of such a system can be determined correspondingly (triangles).

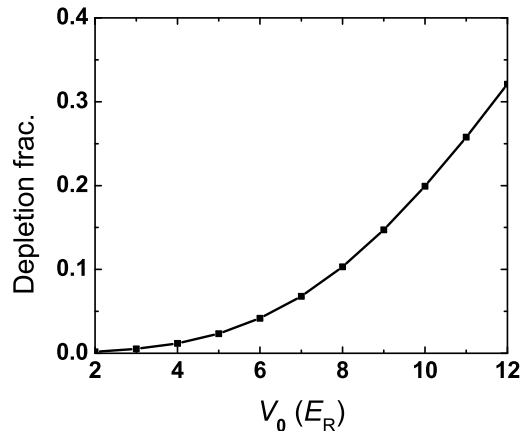


Figure 4.11: The in-trap quantum depletion fraction as a function of the lattice barrier V_0 . The trapping frequency is $\omega = 2\pi \times 60$ Hz. The number density per site at the trap center is unity.

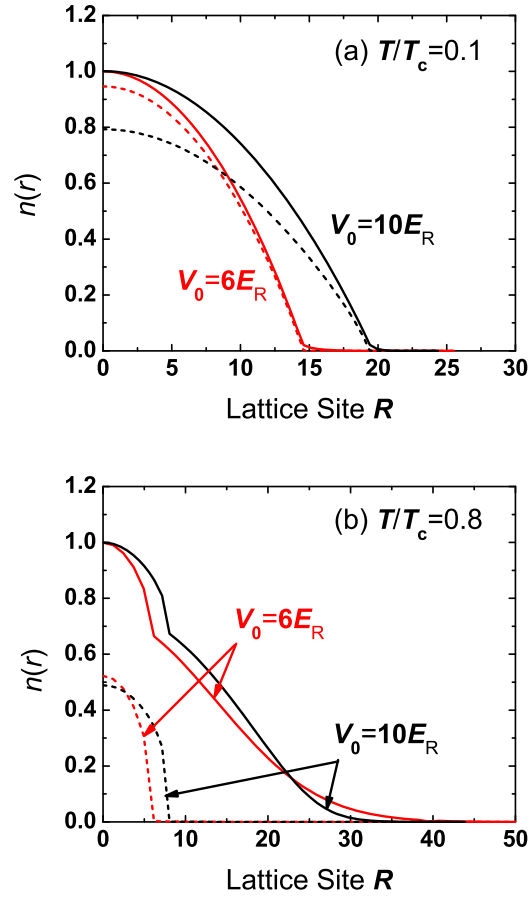


Figure 4.12: The number and condensate density distribution along the radial direction away from the trap center. Two different temperatures are considered as in (a) $T = 0.1T_c$, and (b) $T = 0.8T_c$. The solid curves correspond to the overall density profiles and the dashed curves to the condensate portions. The trapping frequency used here is $\omega = 2\pi \times 60$ Hz. The total number of particles N_{tot} and the number of condensate particles N_0 are respectively (a) $V_0 = 6E_R$ (red): $N_{\text{tot}} = 0.54 \times 10^4$, $N_0 = 0.50 \times 10^4$; $V_0 = 10E_R$ (black): $N_{\text{tot}} = 1.3 \times 10^4$, $N_0 = 1.0 \times 10^4$; (b) $V_0 = 6E_R$ (red): $N_{\text{tot}} = 2.5 \times 10^4$, $N_0 = 2.8 \times 10^2$; $V_0 = 10E_R$ (black): $N_{\text{tot}} = 2.3 \times 10^4$, $N_0 = 6.7 \times 10^2$.

Another interesting feature of the condensate fraction plotted in Fig. 4.10 is the crossing behavior of the two curves for different V_0 at finite temperature. For a homogeneous gas with a certain number density, one would expect a more severe depletion (both quantum and thermal) from the condensate for the higher V_0 case, since both temperature and interaction should play relatively more significant roles. However, this simple trend becomes more complicated in a trapped case. In fact, due to the presence of a global trap, thermal wings emerge at the edge of the trap at finite temperature, while the condensate portion peaks at the trap center. When one calculates the overall condensate fraction, an integration over the whole trap should take the thermal wings into account, and the result will depend on how much the thermal part contributes to the total number. To show this more explicitly, we plot the in-trap number and condensate density profiles in Fig. 4.12 with a fixed total number density at the trap center. At a lower temperature $T = 0.1T_c$, the thermal contribution is negligible, so it is apparent that a higher depletion is observed for higher barriers, as shown in Fig. 4.12(a). At a higher temperature $T = 0.8T_c$, the thermal part becomes significant and one observes a more extended thermal tail in the lower barrier case with $V_0 = 6E_R$, as shown in Fig. 4.12(b). This greater thermal contribution to the total number makes the condensate part relatively smaller and leads to a smaller condensate fraction. Therefore, the crossing behavior of n_0 as shown in Fig. 4.10 is a consequence of the different distributions of the condensate and the thermal portions in an inhomogeneous global trap.

4.3.4 Interaction effects during the time-of-flight expansion

Up to now, we have calculated the atomic momentum distribution inside the trap and have neglected modification of this distribution caused by the atomic interaction during the time-of-flight expansion. During the expansion of the atomic cloud, the

initial interaction energy is transferred to the kinetic energy, which tends to broaden the momentum distribution [124]. This influence is most evident for the condensate part, due to its high number density and narrow initial momentum distribution. The influence on the momentum distribution of the thermal and the non-condensate part is negligible, as confirmed by experiments [48], since this part has a broad initial momentum distribution already, and the weak atomic collisions are unlikely to cause any significant modification. In the following, we only discuss influence of the atomic collisions on the condensate part of the momentum distribution.

After turnoff of the optical lattice and the confining potential, the atomic cloud undergoes a free expansion in space, and the expansion of the condensate part can be well described by a time dependent Gross-Pitaevskii (TDGP) equation

$$i\hbar\partial_t\Psi(\mathbf{r}, t) = \left(-\frac{\hbar^2\nabla_{\mathbf{r}}^2}{2m} + U|\Psi(\mathbf{r}, t)|^2 \right) \Psi(\mathbf{r}, t). \quad (4.18)$$

The initial condition $\Psi(\mathbf{r}, t = 0)$ (t is the expansion time) is given by the equilibrium condensate wave function inside the optical lattice and global trap, which has been calculated with the method detailed in the above. Note that only for the condensate part we use the TDGP to evolve its momentum distribution.

It is easier to understand the consequence of this evolution by looking at the TDGP equation in the momentum space. The Fourier transform of Eq. (4.18) gives

$$i\hbar\partial_t\Psi_{\mathbf{k}}(t) = \frac{\hbar^2k^2}{2m}\Psi_{\mathbf{k}}(t) + U\sum_{\mathbf{k}',\mathbf{q}}\Psi_{-\mathbf{k}+\mathbf{q}}^\dagger(t)\Psi_{-\mathbf{k}'+\mathbf{q}}(t)\Psi_{\mathbf{k}'}(t). \quad (4.19)$$

Clearly without atomic collisions (the U term), the momentum distribution $|\Psi_{\mathbf{k}}(t)|^2$ remains unchanged. The atomic collisions transfer a pair of atoms from momenta $(\mathbf{k}', -\mathbf{k}' + \mathbf{q})$ to $(\mathbf{k}, -\mathbf{k} + \mathbf{q})$, modulating the overall momentum distribution.

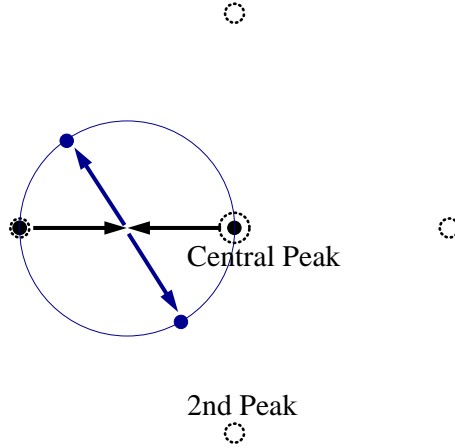


Figure 4.13: Illustration of the scattering between atoms from different peaks (the central and the secondary). This process leads to blurring of the interference peaks with a characteristic blurring pattern.

To understand the consequence of the collision induced momentum transfer, we note that the initial condensate momentum distribution has a number of peaks, one in each Brillouin zone. As the central peak in the first Brillouin zone (with \mathbf{k} close to zero) is the highest one, the scattering of pairs of atoms around the first peak satisfying the momentum conservation has the largest contribution to the collision effect. Around the central peak, the wave function $\Psi_{\mathbf{k}}(t)$ has approximate spherical symmetry, and the evolution of the momentum distribution around the central peak by the TDGP equation has been calculated and shown in [49]. The condensate peak becomes somewhat lower and broader; however, its width is typically still significantly less than the width of the thermal cloud, and a bimodal structure of the momentum distribution remains clearly visible. Thus the collision during the time-of-flight expansion has some quantitative influence on the peak width we calculated before, but the effect is not large and should not change the qualitative discussions in the last sections. In particular, as the bimodal structure remains clearly observable, we do not expect that the condensate fraction measured through the bimodal fitting to the momentum distribution has any significant change due to

the collision effect during the expansion.

Taking into account effects of the next order, the atom in the central peak can collide with another atom in the secondary peak, and scatter to other directions in momentum space. The momentum difference between the central peak and the secondary peak is given by \mathbf{G} (\mathbf{G} is related to the lattice constant d through $|\mathbf{G}| = 2\pi/d$), so the kinetic energy difference corresponds to a large energy scale $\hbar^2|\mathbf{G}|^2/(2m)$, which is typically larger than the interaction strength during the expansion (the latter can be estimated by $Un(t)$, where $n(t)$ is the instantaneous atomic density at the collision). Therefore, to be effective, the collisions need to satisfy momentum conservation as well as an approximate energy conservation in momentum space. As a consequence, for atoms with incoming momenta around 0 and G (corresponding to the central and the secondary peaks, respectively), the outgoing atoms are centered around a spherical surface in the momentum space as shown in Fig. 4.13 (with momenta $(\mathbf{k}', -\mathbf{k}' + \mathbf{G})$, where $\mathbf{k}'^2 + (-\mathbf{k}' + \mathbf{G})^2 \approx |\mathbf{G}|^2$). The sphere has origin at $\mathbf{k} = \mathbf{G}/2$ and a radius of $|\mathbf{G}|/2$. This collision effect causes some blurring of the original peaks. Since the scattered atoms are dominantly around a sphere in momentum space, the blurring caused by scattering yields some characteristic momentum distribution pattern. Experimentally, by looking at such a pattern, one may measure and constrain the magnitude of collision effects during the time-of-flight expansion.

At high orders, there could also be scattering between different secondary peaks as well as scattering between the central and even higher order peaks. Although this scattering can change some of quantities we calculate before, we expect these modifications to be small.

4.4 Chapter Summary

In summary, we have discussed ideal and interacting Bose gases in an inhomogeneous optical lattice within a global harmonic trap. By explicitly calculating the momentum distribution, we have studied several possible signatures of the BEC transition in a lattice based on the common detection technique of time-of-flight imaging. For parameters of relevance to the current experiments, a large visibility, a substantial decline of the peak width, and the appearance of a bimodal structure for the central peak can all be used as signals of the condensation transition as one decreases the temperature. For some other parameters, the thermal visibility could be significant, and in such a case the latter two criteria will work better. In particular, the appearance of a bimodal structure for the momentum distribution is a robust signal associated with the condensation transition in both free space and lattice (in the lattice case, the interference peaks give further information about the underlying lattice structure).

After the condensation transition, both the visibility and the peak width become insensitive to variation in temperature, so they cannot serve as practical thermometers. Instead, one may measure the condensate fraction by a bimodal fitting to the atomic momentum distribution. The condensate fraction changes steadily with temperature, and may work as a good experimental indicator of the system temperature by comparing with the results from theoretical calculations.

CHAPTER V

Large-scale Quantum Computation in an Anharmonic Linear Ion Trap

5.1 Overview

Trapped atomic ions have been regarded as one of the most attractive candidates for the realization of a quantum computer, owing to their long-lived internal qubit coherence and strong laser-mediated Coulomb interaction [14, 15, 53, 125, 126]. Soon after J. I. Cirac and P. Zoller’s first two-qubit gate proposal using trapped ions in 1995 [53], a first two-qubit logic gate was also implemented by C. Monroe *et al.* between the quantized motional mode and the internal state of a single ion [127]. A first two-ion logic gate was realized in 2003 by F. Schmidt-Kaler *et al.* based on the Cirac-Zoller protocol [128]. Various improved protocols have been presented to eliminate cumbersome experimental requirements. For example, in quantum gates based on spin-dependent forces, the information of internal states is not directly transferred to a specific motional mode, thus eliminating the dependence on the noisy thermal states [54, 57, 129]; based on fast pulses, a quantum gate can be operated orders of magnitude faster than the trap period, and can work outside the Lamb-Dicke regime [58, 59, 130]. Other proposals suggest using more strongly confined transverse modes, relaxing the cooling requirement considerably [60]; arbitrary-speed gate operation can be achieved through design of laser pulse shapes [59–61]. In

addition to the development of the quantum gate technology, other experimental achievements include realization of entangled states up to eight particles [131, 132], creation of a six-atom ‘Schrödinger cat’ state [133], entanglement of two distant ionic qubits [134], and quantum teleportation [135, 136].

A next-step mission is to increase the number of ion qubits. This, however, is not a simple task because a large-scale system introduces increasing complications such as trap architecture and growth in number of sidebands. The relevant discussion is in Sec. 5.2, and this work is presented to overcome possible difficulties.

The structure of this chapter is outlined as follows. Sec. 5.2 briefly discusses the scalability issue by summarizing major difficulties in large-scale quantum computing, and the proposals presented from other groups. In Sec. 5.3 we propose an architecture using an anharmonic trap potential to stabilize a uniform ion crystal, meanwhile making the gate designing problem “translationally symmetric”. In Sec. 5.4 we demonstrate implementation of a transverse-mode two-qubit gate using a pulse shaping scheme [60, 61]. Sec. 5.5 discusses possible sources of error and estimate their effects.

5.2 Scalability

The linear RF (Paul) trap has been the workhorse for ion trap quantum computing, with atomic ions laser-cooled and confined in one-dimensional crystals [14, 15, 53, 125] (although there are proposals for the use of two-dimensional crystals in a Penning trap [137] or an array of microtraps [138]). However, scaling the linear ion trap up to large numbers of ions poses significant difficulties [14, 125]. As more ions are added to a harmonic axial potential, a structural instability causes the linear chain to buckle near the middle into a zigzag shape [139, 140], and the resulting

low-frequency transverse modes and the off-axis RF micromotion of the ions makes gate operation unreliable and noisy. Further, most of the logic gate proposals rely on the resolved-sideband limit, i.e. the internal states must be only coupled to a specific motional mode [53, 54, 57, 129]. Even in a linear chain with many ions, the increasingly complicated motional mode spectrum makes it difficult to resolve individual modes for quantum gate operations, and to sufficiently laser cool many low-frequency modes. One approach is to operate with small linear ion chains and multiplex the system by shuttling ions between multiple chains through a maze of trapping zones, but this requires complicated electrode structures and exquisite control of ion trajectories [14, 141]. Another promising approach is through mediation with photons, the so-called quantum networking, which connects an arbitrary number of small ion traps through optical methods. However this relies on very efficient quantum interfacing technology [142, 143].

We propose a new approach to ion quantum computation in a large linear architecture based on several ideas. First, we claim that an anharmonic axial trap provided by static electrode potentials can more easily stabilize a single linear crystal containing a large number of ions. By making the chain uniform, the gate design problem becomes more independent of the location in a trap. Second, tightly-confined and closely-spaced transverse phonon modes can mediate quantum gate operations more robustly at relatively high temperature. Meanwhile, rather than going to the resolved-sideband limit, transverse-mode gates take all modes into consideration and a systematic method is developed to design such gates. Third, gate operations on the large ion array exploit the local character of the laser-induced dipole interaction that is dominated by nearby ions only. This simplifies to a great extent the design complexity [69].

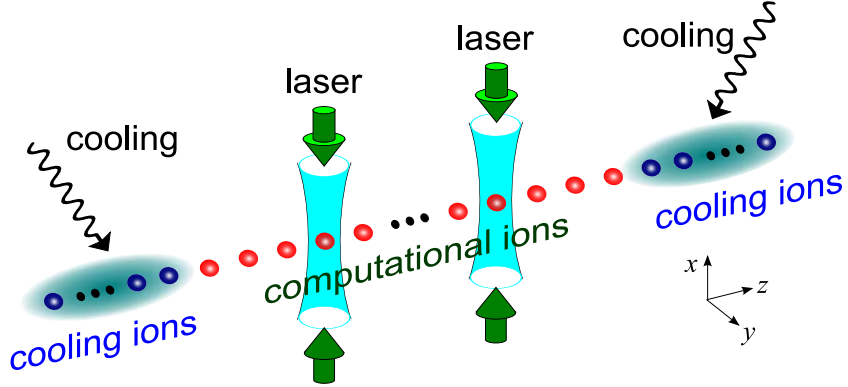


Figure 5.1: Linear architecture for large scale quantum computation, where lasers address individual ions and couple to local modes of the ions, while the edge ions are continuously Doppler laser-cooled. In a large ion chain, more efficient sympathetic cooling could be achieved with cooling ions sparsely distributed in the ion chain.

5.3 Anharmonic Architecture

The proposed ion architecture is illustrated in Fig. 5.1. It is a large linear array where the strong confinement in the transverse (x, y) direction is provided by the ponderomotive Paul trap with an effective potential of the form $V(x, y) = (m\omega_x^2 x^2 + m\omega_y^2 y^2)/2$, where m is the mass of each ion. The ions are initially Doppler cooled, with a number of ions at the edges of the chain continuously Doppler cooled in order to overwhelm any heating that occurs during the gate operation. The middle portion and majority of the ion chain is used for quantum computation. Given an appropriate axial static potential $V(z)$ from the axially-segmented electrodes, we assume these computational ions are distributed nearly uniformly, with a neighboring distance of about $\sim 10\mu\text{m}$. This enables efficient spatial addressing with focused laser beams along the transverse direction for quantum gate operations.

When the axial potential takes the conventional harmonic form $V(z) = m\omega_z^2 z^2/2$, the ion array is subject to the well-known zigzag transition unless the trap anisotropy is at least $\omega_{x,y}/\omega_z > 0.77N/\sqrt{\log N}$ [14, 140, 144], where N is the number of ions. As N becomes large, this structural instability occurs first at the minimal distance at the

trap center due to the spatial inhomogeneity of the ion distribution. When the ions under a similar trap anisotropy are instead uniformly spaced by neighboring distance d_0 , it is easy to see that the linear structure is always stable even for an infinite chain so long as $\omega_{x,y}^2 > 7\zeta(3)e^2/(2md_0^3) \approx 4.2e^2/(md_0^3)$, where $\zeta(l)$ is the Riemann Zeta function and e is the charge of each ion. Therefore, a large linear structure can be more easily stabilized so long as static potentials from the trap electrodes are designed to accommodate equally-spaced ions. The uniformity of the distribution is critical for scaling because the minimum ion spacing can be kept constant to avoid the zigzag transition, while at the same time the maximum ion spacing does not grow, as is required for operating entangling gates efficiently across the whole chain (described below).

To illustrate the general method, we here consider an explicit example with a quartic potential $V(z) = \alpha_2 z^2/2 + \alpha_4 z^4/4$ that can be realized with a simple five-segment electrode geometry as shown in Fig. 5.2(a). Under a quartic trap $V(z)$, the axial equilibrium position z_i of the i th ion can be obtained by solving the force balance equations $\partial U/\partial z_i = 0$, where $U = \sum_i [V(z_i) + V(x, y)] + \sum_{i<j} e^2/|\mathbf{r}_i - \mathbf{r}_j|$ is the overall potential including the ions' mutual interactions. We optimize the dimensionless ratio $B = |\alpha_2/e^2|^{2/3}(\alpha_2/\alpha_4)$ characterizing the axial potential to produce a nearly-uniformly spaced crystal. To be concrete, we consider an array of 120 ions, with 10 ions at each edge continuously laser cooled and 100 qubit ions in the middle for coherent quantum gate operation. We solve the equilibrium positions of all the ions under $V(z)$ and minimize the variance in ion spacing $s_z = \sqrt{\frac{1}{100} \sum_{i=11}^{110} (\Delta z_n - \overline{\Delta z_n})^2}$ for the qubit ions, where Δz_n is the distance between the n th and $(n+1)$ th ion in the chain and $\overline{\Delta z_n}$ denotes its average. The variance in spacing is shown in Fig. 5.2(b) as a function of the parameter B . The value of s_z is fairly insensitive to B

and reaches a minimum when $B \approx -6.1$. Here, the distribution of ion spacing z_n is shown in Fig. 5.2(c), which is remarkably homogeneous for the qubit ions even though we have optimized just one control parameter: $s_z/\overline{\Delta z_n}$ deviates by only 3% over the entire crystal. In this configuration, if we take $\overline{\Delta z_n} = 10 \mu m$ for atomic Yb⁺ ions, we only need a transverse center-of-mass frequency $\omega_{x,y}/2\pi > 221$ kHz to stabilize the linear structure. In this paper, we actually take $\omega_x/2\pi = 5$ MHz, as is typical in experiments [64], and such transverse confinement would be able to stabilize linear chains with thousands of ions under an optimized quartic potential. We note that the ion spacing can be made even more uniform by adding higher order multipole potentials.

5.4 Gate Design

We now describe quantum gate operations with this large ion chain, mediated by many transverse phonon modes. Given the equilibrium positions of the ions, we can efficiently determine all axial and transverse phonon modes. We then apply a spin-dependent laser force, with the resulting interaction Hamiltonian [59, 61]

$$H = \sum_n \hbar \Omega_n(t) \sigma_n^z \cos(|\Delta \mathbf{k}| q_n + \mu t), \quad (5.1)$$

where the transverse displacement q_n of the n th ion in the x direction is expressed in terms of phonon modes a_k with eigenfrequency ω_k and the normal mode matrix b_n^k by $q_n = \sum_k b_n^k \sqrt{\hbar/(2m\omega_k)} (a_k^\dagger e^{i\omega_k t} + a_k e^{-i\omega_k t})$. The normal mode matrix b_n^k and its eigenfrequency ω_k are determined by solving the eigen-equations $\sum_n A_{in} b_n^k = \omega_k^2 b_i^k$, where $A_{in} \equiv \partial^2 U / \partial x_i \partial x_n$ are calculated at the ions' equilibrium positions z_i . In Eq. (5.1), σ_n^z is the Pauli spin operator for the n th ion, $\Omega_n(t)$ denotes the Rabi frequency of the laser pulse on the n th ion with detuning μ from the qubit resonance, and the effective laser momentum kick $\Delta \mathbf{k}$ is assumed to be along the transverse x

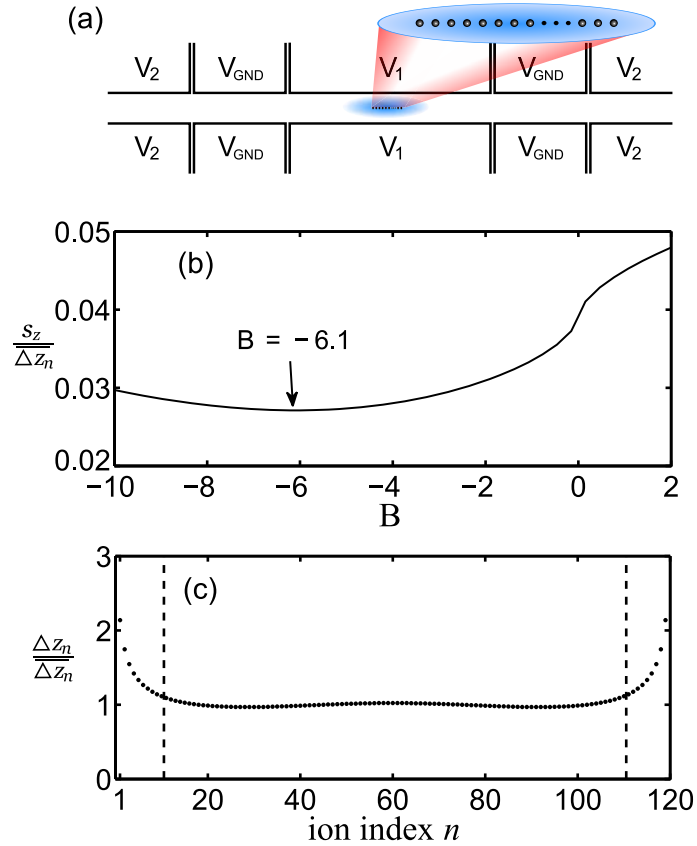


Figure 5.2: (a) Sample five-segment linear ion trap with voltages V_i ($i = 1, 2$) to produce a quartic axial potential. The ions are confined in the central segment. (b) The variance of the ion spacings s_z in a linear quartic trap as a function of the trap parameter B that characterizes the ratio of quadratic to positive-quartic nature of the potential. (c) The distribution of the ion spacing at the optimum value $B = -6.1$. The computational ions are within the dashed lines, where the spacing is essentially uniform.

direction. (For twin-beam stimulated Raman laser forces and hyperfine state qubits, the effective laser kick carries momentum along the difference wavevector $\Delta\mathbf{k} \equiv \mathbf{k}_1 - \mathbf{k}_2$ of the two beams.) Due to the strong transverse confinement, the Lamb-Dicke parameter $\eta_k \equiv |\Delta\mathbf{k}| \sqrt{\hbar/(2m\omega_k)} \ll 1$, and the Hamiltonian H can be expanded as $H = -\sum_{n,k} \hbar\chi_n(t)g_n^k(a_k^\dagger e^{i\omega_k t} + a_k e^{-i\omega_k t})\sigma_n^z$ with $g_n^k = \eta_k b_n^k$ and $\chi_n(t) = \Omega_n(t) \sin \mu t$ (the effect of higher-order terms in the Lamb-Dicke expansion will be estimated in Sec. 5.5). The corresponding evolution operator is given by [61]

$$U(\tau) = \exp \left[i \sum_{n,k} [\alpha_n^k(\tau) a_k^\dagger + \alpha_n^{k*}(\tau) a_k] \sigma_n^z + i \sum_{m < n} \phi_{mn}(\tau) \sigma_m^z \sigma_n^z \right], \quad (5.2)$$

where $\alpha_n^k(\tau) = \int_0^\tau \chi_n(t) g_n^k e^{i\omega_k t} dt$ characterizes the residual entanglement between ion n and phonon mode k and $\phi_{mn}(\tau) = 2 \int_0^\tau dt_2 \int_0^{t_2} dt_1 \sum_k g_m^k g_n^k \chi_m(t_2) \chi_n(t_1) \sin \omega_k(t_2 - t_1)$ represents the effective qubit-qubit interaction between ions m and n .

For a two-qubit gate on an ion pair i and j , we direct laser light exclusively on these two ions ($\Omega_i(t) = \Omega_j(t) \equiv \Omega(t)$ and all other $\Omega_n(t) = 0$), and the evolution operator reduces to the standard controlled π -phase (CP) gate for $\alpha_n^k(\tau) = 0$ and $\phi_{jn}(\tau) = \pi/4$. For a large ion crystal, the residual entanglement with the motional modes cannot be eliminated completely, but we can minimize the resulting gate infidelity by optimizing the laser pulse shape $\Omega(t)$ [61]. Assuming each phonon mode k is cooled to temperature T_k , the infidelity of the CP gate from the residual motional entanglement is given by $\delta F = [6 - 2(\Gamma_i + \Gamma_j) - \Gamma_+ - \Gamma_-]/8$ [61], where $\Gamma_{i(j)} = \exp[-\sum_k |\alpha_{i(j)}^k(\tau)|^2 \bar{\beta}_k/2]$, $\Gamma_\pm = \exp[-\sum_k |\alpha_i^k(\tau) \pm \alpha_j^k(\tau)|^2 \bar{\beta}_k/2]$, and $\bar{\beta}_k = \coth(\hbar\omega_k/k_B T_k)$.

To minimize the gate infidelity δF , we break the laser pulse on the two ions into uniform segments of constant intensity as shown in Fig. 5.3(b) and optimize the values $\Omega^{(i)}$ ($i = 1, \dots, M$) over M equal-time segments [61] (see Appendix A). The

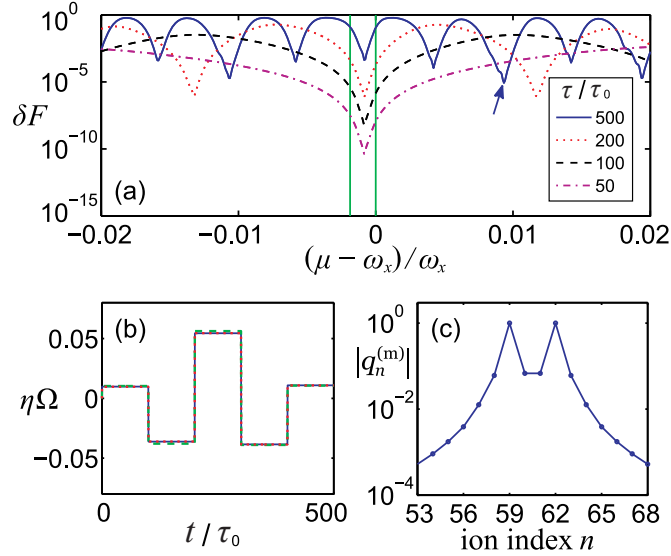


Figure 5.3: (a) The gate infidelity δF as a function of the laser detuning μ from the qubit resonance, with optimized Rabi frequencies over $M = 5$ equal segments of the laser pulse. Different curves correspond to different gate times. The 120 transverse phonon modes are all distributed within the narrow frequency range indicated by the two vertical lines. (b) The shape of the laser pulse $\eta\Omega$ (in units of ω_x) that achieves the optimal fidelity (with $\delta F = 8.5 \times 10^{-6}$), at the detuning shown by the arrow in (a) (with $(\mu - \omega_x)/\omega_x = 9.3 \times 10^{-3}$) and the gate time $\tau = 500\tau_0$. The dashed (or dotted) lines represent the approximate optimal solutions of the laser shape where only 4 (or 8) ions (from the 59th to 62nd or the 57th to 64th, respectively) are allowed to vibrate and all the other ions are fixed in their equilibrium positions. This approximation does not significantly change the optimal laser pulse shape compared to that of the exact solution (represented by the solid line) where all ions are allowed to vibrate, so the gate is essentially local and the gate complexity does not depend on the crystal size. (c) The relative response of the ions for the gate shown in (b) (characterized by the largest spin-dependent shift $|q_n^{(m)}|$ during the gate time τ). We take a relative unit where $|q_n^{(m)}|$ for the target ions haven been normalized to 1. The fast decay of the response as one moves away from the target ions (59th and 62nd) shows that the gate involves vibration of only local ions.

control of $\Omega(t)$ from one segment to the next can easily be accomplished with optical modulators. (Alternatively, we can modulate the detuning μ of the laser pulse as a control parameter.) After optimization of $\Omega^{(i)}$, the infidelity δF is shown as a function of the detuning μ in Fig. 5.3(a) for $M = 5$ segments. For this example, we perform a CP gate on the 59th and 62nd ions in this 120-ion chain. With an appropriate choice of $\Omega^{(i)}$ and μ , the infidelity can be made negligible (well below 10^{-5}). For this calculation, we assume Doppler cooling for all modes and take gate times τ in the range $50\tau_0$ to $500\tau_0$ where $\tau_0 = 2\pi/\omega_x = 0.2\mu s$ is the period of transverse harmonic motion. The gate can certainly be faster with stronger laser beams (there is no speed limit), and with a faster gate, the control becomes easier as the gate becomes more localized (Fig. 5.3).

Interestingly, we use only a few control parameters ($M = 5$ segments) to perform a high-fidelity gate that involves excitation of hundreds of transverse phonon normal modes. This is possible because the gate has a local character where the contribution to the CP gate comes primarily from the spin-dependent oscillations of the ions close to the target ions. To show this, we plot the response of each ion in Fig. 5.3(c) during the gate operation. Note that the displacement q_n of the n th ion is spin-dependent during the gate, and we can use its largest magnitude $\left|q_n^{(m)}\right|$ over the gate time τ to characterize the response of ion n , as is shown in Fig. 5.3(c). The ion response decays very fast from the target ions (59th and 62nd in this case) and can be safely neglected after a distance of a few ions. Thus during a gate, only the motion of ions near the target ions is important, and the other ions largely remain in their equilibrium positions. The resultant control parameters from this approximation are almost identical to those shown in Fig. 5.3(b). Owing to the local character of the gate, the complexity of a gate operation does not depend on the chain size, and we

can perform gates in parallel on ions in different regions of a large chain.

As we use primarily the quasi-local phonon modes for the gate operations, we assume only local entangling gates where the distance between the target ions is small compared with the length of the whole ion chain. (For distant quantum computing, gate operations can be implemented through the aid of a series of mediate local SWAP gates.) Recent studies have shown that with only nearest-neighbor entangling gates in a two-dimensional (2D) lattice, the error threshold for fault-tolerant computation can still be very good, close to the level of one percent [145, 146]. In a one dimensional (1D) ion chain, if we perform gates with distance up to \sqrt{N} (which is still relatively local compared with the size N of the ion chain), this simulates a 2D system, and the error threshold for this case should be as least as good as the 2D case with nearest neighbor entangling gates. Moreover, in the 1D case, it is even possible to perform fault-tolerant quantum computing with only next-to-nearest-neighbor entangling gates [147, 148], albeit with a more demanding threshold.

5.5 Other Imperfections

We now discuss several sources of noise for gates in a large ion crystal and show that their effects are negligible. First, the axial ion modes have large phonon occupation numbers under Doppler cooling alone, and the resulting thermal spread in position along the axial direction can degrade the effective laser interaction. For example, the lowest axial mode in a 120-ion chain of Yb^+ ions with a spacing $\bar{z} \sim 10\mu\text{m}$ has a frequency of only $\omega_{L0}/2\pi = 9.8$ kHz and a mean thermal phonon number $\bar{n}_0 \approx \gamma/\omega_{L0} \approx 10^3$ under Doppler laser cooling (radiative half-linewidth $\gamma/2\pi = 10$ MHz). We assume the quantum gate laser beams are directed along the transverse direction with an axial Gaussian laser profile $\Omega(z) \propto e^{-(z/w)^2}$ centered on each ion.

The beam waist is taken as $w = \bar{z}/2.5 \approx 4\mu m$ so that the cross-talk error probability between adjacent ions is $P_c = e^{-2(\bar{z}/w)^2} < 10^{-5}$. The position fluctuation δz_n of the n th ion causes the effective Rabi frequency to fluctuate, resulting in a gate infidelity $\delta F_1 \approx (\pi^2/4) (\delta\Omega_n/\bar{\Omega}_n)^2 \approx (\pi^2/4) (\delta z_n/w)^4$. The fluctuation δz_n can be calculated exactly from summation of contributions of all the axial modes, and its value is almost independent of the index n for the computational ions (see Appendix B). Under Doppler laser-cooling, $\overline{\delta z_n} \approx 0.26\mu m$ and the corresponding infidelity is $\delta F_1 = 4.4 \times 10^{-5}$. The position fluctuation of the ions may also lead to anharmonic ion motion, whose contribution to the gate infidelity can be estimated by $\delta F_2 \sim (\delta z_n/\bar{z})^2 \sim 6.8 \times 10^{-4}$. Finally, in the transverse direction we estimate the infidelity caused by higher-order expansions in the Lamb-Dicke parameter. As all the transverse modes have roughly the same frequency $\omega_k \approx \omega_x$, the effective Lamb-Dicke parameter for the transverse modes is $\eta_x = |\Delta\mathbf{k}| \sqrt{\hbar/2m\omega_x} \approx 0.038$ for Yb^+ ions at $\omega_x/2\pi = 5$ MHz, with each mode containing a mean thermal phonon number $\bar{n}_x \approx 2.0$ under Doppler cooling. The resultant gate infidelity is estimated to be $\delta F_3 \approx \pi^2\eta_x^4 (\bar{n}_x^2 + \bar{n}_x + 1/8) \approx 7 \times 10^{-4}$ [56, 60]. Note finally that sideband cooling is possible in the transverse direction as all the modes have nearly the same frequency, thus reducing the gate infidelity due to transverse thermal motion by another order of magnitude.

5.6 Chapter Summary

In summary, we have shown through explicit examples and calculations that it is feasible to stabilize large linear ion crystals where the gate complexity does not increase with the size of the crystal and the gate infidelity from thermal fluctuations can be made negligibly small under routine Doppler cooling. The results suggest

a realistic prospect for realization of large scale quantum computation in a simple linear ion architecture.

CHAPTER VI

Quantum Simulation of Ising Magnets with Trapped Ions

6.1 Overview

Recently there has been considerable interest in quantum simulation based on trapped ions. The ion trap system has been found suitable for implementation of various many-body Hamiltonians, such as the spin models [62–65], the Bose-Hubbard model [65, 149], the spin-boson models [150], neural networks [151], the quantum phase transitions of polaritons [152] and Bose-Einstein condensation of phonons [153]. For simulation of the Ising models, the utility of ion trap systems has been demonstrated for $N = 2$ ions [63], and quite recently for $N = 3$ ions [70]. The three-ion case is the smallest network that shows frustration, i.e., competing interactions that cannot satisfy every bond energetically. Scaling up to a large frustrated network is possible. As it has been reported that frustration can lead to complexity of magnetic orders [154, 155] and plays an important role in exotic materials such as quantum spin liquids and spin glasses [156–159], this line of research will help our understanding of the intractable frustration mechanism.

In this chapter we discuss the “analog” quantum simulation for Ising-type magnets, in contrast with the “digital” version based on quantum gate operations. When the whole ion array is simultaneously illuminated by the same laser field in order to

create state-dependent forces, one or more collective motional modes are driven according to the internal state of each ion. For example, given that all ions are in the spin-up state and hence share a force along the same direction, they are all equally pushed so that the center-of-mass (CM) mode is excited. In general, as the motional modes are excited, relative (geometrical) phases are then developed between different ions. In a sense, the relative phase between any two spins accounts for the “coupling” between them, and the temporal behavior of the spins can be described by an effective Hamiltonian constituted by these “couplings”. In this work we discuss an effective Ising model, in which every two ions are coupled so that the overall system forms a complete graph, with each spin represented by a node and the coupling represented by an edge connecting two spins. By tuning the beatnote detuning frequency of the bichromatic field, various coupling patterns (sign and strength of edges) can be realized.

The structure of this chapter is outlined as follows. In Sec. 6.2 we derive the effective Ising-type Hamiltonian following procedures similar to those discussed in Chapter V. In Sec. 6.3 we explicitly calculate the coupling intensities for three-ion cases. In some parameter regions the network is frustrated. We map out the spin phases and show the “phase diagrams” as a transverse field is simulated and tuned up. To provide a comparison, in Sec. 6.4 we summarize the experimental results reported in [70]. Sec. 6.5 discusses larger Ising networks. As richer phases (spin orders) are observed, we find an interesting “transition”, i.e. the ground-state spin order change, due to competing interactions. We present a brief discussion on its scaling properties.

6.2 Formalism

We follow the same operation scheme as in Chapter V, by considering an ion chain illuminated by bichromatic laser beams with frequency detuning μ and a wavevector difference $\Delta\mathbf{k}$ along the operating mode direction, which is chosen to be the transverse (x) direction in our approach. This arrangement results in spin-dependent forces with frequency μ . The corresponding Hamiltonian is given by $H = \sum_n \hbar\Omega_n\sigma_n^z \cos(|\Delta\mathbf{k}|q_n + \mu t)$, where Ω_n is the Rabi frequency of the laser pulse on the n th ion; σ_n^z is the Pauli spin operator, and q_n is the transverse displacement in the x -direction of the n th ion. In the interaction picture we express $q_n = \sum_k b_n^k \sqrt{\hbar/(2M\omega_k)}(a_k^\dagger e^{i\omega_k t} + a_k e^{-i\omega_k t})$ in terms of the normal phonon modes a_k with mode frequency ω_k and the corresponding mode vectors \mathbf{b}^k . Under the rotating wave approximation and within the Lamb-Dicke limit $\eta_k \equiv |\Delta\mathbf{k}| \sqrt{\hbar/(2M\omega_k)} \ll 1$, the Hamiltonian becomes $H = -\hbar \sum_{n,k} \eta_k \Omega_n(t) b_n^k (a_k^\dagger e^{i\omega_k t} + a_k e^{-i\omega_k t}) \sigma_n^z \sin \mu t$, which leads to the evolution operator

$$U(\tau) = \exp \left[i \sum_{n,k} [\alpha_n^k(\tau) a_k^\dagger + \alpha_n^{k*}(\tau) a_k] \sigma_n^z + i \sum_{m,n} \phi_{mn}(\tau) \sigma_m^z \sigma_n^z \right]. \quad (6.1)$$

Here $\alpha_n^k(\tau) = \eta_k \Omega_n b_n^k \int_0^\tau e^{i\omega_k t} \sin \mu t dt$ characterizes the residual entanglement between the internal state of the n th ion and the collective phonon mode k ; $\phi_{mn}(\tau) = \Omega_m \Omega_n \int_0^\tau dt_2 \int_0^{t_2} dt_1 \sum_k \eta_k^2 b_m^k b_n^k \sin \mu t_2 \sin \mu t_1 \sin \omega_k(t_2 - t_1)$ represents the effective qubit-qubit interaction between ions m and n . In contrast to the pulse shaping in Chapter V, we do not require temporal variation in $\Omega_{m,n}$ and treat them as a constant pulse with a period τ . Therefore the above two integrals can be carried out and results

read

$$\alpha_n^k(\tau) = \frac{\eta_k b_n^k \Omega_n}{\mu^2 - \omega_k^2} [\mu - e^{i\omega_k \tau} (\mu \cos \mu \tau - i\omega_k \sin \mu \tau)], \quad (6.2)$$

$$\begin{aligned} \phi_{mn}(\tau) = \Omega_m \Omega_n \sum_k \frac{\eta_k^2 b_m^k b_n^k}{\mu^2 - \omega_k^2} & \left[\frac{\mu \sin(\mu - \omega_k)\tau}{\mu - \omega_k} - \frac{\mu \sin(\mu + \omega_k)\tau}{\mu + \omega_k} \right. \\ & \left. + \frac{\mu \sin 2\mu\tau}{2\omega_k} - \omega_k \tau \right]. \end{aligned} \quad (6.3)$$

As mentioned above, $\alpha_n^k(\tau)$ accounts for the unwanted entanglement of qubits and phonons during quantum simulation. We discuss the asymptotic behaviors in the “slow” regime, when the laser field is far detuned from each mode compared to the sideband Rabi frequency, i.e. $\eta_k \Omega_n / |\mu - \omega_k| \ll 1$. In this case the phonon contribution becomes negligible, and the evolution 6.1 can be factorized. As time increases, the first three terms in the square brackets of Eq. (6.3) are bounded and $\omega_k \tau$ becomes dominant. By comparing with the standard form $U(\tau) = e^{-iH_{\text{eff}}\tau/\hbar}$, we obtain an effective Ising Hamiltonian with

$$H_{\text{eff}} = \hbar \sum_{m,n} J_{mn} \sigma_m^z \sigma_n^z + \hbar \sum_{n,\xi} B_{n,\xi} \sigma_n^\xi \quad (6.4)$$

where

$$J_{mn} = \Omega_m \Omega_n \frac{\hbar}{2M} |\Delta \mathbf{k}|^2 \sum_k \frac{b_m^k b_n^k}{\mu^2 - \omega_k^2}. \quad (6.5)$$

Here we have included an effective term due to an external “magnetic field” in Hamiltonian (6.4): $\hbar \sum_{n,\xi} B_{n,\xi} \sigma_n^\xi$ ($\xi = x, y, z$), which can be simulated by applying single-qubit rotation laser beams. In this work, we only consider that all the ions share the same fields, i.e. $\Omega_m = \Omega_n = \Omega$ and $B_{n,\xi} = B_\xi$. (More complex configurations can be achieved by inclusion of multiple laser detunings and/or partial addressing.) Then the ground state for the simulated Hamiltonian only depends on two free parameters, the laser detuning μ and the ratio between the characteristic strength of coupling J_{rms} and B with $J_{rms} \equiv \sqrt{\frac{\sum_{m<n} |J_{mn}|^2}{N(N-1)/2}}$.

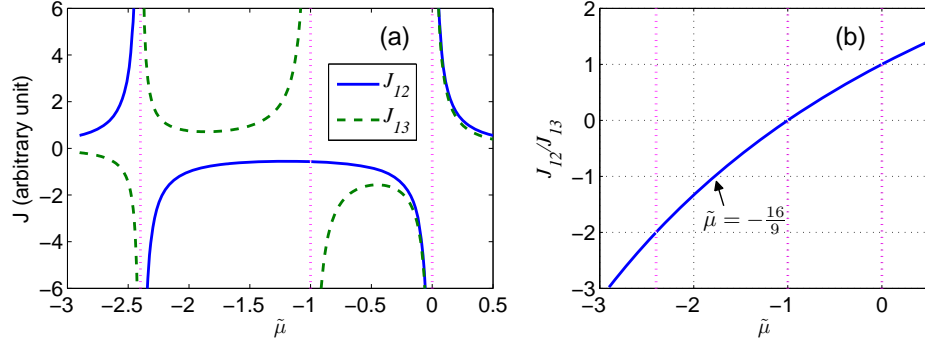


Figure 6.1: Coupling coefficients and ratio as a function of the normalized detuning $\tilde{\mu}$.

For $N = 2$, there is only one bond, whose coupling can be either positive (anti-ferromagnetic, AFM) or negative (ferromagnetic, FM). The sign changes when the detuning μ crosses the motional modes ω_k . Simulation with $N = 2$ was first demonstrated by A. Friedenauer *et al.* [63]. Coupling complexity of the Ising network increases when more and more ions are added. For $N = 3$, the network presents a simplest structure having competing interactions and shows frustration properties, which have been studied by K. Kim *et al.* very recently [70].

6.3 Three-ion Network

In this section we consider a three-ion string trapped in a harmonic trap $V(\mathbf{r}) = \frac{1}{2}m[\omega_x^2(x^2 + y^2) + \omega_z^2z^2]$. The three normal modes are represented by the mode vectors $\mathbf{b}_1 = \frac{1}{\sqrt{6}}[1, -2, 1]^\top$ (zigzag mode), $\mathbf{b}_2 = \frac{1}{\sqrt{2}}[1, 0, -1]^\top$ (tilt mode), $\mathbf{b}_3 = \frac{1}{\sqrt{3}}[1, 1, 1]^\top$ (center-of-mass, CM, mode) with the eigen-frequencies $\omega_1 = \sqrt{\omega_x^2 - \frac{12}{5}\omega_z^2}$, $\omega_2 = \sqrt{\omega_x^2 - \omega_z^2}$, $\omega_3 = \omega_x$, respectively. The three-ion Ising network is then characterized by the nearest-neighbor interaction $J_{12} = J_{23}$ and the next-nearest-neighbor one J_{13} . In Fig. 6.1(a), we plot the two couplings against the normalized dimensionless laser detuning $\tilde{\mu} \equiv \frac{\mu^2 - \omega_x^2}{\omega_z^2}$. Note that the couplings diverge when the detuning is on resonance with each mode ($\tilde{\mu} = -2.4, -1, 0$), and may change

Detuning	Coupling Type	Frustration	Spin configuration
$\tilde{\mu} < -2.4$	Short (AFM)		$ \downarrow\uparrow\downarrow\rangle, \uparrow\downarrow\uparrow\rangle$
$-2.4 < \tilde{\mu} < -\frac{16}{9}$	Short (AM)	\checkmark	$ \downarrow\downarrow\downarrow\rangle, \uparrow\uparrow\uparrow\rangle$
$-\frac{16}{9} < \tilde{\mu} < -1$	Long (AFM)	\checkmark	$ \downarrow\downarrow\uparrow\rangle, \uparrow\downarrow\downarrow\rangle, \uparrow\uparrow\downarrow\rangle, \downarrow\uparrow\uparrow\rangle$
$-1 < \tilde{\mu} < 0$	FM		$ \downarrow\downarrow\downarrow\rangle, \uparrow\uparrow\uparrow\rangle$
$\tilde{\mu} > 0$	AFM	\checkmark	$ \downarrow\uparrow\downarrow\rangle, \uparrow\downarrow\uparrow\rangle$

Table 6.1: Coupling pattern and the corresponding ground spin configurations for the three-ion network. The coupling pattern is classified into types: all bonds are ferromagnetic (FM), anti-ferromagnetic (AFM), and hybrid with the nearest-neighbor coupling stronger than the next-nearest-neighbor (Short), or the opposite (Long). FM or AFM in parentheses denotes the type of the stronger bond. Note that when approaching the CM mode ($\tilde{\mu} \rightarrow 0^\pm$), the two couplings are asymptotically identical and introduce extra degeneracy.

sign across the resonant points. The ratio $\frac{J_{12}}{J_{13}} = \frac{8(\tilde{\mu}+1)}{\tilde{\mu}+8}$, however, is a smooth function of $\tilde{\mu}$, as shown in Fig. 6.1(b), which plays a role as the only parameter controlling the ‘‘coupling pattern’’ of the network.

Note that the Hamiltonian (6.4) without an external field has a Z_2 symmetry so that the ground state is at least 2-fold degenerate and can be a superposition of all possible ground-state configurations. In Table 6.1, we show the coupling patterns and the associated ground spin configurations. Frustration occurs when not every bond can be satisfied energetically, and can usually lead to high degeneracy in general for a big network. In the three-ion case, frustration is observed in the blue-detuned region of the CM mode ($\tilde{\mu} > 0$), and emerges alternatively when $\tilde{\mu}$ is tuned down passing each mode. An unusual point is presented at $\tilde{\mu} = -\frac{16}{9} \sim -1.78$, where the ratio $J_{12}/J_{13} = -1$, indicating a balance of competition of the two interactions. This special point remains in a larger odd-number network. We will discuss some interesting properties in Sec. 6.5.

When a transverse external field $\mathbf{B} = B\hat{x}$ is turned up, the spins start to rotate tending to align with the field. We plot the probability of having FM order $P_{FM} = P_{\uparrow\uparrow\uparrow} + P_{\downarrow\downarrow\downarrow}$ for a ground state of Hamiltonian (6.4) in Fig. 6.2. Note that in a long-range Ising model, a second-order phase transition into a paramagnetic state can

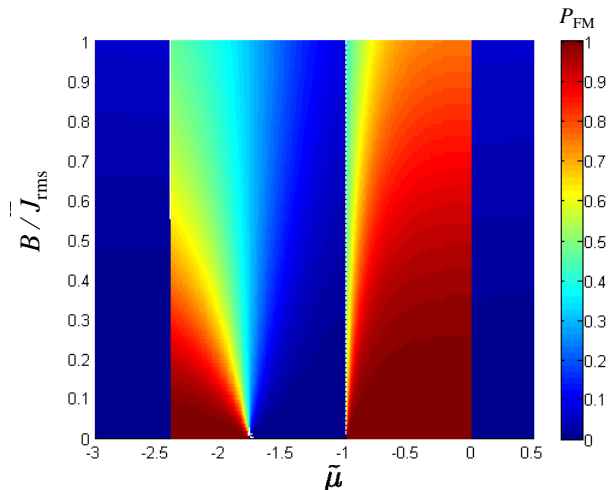


Figure 6.2: Phase diagram showing the projection (probability) of the ground state to the FM order component. ($J_{rms} \equiv \sqrt{(2J_{12}^2 + J_{13})/3}$)

be observed in the thermodynamic limit. However in a small system, as expected, the “transition” is still quite smooth. Another noticeable transition takes place at $\tilde{\mu} \sim 1.78$ as mentioned above. At $B = 0$, the transition is due to a strict level crossing but the crossing is avoided at $B \neq 0$. The scaling properties of the energy gap or other relevant orders are interesting problems for quantum phase transitions, which will be discussed in Sec. 6.5.

Generally speaking, although frustration does not necessarily lead to high degeneracy (e.g. $-2.4 < \tilde{\mu} < -1.78$ in our three-spin case), they have close connections because of the competing interactions. A ground manifold of a frustrated Hamiltonian with no external field can be spanned by various competing configurations, which can be a set of product states. As a transverse field is turned on and hence introduces noncommuting contributions, different manifolds can be mixed. Once the field is gradually removed (staying adiabatic) without breaking the symmetry of the original Hamiltonian, it normally ends up with entangled states. In the experimental demonstration [70], we start with the ground state $|+++ \rangle$ with $|+\rangle \equiv \frac{1}{2}(|\uparrow\rangle + |\downarrow\rangle)$

in the strong field limit $H \sim \sum_i B\sigma_i^x$. Next, the Ising Hamiltonian comes in with B kept strong, and then we ramp B down to zero through a specific path. As mentioned earlier, the Ising Hamiltonian has a Z_2 symmetry so that the resultant state should involve superposition of two Z_2 -symmetric states, given that the adiabatic path is perfectly unbiased. However, macroscopically such entanglement is always lost and collapses to a classical (product) state with a biased order, the so-called spontaneous symmetry breaking. We can mimic this effect by applying an additional symmetry breaking field B_z along z -direction, which, however, must be kept sufficiently small so as not to interfere with the frustrated mechanism. To be more precise, since $B_z\sigma_i^z$ commutes with the no-field Hamiltonian (6.4), B_z can be made small to stay in the same frustrated ground manifold of the specific polarization direction, but needs to be large enough to lift (separate) the non-favored polarization manifold.

The adiabatic path is designed as follows. We initialize the state in $|+++ \rangle$ and turn on the system at $B \gg J_{rms}$. We then linearly tune up the symmetry breaking field from 0 to B_z . Keeping B_z unchanged, ramp B down exponentially to nearly 0. In Fig. 6.3, we show the time-evolution curves as B is turned down exponentially. We calculate the fidelity of the final state $|\psi_f\rangle$ with $F_{FM} = |\langle \uparrow\uparrow\uparrow | \psi_f \rangle|^2$, $F_W = |\langle \psi_W | \psi_f \rangle|^2$ with $|\psi_W\rangle = \frac{1}{\sqrt{3}}(|\uparrow\uparrow\downarrow\rangle + |\uparrow\downarrow\uparrow\rangle + |\downarrow\uparrow\uparrow\rangle)$, and $F_{\psi^+} = |\langle \psi^+ | \psi_f \rangle|^2$ with $|\psi^+\rangle = \frac{1}{\sqrt{2}}(|\uparrow\uparrow\downarrow\rangle + |\downarrow\uparrow\uparrow\rangle)$. In Fig. 6.3(a), we deal with a uniform AFM three-ion network whose ground state should be a superposition of two W-type states and hence has 6-fold degeneracy. This situation is highly frustrated because every bond has equal probability of not being satisfied energetically. Through the time evolution, the Z_2 symmetry is broken and a polarized W-state is obtained with a very high fidelity. However, this uniform AFM network cannot be realized perfectly in experiments because $J_{12} = J_{13} > 0$ only occurs on resonance with the CM mode.

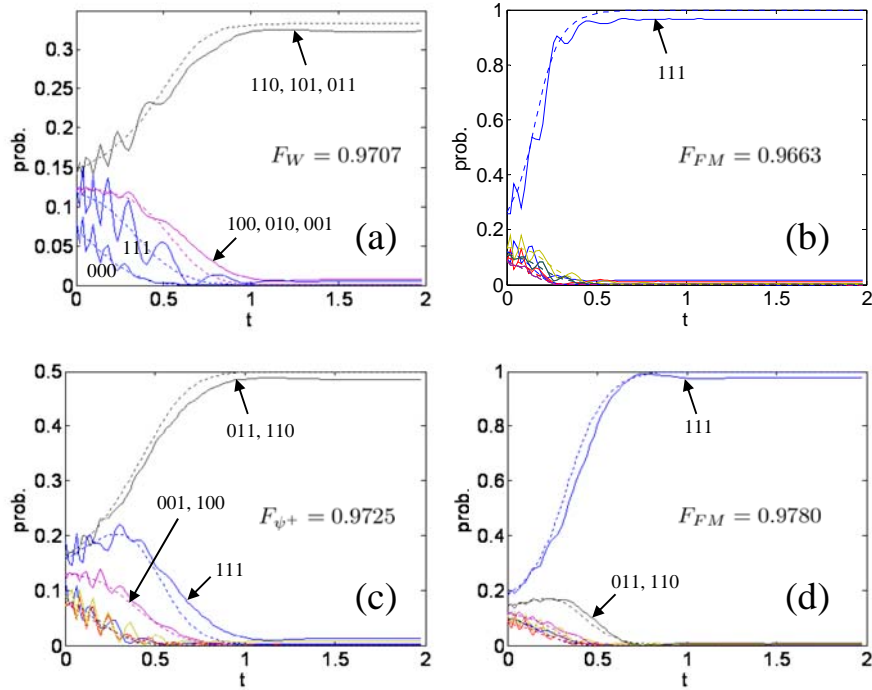


Figure 6.3: Time evolution of the probability of each component for (a) $J_{12} = J_{13} = 1\text{kHz}$, (b) $J_{12} = -1\text{kHz}$, $J_{13} = -2\text{kHz}$, (c) $J_{12} = -1\text{kHz}$, $J_{13} = 2\text{kHz}$, (d) $J_{12} = -1\text{kHz}$, $J_{13} = 0.8\text{kHz}$. The components with significant probabilities are pointed out by binary numbers where $1 \rightarrow |\uparrow\rangle$ and $0 \rightarrow |\downarrow\rangle$. About the evolution path, first keep $B = B_0 = 10\text{kHz}$ (x direction) and increase B_z (z direction) from 0 to 1kHz within $T_1 = 0.1\text{ms}$; then keep $B_z = 1\text{kHz}$ and follow $B(t) = B_0 \exp(-t/T_2)$ with $T_2 = 0.2\text{ms}$. Only the evolution curves for the final step are shown here.

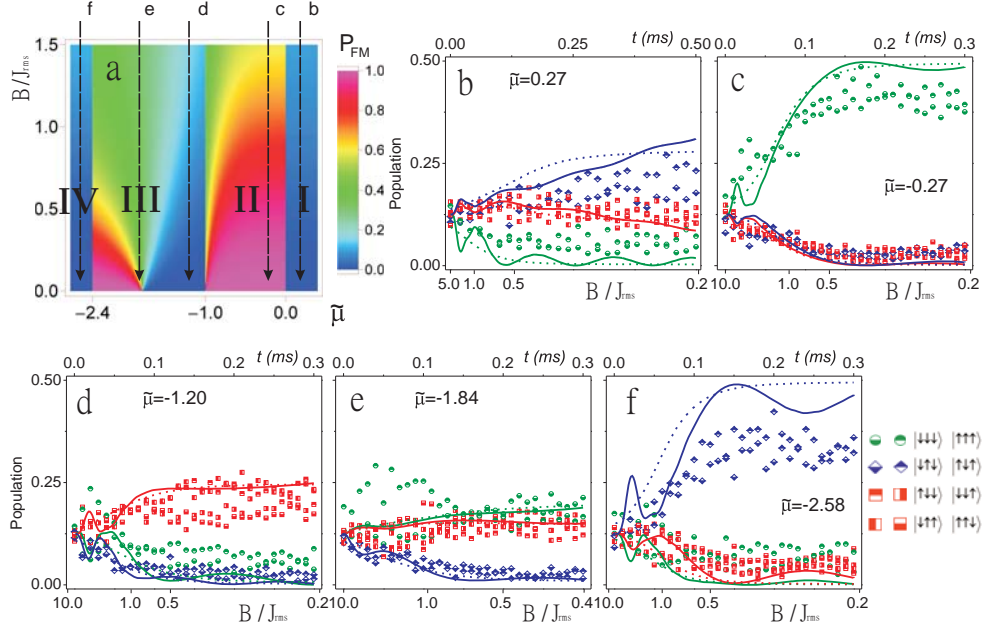


Figure 6.4: (a) The theoretical phase diagram (same as Fig. 6.2). Indicated by the vertical arrows are the evolution paths for case (b) to case (f). (b–f) The time evolution curves for each basis component. The scattered points correspond to the experimental data; the dashed curves correspond to the instantaneous (absolutely adiabatic) ground states, and the solid curves correspond to theoretical finite-speed evolution. (Figure from [70].)

The resultant state will deviate from the W-state very fast when $\tilde{\mu}$ is away from 0. Despite that, the final state remains W-type entangled (through entanglement witness measurement, see Sec. 6.4) even when F_W is far below unity. Another “frustration-assisted” entangled state is shown in Fig. 6.3(c); we find it belongs to the two-qubit entanglement class because it is a direct product of a single qubit and a two-qubit Bell state.

6.4 Experimental Comparison

In this section we summarize the experimental results of [70]. The Ising network is realized on a linear chain of three $^{171}\text{Yb}^+$ ions within a three-layer Paul trap [64]. The Ising spin is represented by two-level hyperfine states $^2S_{1/2}|F=1, m_F=0\rangle$ and $^2S_{1/2}|F=0, m_F=0\rangle$ (separated by $2\pi \times 12.6\text{GHz}$) for each ion. In the current experimental setup, the trapping frequencies are chosen as $\omega_z = 2\pi \times 1.49\text{MHz}$ and

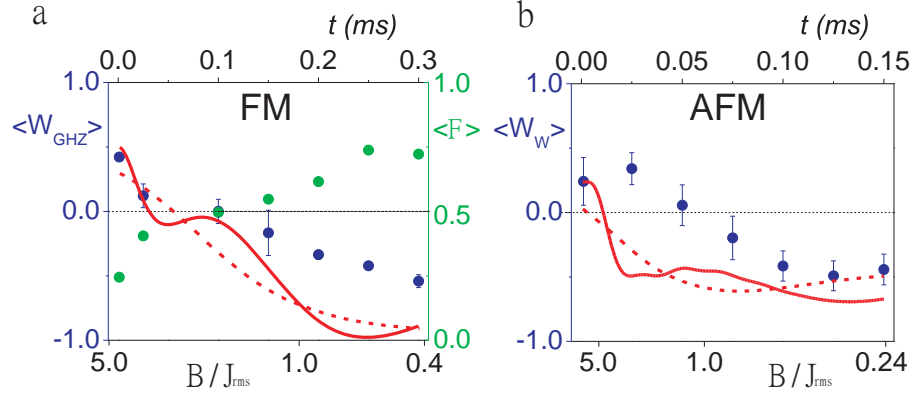


Figure 6.5: Entanglement witness measurements as $|B|/J$ is ramped down for (a) FM and (b) AFM regions (see Fig. 6.4). A negative value indicates entanglement. Here, $|J_{13}/J_{12}| \sim 0.85$. The blue dots correspond to the experimental data for (a) the GHZ witness and (b) the W-type witness. The dashed curves correspond to the absolutely adiabatic evolution and the solid curves correspond to the theoretical finite-speed ramping. For (a), the experimental data for the GHZ fidelity F_{FM} (see Sec. 6.3) is plotted in green dots. ($F > 0.5$ indicates entanglement.) (Figure from [70].)

$\omega_x = 2\pi \times 4.33\text{MHz}$. To check the validity of the quantum simulation of Hamiltonian (6.4), we probe the population of each component for a time-evolving state instantaneously. In Fig. 6.4 (b–f) we show the experimental curves corresponding to the evolution paths indicated by Fig. 6.4(a) at different laser detuning $\tilde{\mu}$. Figs. 6.4(b), (d) and (e) correspond to the frustration parameter regions. In Fig. 6.4(b) where the coupling is AFM-type with $J_2 \sim 0.8J_1$, in the end of the evolution six components out of the total eight, excluding the two FM-type components, are picked up, signaling the emergence of the W-type state. (The difference in population in these six components mainly comes from $J_1 \neq J_2$.) By contrast, Fig. 6.4(c) shows the FM case; only the FM-type components emerge. In Figs. 6.4(d) and (e), the experimental curves reveal that the ground state has multiple degeneracy (due to frustration) and the population roughly lies in these degenerate components equally. In Figs. 6.4(f) where the network becomes non-frustrated. The dominance of a specific spin order is obvious.

As the AFM-type coupling has been realized in the ground state manifold (as

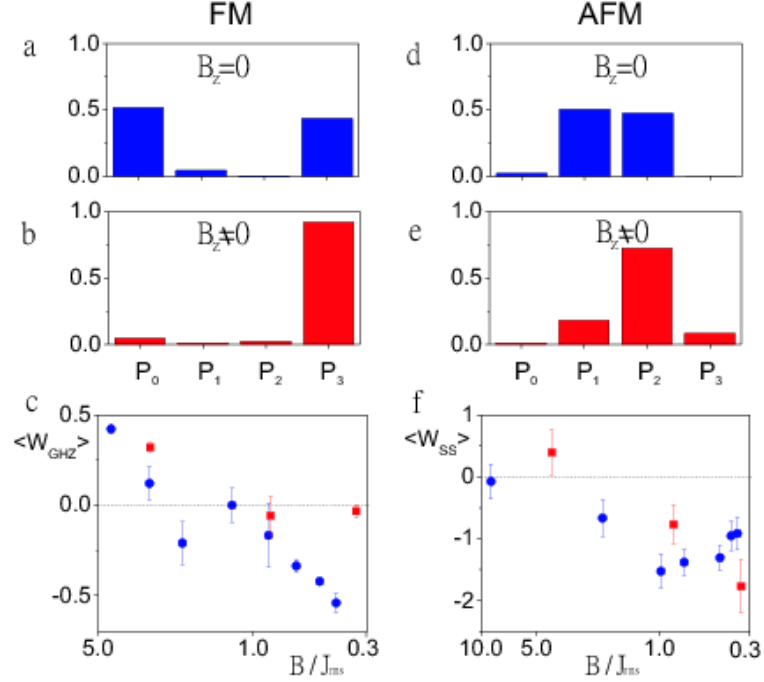


Figure 6.6: The effect of a symmetry breaking field B_z in the FM region (a-c) and AFM region (d-f). Panel (a), (b) and (d), (e) show the population in different components of the resultant state, without and with a symmetry breaking field, respectively. The probabilities P_0, P_1, P_2, P_3 corresponding the projection of the state to the σ^z eigen-component(s) of 0, 1, 2, 3 \uparrow 's (number of up-spins). Panel (c) and (d) show the instantaneous entanglement witness during the ramp. The blue (red) dots correspond to no-field (finite-field) cases. (Figure from [70].)

in Figs. 6.4(b)), the same-magnitude FM-type coupling can be also implemented effectively, by following the highest excited manifold (and reversing the sign of the transverse field as well). A comparison between these two cases is shown in Fig. 6.5, where the entanglement of the GHZ- and W-type is detected under the FM and AFM situations, respectively. The entanglement witness for the GHZ-type is given by $W_{GHZ} = 9/4 - \hat{\mathcal{J}}_z^2 - \prod_i \sigma_i^x$, where $\hat{\mathcal{J}}_z \equiv \frac{1}{2} \sum_i \sigma_i^z$, and for the W-type $W_W = 4 + \sqrt{5} - 2(\hat{\mathcal{J}}_x^2 + \hat{\mathcal{J}}_y^2)$ [131, 160]. The experimental data and the theoretical curves agree qualitatively.

To show the effects of the symmetry breaking field B_z discussed in Sec. 6.3, we add this field during the time evolution to study the above FM and AFM cases. To keep adiabaticity, the field is turned on and then linearly increased to a finite value

of B_z while the transverse field B is ramped down. We measure the probability of each number of up-spins for the final state, and detect the entanglement change with the ramp as shown in Fig. 6.6. For the FM case, we can see the ground state switches from the GHZ-type (equal probability in P_0 and P_3) to a product state (P_3 only) when B_z is introduced. It is confirmed by looking at the entanglement witness, which indicates that the entanglement is lost with time by inclusion of B_z . By contrast, in the AFM case the final state (with no symmetry breaking field) should be approaching to a superposition of two W-states, and become closer to a single W-state (P_2 dominates). In this situation, the bipartite spin-squeezing witness operator $W_{SS} \equiv (\hat{\mathcal{J}}_z^2 + \frac{3}{4})^2 - 4\langle \hat{\mathcal{J}}_z \rangle^2 - (\hat{\mathcal{J}}_x^2 + \hat{\mathcal{J}}_y^2 - \frac{3}{2})^2$ is taken instead of W_W because the W_{SS} -measurement is less sensitive to errors [160]. It also shows that the entanglement remains in the presence of B_z , in agreement with the discussion in Sec. 6.3.

6.5 Multiple-ion Network

As more ions are added to the Ising network, the number of edges (couplings) grows as fast as $N(N-1)/2 \sim O(N^2)$, and the dimension of the Hilbert space grows even faster, as 2^N . However, the strength and sign on each edge are uniquely determined by the laser frequency detuning μ if the same bichromatic laser field is applied. This means the controllability to achieve arbitrary coupling is somewhat limited. Nevertheless, the multiple-ion networks show a rich zoo of phases. In Table 6.2, we list all ground-state spin orders for odd numbers of ions less than 10. For convenience of discussion, we rescale the laser detuning by labeling the motional modes (from lowest to highest modes) by integers (from 1 to N) and using a linear scaling (between two integers) for detunings located between two modes. (For example, $\mu = \omega_2 + \frac{3}{4}(\omega_3 - \omega_2) \rightarrow \mu' = 2.75$.) For even numbers of ions, the variation of

$N = 3$		$N = 5$		$N = 7$		$N = 9$	
Spin order	Trans. Pt.	Spin order	Trans. Pt.	Spin order	Trans. Pt.	Spin order	Trans. Pt.
010	- Mode 1 1.45	01010	- Mode 1 1.07	0101010	- Mode 1 1.007	010101010	- Mode 1 1.0005
000		00000		0000000		000000000	
001		00001		0000001		000000001	
000	- Mode 2	00110	1.18	0111110	1.023	011111110	1.0015
010	- Mode 3	01001	1.23	0100110	1.041	010011010	1.0033
		01110	- Mode 2	0100101	1.205	010100101	1.1703
		00000	- Mode 3	0100010	- Mode 2	010111010	- Mode 2
		00011	3.26	0000000	- Mode 3	000000000	- Mode 3
		00000	- Mode 4	0001110	3.001	000011100	3.0074
		01010	- Mode 5	0110001	3.113	001100010	3.0363
				0111110	- Mode 4	010001101	3.1061
				0000000	- Mode 5	011000110	- Mode 4
				0000111	5.183	000000000	- Mode 5
				0000000	- Mode 6	010100001	5.0006
				0101010	- Mode 7	011010001	5.0049
						000011110	5.0215
						011100001	5.0488
						001111100	- Mode 6
						000000000	- Mode 7
						000001111	7.1386
						000000000	- Mode 8
						010101010	- Mode 9

Table 6.2: Ground spin configurations for odd numbers of ions. For the spin order indicated in binary numbers, only one specific component is shown. The real ground states should be superpositions of all possible configurations that can be transformed from this specific component by Z_2 transformation and reflection with respect to the middle ion. Among rows, the thick borders between different spin configurations indicate the separation due to motional modes; the dashed borders indicate the change of spin order due to competing interactions, with similar coupling patterns, between modes. The number beside a dashed border shows the corresponding (rescaled) detuning μ' (see text).

spin orders is relatively less rich than in odd-number cases due to perfect reflection symmetry of the left and right parts of the ion chain, and hence is not discussed here.

An interesting feature can be observed between the second- and third-highest modes for odd-number cases, namely the change of the spin order from FM to a kink order, i.e., two different FM orders on two sides of the ion chain. The change to a kink order occurs in the three-ion case when the Short-FM couplings compete with the Long-AFM type (see Table 6.2 and Fig. 6.2). When a transverse field is turned on, the two configurations are mixed and gradually aligned to the field direction. In Fig. 6.7 we plot the “order parameter” $P_{FM} - P_K$ at different (rescaled) detunings and fields. Along the x -axis where B/J_{rms} is negligibly small, the abrupt change of the spin order indicates a strict level-crossing. The phase boundary is blurred by increasing B . But as more ions are added, the interface becomes sharper and sharper, signaling the closing of the energy gap between the ground state and the excited states (see Fig. 6.8). By fitting the energy gap with increasing N , we obtain $\Delta E \propto \left(\frac{B}{NJ_{rms}}\right)^{\frac{N-1}{2}}$ for small B , which is a signature for a first-order quantum phase transition. This transition boundary develops extremely fast as N grows into a distinct interface even for a small system (for $N = 13$), in contrast to the conventional phase transitions, which usually show only crossover behaviors for such small systems. Interestingly, the FM-order region in Fig. 6.7 shrinks too as N grows. The width of the rescaled detuning along $B = 0$, measuring the distance from the strict level-crossing point (the endpoint of the interface on the μ' -axis) to the motional mode on the left-hand side, can be fitted by the relation $\Delta\mu' \sim 1.45N^{-1.07}$. This special phase transition thus cannot be discussed in the thermodynamic limit in our simple simulation model.

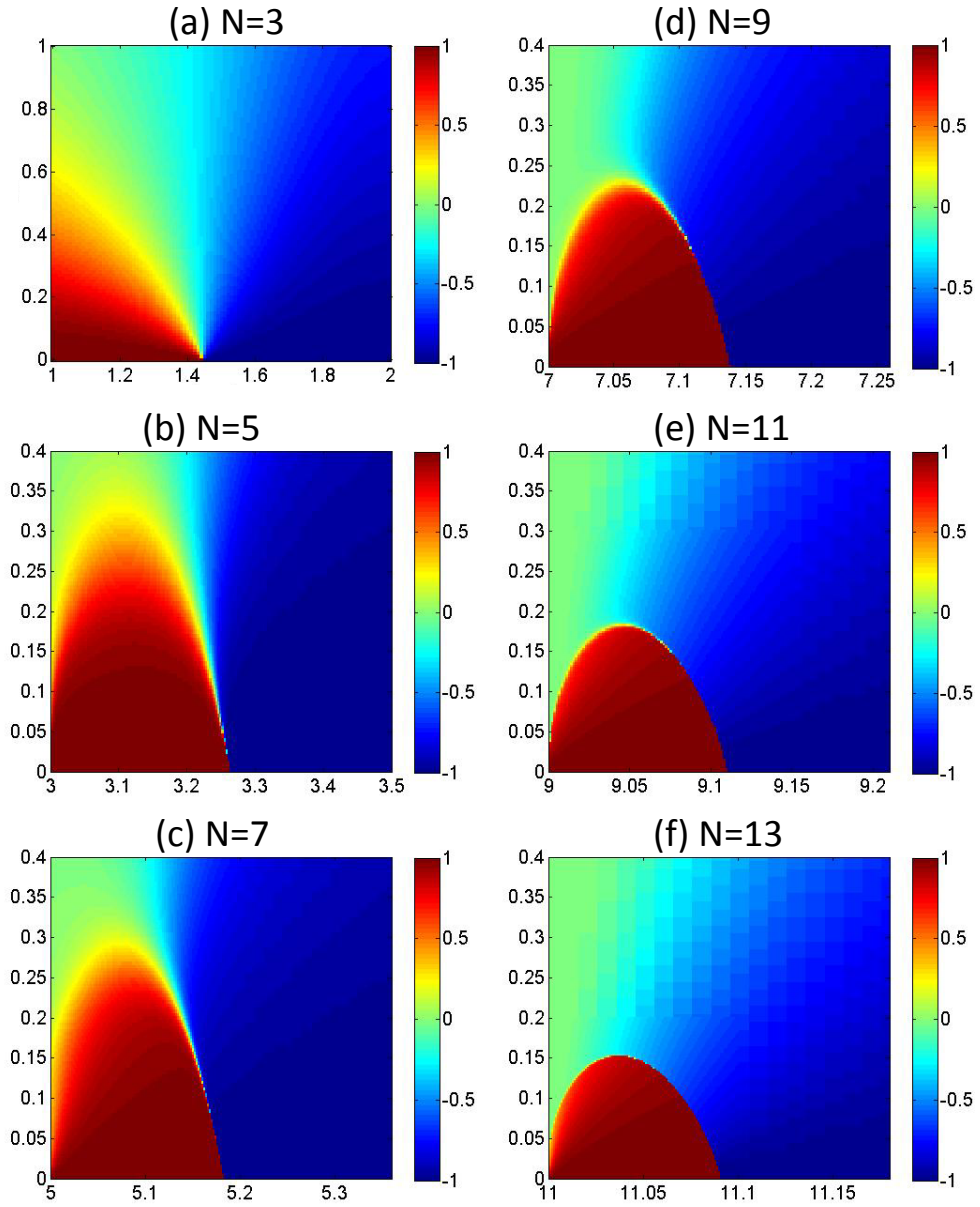


Figure 6.7: Phase diagrams of odd numbers of ions. (x-axis: the rescaled detuning μ' ; y-axis: B/J_{rms} ; color-axis: $P_{FM} - P_K$ with P_{FM} and P_K are the projection (probability) of the ground state to the FM- and kink-order components, respectively.)

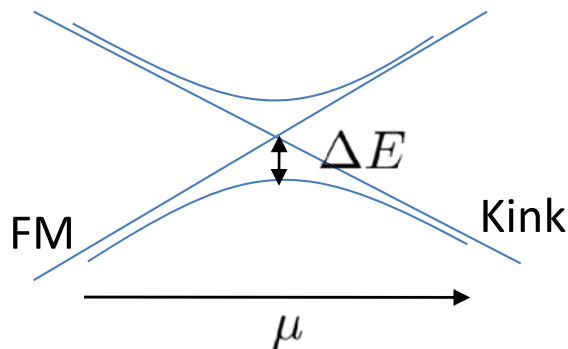


Figure 6.8: Level crossing at the FM-Kink transition. Two FM ground states intersect with two Kink ground states with an energy gap raised by the transverse field.

6.6 Chapter Summary

In this chapter we have explicitly demonstrated the quantum simulation of Ising-type magnets in a trapped ion system. Through controlling the laser beatnote detuning frequency, various coupling patterns can be realized on the Ising networks. We have given a detailed discussion on frustration of the three-ion network. We have presented a “phase diagram” of the spin order as the detuning and the external field change. For comparison with the experimental data, we perform the nearly-adiabatic time evolution calculation. When the coupling changes, the no-field ground states are in general superpositions of different product states and hence entangled. To distinguish different types of entanglement (e.g. GHZ- or W-type) in different coupling regions, we add a symmetry breaking field during the evolution. Our theoretical results are confirmed by experimental observation [70].

For large networks, richer spin phases can be found. Certain spin orders pre-existent in the small networks are also observed in a larger system. This allows us to investigate scaling properties of such orders. Frustration leads to an interesting transition that takes place in the case of odd numbers of ions: the change in the spin order from the ferromagnetic to a kink state. The phase boundary develops into a

first-order transition very fast as N grows, even for a small system ($N \leq 13$).

CHAPTER VII

Conclusions

7.1 Summary

In this thesis we have investigated several interesting problems in the field of ultracold atomic systems, and discussed potential applications by engineering these systems to study fundamental quantum many-body problems. For an ultracold Fermi gas, our study reconstructs the conventional superfluidity and superconductivity that have been studied in different scenarios such as helium-3 or -4 and superconductors, and may help in understanding high- T_c superconductivity [16–18], quantum Hall effects [19, 20], and quark matter [161, 162]. By introducing optical lattices, we are able to simulate general lattice problems. Trapped ions are employed for universal digital quantum simulation, in which each step is performed by a one- or two-qubit operation. Another application is to simulate the Ising or Heisenberg model in an “analog” way. This allows us to directly study the quantum phase transitions and frustrated physics.

We have discussed 3D and quasi-2D Fermi gases in the context of the BEC-BCS crossover, and demonstrated the mean-field calculation at zero-temperature. For 3D cases, Bose-condensation and superfluidity have been extensively investigated, and attention in the field has turned to spin imbalanced Fermi gases or more complicated

cases. In particular, motivated by recent advances in observation of the Feshbach resonances between different species of atoms like boson-fermion [79, 80] and fermion-fermion mixtures [81–84], we have studied the mass effects in the ultracold fermion-fermion mixture, focusing on conventional BCS pairing and superfluidity, as well as the BEC-BCS crossover behavior. The Cooper pairing of two spins strongly relies on the closeness of the two Fermi surfaces. The energy characterized by the gap Δ associated with the formation of pairs has to compete with the differential chemical potential \hbar . Under the local density approximation (LDA), the Fermi surfaces are profiled in quadratic curves in a harmonic trap. In an equal-mass scenario, the trap center has a higher number density so that the superfluid core usually emerges. The mass mismatch introduces different curvatures of the two Fermi surfaces $k_F^\sigma(\tilde{r}) = \sqrt{2m_\sigma(\mu_\sigma - \tilde{r}^2)}$. When the heavy species is in excess, the two Fermi surfaces might have a large discrepancy at the trap center (so that Cooper pairing is suppressed) but become comparable near the trap edge (so that a superfluid phase tends to appear), leading to a superfluid shell enclosing a normal-state core. This feature of forming a superfluid shell is not notable in the equal-mass case. We anticipate that the properties of such superfluid shells may be interesting because of the nontrivial topology.

A quasi-2D Fermi gas can be prepared in a deep one-dimensional optical lattice (strong plain standing waves) where the inter-layer tunneling is shut off. It seems intuitively valid that in the strong confinement limit, the higher-band excitations (with respect to the strong trap) would be suppressed. From this assumption we have derived a single-channel model with renormalized atomic interaction across the Feshbach resonance [106, 108, 109]. We have shown that the detail for the renormalized interaction is not important, and the single-channel model leads to the

result that the in-trap density profiles of the gas are invariant. The single-channel model also predicts a constant cloud size over the entire BEC-BCS crossover scope. This result is counter-intuitive and violates the bosonic nature when the gas is tuned to the BEC side. Previous work [110, 112] has suggested a two-channel point of view, where the closed (Feshbach molecule) channel is included and the couplings of atom-atom, atom-molecule, molecule-molecule are “dressed” by higher-band excitations that we originally neglected in the single-channel model. Therefore, to be precise the closed channel corresponds to including effective “dressed molecules” by summing all the contributions from higher bands. From this two-channel model, we have calculated relevant properties and observed a shrinking cloud size when the gas is tuned from the BCS side to the BEC side. This result confirms the suggestion of [110, 112] that the higher-band excitations even in the strong trap limit cannot be neglected. Further, this two-channel model provides a quantitative description of the cloud size; its validity can be verified by future experiments.

As a considerable amount of work has focused on the quantum (superfluid to Mott insulator) and thermal phase transitions in an optical lattice, we discuss the signature for identifying superfluidity in such systems. At present, the time-of-flight spectroscopy is commonly used for this purpose [47, 48]. Because the condensed particles are strongly correlated and show distinct interference peaks, we explicitly calculate the momentum density distribution and the interference profiles by taking into consideration the atomic interaction strength and the global (but weak) trap. We claim that the interference profiles can reveal a wealth of information. First, a bimodal distribution, i.e. a sharp peak on top of relatively flat thermal tails, is a robust feature as long as a condensate is present. Other quantities such as the visibility and the peak width can be read out, signaling the onset of superfluidity

under some circumstances. Most notably, below the critical temperature where the thermal tail itself is not reliable in determining the temperature, the condensate fraction can be extracted by fitting the bimodal distributions, and serves as a good supplementary thermometer.

Regarding trapped ion quantum computation, as so many proposals have been successfully realized with a small number (< 15) of ions (qubits), it seems that a next milestone is a direct demonstration of quantum power, i.e., the ability to handle problems that are intractable by classical means. Scaling of the system is an obstacle to be overcome, owing to the increasing technical challenges as more ions are added to a one-dimensional array. We propose a large-scale architecture by stabilizing a uniform ion crystal within an anharmonic potential. We demonstrate realization of high-fidelity transverse quantum gates for which the temperature requirement can be reached by simply Doppler cooling. The gate design is through a systematic shaping of the laser pulse, making the gate operation arbitrarily fast. We find that the two-qubit operation involves only neighboring ions, with irrelevant ions “frozen” in space. This implies that the gate implementation does not have scaling difficulties. Further, concurrent multiple gate operations at different locations do not interfere with each other, so that parallel computing is possible.

Finally we have discussed the Ising magnet simulation based on trapped ion systems [62–65]. The effective Hamiltonian can be realized by illuminating all the ions with the same laser field. Various coupling patterns can be implemented by choosing the laser beatnote detuning across motional modes, yielding an Ising magnet network. We have explicitly investigated the three-ion case, which is the simplest network that shows frustrated behaviors. In a recent experimental work [70], the validity of such simulation (for three ions) has been confirmed. We have discussed

the close connection of frustration due to competing interactions and entanglement in highly degenerate systems. When this simulation applies to larger Ising networks, much richer phases can be found. In general, the study of the scaling properties helps us understand how a quantum phase transition develops towards the thermodynamic limit. We discuss a particular example observed for only odd numbers of ions, where the spin order changes suddenly with the laser detuning. This “transition” is due to the competing interactions, and already shows clear evidence of a first-order phase transition even for a small system (≤ 13).

In conclusion, successful quantum simulation relies on several important aspects: first, the similarity of two “inter-simulatable” physical systems [1]; second, the arbitrariness (controllability) of the physical simulator; third, good isolation from noisy environments; and finally, the initial preparation to encode information and faithful measurement to retrieve information. In this thesis, although our discussion focuses mainly on the first two aspects, we have demonstrated that ultracold atomic systems are “inter-simulatable” with a wide range of many-body problems, and have an exceptional controllability through optical and magnetic manipulation.

7.2 Future Directions

As the BEC-BCS crossover for a spin polarized Fermi gas has become accessible in current experiments, recent attention has focused on unequal-mass mixtures. Although we anticipate that our mean-field calculation should provide at least a qualitatively correct picture, other work suggests unusual properties beyond the mean-field point of view. For example, in the BCS regime, correlations beyond the mean field introduce a nontrivial mass dependence on the superfluid gap [163]. In the BEC regime, several studies reveal that the mass ratio plays a crucial role in the dimer-

dimer interaction [164, 165]. To further study these nontrivial properties, inclusion of higher order fluctuations will be necessary. One direction of interest which has been raised quite recently is the trap asymmetry between two species [166–168]. At the mean-field level, our approach should easily generalize to include this factor. Another important topic concerns the p -wave superfluid phases with s -wave short-range interactions in a spin polarized (equal-mass) Fermi gas [169].

For trapped ion quantum computing, in addition to the quantum gate implementation presented in this thesis, there have been considerable efforts and achievements in realizing certain interesting many-body states [131–133]. These states have great significance for, e.g., measurement-based quantum computation [170]. However, so far experimental demonstration exists only for small numbers of ions and for certain simple entangled states such as GHZ states. We hope to generalize our proposed method by laser pulse shaping and look for a systematic way to implement complex many-body entangled states such as cluster states. Regarding quantum simulation, the Ising coupling patterns in our proposed model are controlled through a single parameter, the laser detuning, and therefore the arbitrariness is restricted. As more complicated laser fields are engineered, one can expect that the controllability of interactions can be increased. It has been reported that a certain Ising-coupled network has a close connection to the NP-complete problem [171]. The engineering of such interactions will be an important step toward addressing NP-hard problems.

APPENDICES

APPENDIX A

Segmental Pulse Shaping

In this appendix we explicitly show the procedures for designing a two-qubit gate by the segmental-pulse shaping scheme. As discussed in Chapter V, the computational infidelity of the controlled-phase (CP) gate from the residual motional entanglement is given by [61]

$$\delta F = [6 - 2(\Gamma_i + \Gamma_j) - \Gamma_+ - \Gamma_-]/8, \quad (\text{A.1})$$

where

$$\begin{aligned} \Gamma_{i(j)} &= \exp[-\sum_k |\alpha_{i(j)}^k(\tau)|^2 \bar{\beta}_k/2], \\ \Gamma_{\pm} &= \exp[-\sum_k |\alpha_i^k(\tau) \pm \alpha_j^k(\tau)|^2 \bar{\beta}_k/2], \end{aligned} \quad (\text{A.2})$$

with $\bar{\beta}_k = \coth \frac{\hbar\omega_k}{k_B T_k}$ and $\alpha_i^k(\tau) = \eta_k b_i^k \int_0^\tau dt \Omega(t) e^{i\omega_k t} \sin \mu t$ (τ is the gate time). Our purpose is to chop $\Omega(t)$ into M equal segments, i.e. $\Omega_n(t) = \Omega_m = \text{constant}$ when $t \in [\tau_{m-1}, \tau_m)$ for $m = 1, 2, \dots, M$ and $\tau_m \equiv m\tau/M$, and minimize δF over a real vector $X \equiv (\Omega_1, \Omega_2, \dots, \Omega_M)^\top$. This can be done fully numerically; however, it can be greatly simplified by a quadratic minimization method. To see this, we need an asymptotic expression for δF when it is nearly unity, which corresponds to $\alpha_{i(k)}^k$ being small, so that one can expand $e^x = 1 - x + O(x^2)$ in those Γ 's with x containing $\alpha_{i(j)}^k$'s to the second order. The infidelity then reads

$$\delta F \simeq \frac{1}{8} \sum_k \bar{\beta}_k [|\alpha_i^k|^2 + |\alpha_j^k|^2 + |\alpha_i^k(\tau) + \alpha_j^k(\tau)|^2/2 + |\alpha_i^k(\tau) - \alpha_j^k(\tau)|^2/2]. \quad (\text{A.3})$$

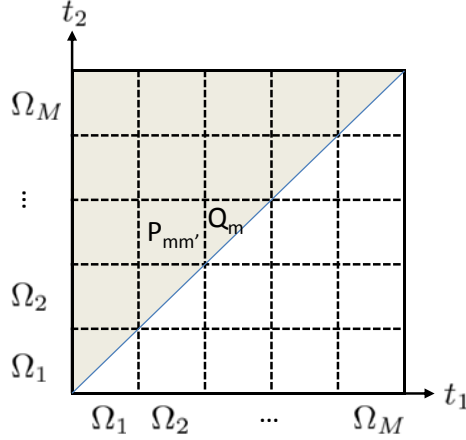


Figure A.1: Integration area for $\phi_{ij}(\tau)$. Each piece has a contribution weighted by the corresponding $\Omega_m \Omega_{m'}$.

Define $G_{im}^k = \eta_k b_i^k \int_{\tau_{m-1}}^{\tau_m} e^{i\omega_k t} \sin \mu t dt$, constructing a vector $G_i^k \equiv (G_{i1}^k, G_{i2}^k, \dots, G_{iM}^k)^\top$.

It can then be written that $\alpha_i^k = G_i^k X$ and $\sum_k \bar{\beta}_k |\alpha_i^k|^2 = X^\top A^i X$, where the matrix A is defined as $A_{mm'}^i = \sum_k \bar{\beta}_k G_{im}^k G_{im'}^{k*}$. Similarly, $\sum_k \bar{\beta}_k |\alpha_i^k \pm \alpha_i^k|^2 / 2 = X^\top A^\pm X$ with $A_{mm'}^\pm = \sum_k \bar{\beta}_k (G_{im}^k \pm G_{im}^{k*})(G_{im'}^{k*} \pm G_{im'}^k)$. Note that $A^{i(j)}$ and A^\pm can be evaluated numerically in no time because G_{im}^k has an analytical form (omitted here).

Then we have $\delta F = X^\top A X$ with $A = (A^i + A^j + A^+ + A^-) / 8$.

Note that the above minimization must be performed under the constraint $\phi_{ij} = \pi/4$, where

$$\phi_{ij}(\tau) = 2 \int_0^\tau dt_2 \Omega(t_2) \int_0^{t_2} dt_1 \Omega(t_1) \sum_k \eta_k^2 b_i^k b_j^k \sin \mu t_2 \sin \mu t_1 \sin \omega_k(t_2 - t_1).$$

This integration is performed over the shaded area in Fig. A.1. Define the partitioned parts of the integration

$$P_{mm'} \equiv 2 \int_{\tau_{m-1}}^{\tau_m} dt_2 \int_{\tau_{m'-1}}^{\tau_{m'}} dt_1 \sum_k \eta_k^2 b_i^k b_j^k \sin \mu t_2 \sin \mu t_1 \sin \omega_k(t_2 - t_1)$$

and

$$Q_m \equiv 2 \int_{\tau_{m-1}}^{\tau_m} dt_2 \int_{\tau_{m-1}}^{t_1} dt_1 \sum_k \eta_k^2 b_i^k b_j^k \sin \mu t_2 \sin \mu t_1 \sin \omega_k(t_2 - t_1),$$

which can both be evaluated analytically (omitted). Then $\phi_{ij}(\tau)$ can be rewritten as $\phi_{ij} = \sum_{m>m'} P_{mm'} \Omega_m \Omega_{m'} + \sum_m Q_m \Omega_m^2 = X^\top B X$. The matrix B is symmetrized with $B_{mm'} = B_{m'm} \equiv P_{mm'}/2 + Q_m \delta_{mm'}$.

We use the method of Lagrange undetermined multipliers, intending to minimize a modified infidelity $\delta F^* \equiv X^\top A X + \lambda X^\top B X$. From $\partial \delta F^* / \partial X^\top = 0$, we get a generalized eigenvalue equation $A X = \lambda B X$, which can be easily solved by a standard numerical method.

APPENDIX B

Thermal position fluctuation for trapped ions along the axial direction

We address individual ions through focused laser beams which typically take a Gaussian shape along the axial (z) direction with $\Omega_n(z) \propto e^{-z'^2/w^2}$, where $z'_n = z - z_n$ is centered at the equilibrium position z_n of the n th ion. At the Doppler temperature, the ions have significant thermal fluctuation in their positions along the z direction, which leads to an effectively fluctuating laser amplitude $\Omega_n(z)$ and induces infidelity in the gate operation. This position fluctuation influences both the single-bit and the two-bit operations in the same way. To quantify the gate error caused by this fluctuation, let us consider a spin-flip gate operated on the n th ion as a typical example. For a spin-flip with a π -pulse, the gate fidelity is given by $F_1 = \sin^2(\bar{\Omega}_n\tau + \delta\Omega_n\tau) \approx 1 - (\pi^2/4)(\delta\Omega_n/\bar{\Omega}_n)^2$, where $\bar{\Omega}_n$ is the expectation value of the Rabi frequency ($\bar{\Omega}_n\tau = \pi/2$ for a spin-flip gate), and $\delta\Omega_n$ is its fluctuation caused by the position fluctuation of the ion. From $\Omega_n(z) \propto e^{-z'^2/w^2} \approx 1 - z'^2/w^2$ around the equilibrium position, the gate infidelity $\delta F_1 \equiv 1 - F_1 = (\pi^2/4)(\delta z_n/w)^4$, where $\delta z_n \equiv \left(\overline{z'^4} - \overline{z'^2}^2\right)^{1/4}$ characterizes the thermal position fluctuation of the n th ion along the axial direction.

The phonon modes are in thermal equilibrium under the Doppler temperature T , with their density operator given by $\rho_m = \prod_k \sum_{\{n_k\}} P_k |n_k\rangle \langle n_k|$, where $P_k =$

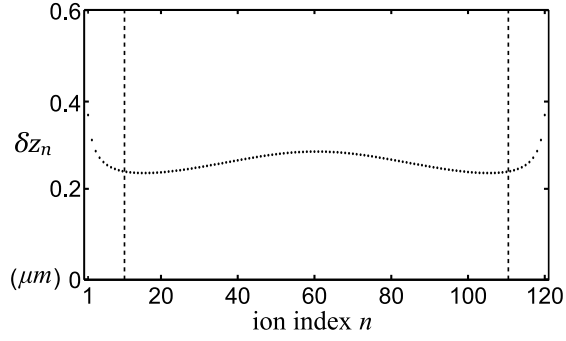


Figure B.1: The axial position fluctuation δz_n is plotted along the ion chain, which is about $0.26\mu\text{m}$ (averaged) for the computational ions (n from 11 to 110).

$\bar{n}_k^{n_k} / (\bar{n}_k + 1)^{n_k+1}$ is the probability of having n_k phonons in the k th mode, and $\bar{n}_k = k_B T / (\hbar \omega_k)$ is the average phonon number. From $\overline{z_n'^2} = \text{tr}(z_n'^2 \rho_m)$ and $\overline{z_n'^4} = \text{tr}(z_n'^4 \rho_m)$, we explicitly have $\delta z_n = \sqrt{\hbar/2m} \left[\sqrt{2} \sum_k (b_n^{z,k})^2 (2\bar{n}_k + 1) / \omega_{z,k} \right]^{1/2}$ where $\omega_{z,k}$ and $b_n^{z,k}$ denote the eigen-frequencies and eigen-matrices of the axial modes. For our example of a 120-ion chain (see Chapter V) with the Doppler temperature $k_B T / \hbar = 62\text{MHz}$ for the Yb^+ ions, the resultant position fluctuation δz_n is plotted in Fig. B.1 for all the ions. One can see that for the computational ions (n from 11 to 110), $\delta z_n \approx 0.26 \mu\text{m}$ with its value almost independent of the ion index. The position fluctuation is still significantly smaller than the ion spacing ($\approx 10 \mu\text{m}$), which ensures a tiny gate infidelity δF_1 as discussed in Chapter V.

BIBLIOGRAPHY

BIBLIOGRAPHY

- [1] Richard Feynman. Simulating physics with computers. *International Journal of Theoretical Physics*, 21(6):467–488, June 1982. doi: 10.1007/BF02650179.
- [2] Kerson Huang. *Statistical Mechanics*. Wiley, 2nd edition, 1987. ISBN-10: 0471815187.
- [3] M. H. Anderson, J. R. Ensher, M. R. Matthews, C. E. Wieman, and E. A. Cornell. Observation of Bose-Einstein condensation in a dilute atomic vapor. *Science*, 269(5221):198–201, 1995. doi: 10.1126/science.269.5221.198.
- [4] Markus Greiner, Cindy A. Regal, and Deborah S. Jin. Emergence of a molecular Bose-Einstein condensate from a Fermi gas. *Nature*, 426(6966):537–540, December 2003. ISSN 0028-0836. doi: 10.1038/nature02199.
- [5] William C. Stwalley. Stability of spin-aligned hydrogen at low temperatures and high magnetic fields: New field-dependent scattering resonances and predissociations. *Phys. Rev. Lett.*, 37(24):1628–1631, Dec 1976. doi: 10.1103/PhysRevLett.37.1628.
- [6] H. T. C. Stoof, M. Houbiers, C. A. Sackett, and R. G. Hulet. Superfluidity of spin-polarized ${}^6\text{Li}$. *Phys. Rev. Lett.*, 76(1):10–13, Jan 1996. doi: 10.1103/PhysRevLett.76.10.
- [7] I. Bloch. Quantum gases in optical lattices. *Physics World*, 17:25–29, 2004.
- [8] Immanuel Bloch, Jean Dalibard, and Wilhelm Zwerger. Many-body physics with ultracold gases. *Rev. Mod. Phys.*, 80(3):885–964, Jul 2008. doi: 10.1103/RevModPhys.80.885.
- [9] Belen Paredes, Artur Widera, Valentin Murg, Olaf Mandel, Simon Fölling, Ignacio Cirac, Gora V. Shlyapnikov, Theodor W. Hansch, and Immanuel Bloch. Tonks-Girardeau gas of ultracold atoms in an optical lattice. *Nature*, 429(6989):277–281, May 2004. ISSN 0028-0836. doi: 10.1038/nature02530.
- [10] Toshiya Kinoshita, Trevor Wenger, and David S. Weiss. Observation of a one-dimensional Tonks-Girardeau gas. *Science*, 305(5687):1125–1128, 2004. doi: 10.1126/science.1100700.
- [11] Henning Moritz, Thilo Stöferle, Kenneth Günter, Michael Köhl, and Tilman Esslinger. Confinement induced molecules in a 1D Fermi gas. *Phys. Rev. Lett.*, 94(21):210401, Jun 2005. doi: 10.1103/PhysRevLett.94.210401.
- [12] Sabine Stock, Zoran Hadzibabic, Baptiste Battelier, Marc Cheneau, and Jean Dalibard. Observation of phase defects in quasi-two-dimensional Bose-Einstein condensates. *Phys. Rev. Lett.*, 95(19):190403, Nov 2005. doi: 10.1103/PhysRevLett.95.190403.
- [13] Gavin K. Brennen, Carlton M. Caves, Poul S. Jessen, and Ivan H. Deutsch. Quantum logic gates in optical lattices. *Phys. Rev. Lett.*, 82(5):1060–1063, Feb 1999. doi: 10.1103/PhysRevLett.82.1060.
- [14] D.J. Wineland, C. Monroe, W. M. Itano, D. Leibfried, B. E. King, and D. M. Meekhof. Experimental issues in coherent quantum-state manipulation of trapped atomic ions. *J. Res. Natl. Inst. Stand. Tech.*, 103:259, 1998. URL <http://nvl.nist.gov/pub/nistpubs/jres/103/3/j33win.pdf>.

- [15] D. Leibfried, R. Blatt, C. Monroe, and D. Wineland. Quantum dynamics of single trapped ions. *Rev. Mod. Phys.*, 75(1):281–324, Mar 2003. doi: 10.1103/RevModPhys.75.281.
- [16] C. C. Tsuei and J. R. Kirtley. Pairing symmetry in cuprate superconductors. *Rev. Mod. Phys.*, 72(4):969, Oct 2000. doi: 10.1103/RevModPhys.72.969.
- [17] Sudip Chakravarty, R. B. Laughlin, Dirk K. Morr, and Chetan Nayak. Hidden order in the cuprates. *Phys. Rev. B*, 63(9):094503, Jan 2001. doi: 10.1103/PhysRevB.63.094503.
- [18] Qijin Chen, Jelena Stajic, Shina Tan, and K. Levin. BCS-BEC crossover: From high temperature superconductors to ultracold superfluids. *Physics Reports*, 412(1):1–88, June 2005. ISSN 0370-1573. doi: 10.1016/j.physrep.2005.02.005.
- [19] N. Read and Dmitry Green. Paired states of fermions in two dimensions with breaking of parity and time-reversal symmetries and the fractional quantum Hall effect. *Phys. Rev. B*, 61(15):10267–10297, Apr 2000. doi: 10.1103/PhysRevB.61.10267.
- [20] Alexander L. Fetter. Rotating trapped Bose-Einstein condensates. *Rev. Mod. Phys.*, 81(2):647–691, May 2009. doi: 10.1103/RevModPhys.81.647.
- [21] J. Bardeen, L. N. Cooper, and J. R. Schrieffer. Microscopic theory of superconductivity. *Phys. Rev.*, 106(1):162–164, Apr 1957. doi: 10.1103/PhysRev.106.162.
- [22] S. Inouye, M. R. Andrews, J. Stenger, H.-J. Miesner, D. M. Stamper-Kurn, and W. Ketterle. Observation of Feshbach resonances in a Bose-Einstein condensate. *Nature*, 392(6672):151–154, March 1998. ISSN 0028-0836. doi: 10.1038/32354.
- [23] R. A. Duine and H. T. C. Stoof. Atom-molecule coherence in Bose gases. *Physics Reports*, 396(3):115–195, June 2004. ISSN 0370-1573. doi: 10.1016/j.physrep.2004.03.003.
- [24] Aurel Bulgac. Specific heat of a fermionic atomic cloud in the unitary regime. *Phys. Rev. Lett.*, 95(14):140403, Sep 2005. doi: 10.1103/PhysRevLett.95.140403.
- [25] J. E. Thomas, J. Kinast, and A. Turlapov. Virial theorem and universality in a unitary Fermi gas. *Phys. Rev. Lett.*, 95(12):120402, Sep 2005. doi: 10.1103/PhysRevLett.95.120402.
- [26] Paulo F. Bedaque, Heron Caldas, and Gautam Rupak. Phase separation in asymmetrical fermion superfluids. *Phys. Rev. Lett.*, 91(24):247002, Dec 2003. doi: 10.1103/PhysRevLett.91.247002.
- [27] Martin W. Zwierlein, André Schirotzek, Christian H. Schunck, and Wolfgang Ketterle. Fermionic superfluidity with imbalanced spin populations. *Science*, 311(5760):492–496, 2006. doi: 10.1126/science.1122318.
- [28] Guthrie B. Partridge, Wenhui Li, Ramsey I. Kamar, Yean-an Liao, and Randall G. Hulet. Pairing and phase separation in a polarized Fermi gas. *Science*, 311(5760):503–505, 2006. doi: 10.1126/science.1122876.
- [29] Martin W. Zwierlein, Christian H. Schunck, André Schirotzek, and Wolfgang Ketterle. Direct observation of the superfluid phase transition in ultracold Fermi gases. *Nature*, 442(7098):54–58, July 2006. ISSN 0028-0836. doi: 10.1038/nature04936.
- [30] Masudul Haque and H. T. C. Stoof. Pairing of a trapped resonantly interacting fermion mixture with unequal spin populations. *Phys. Rev. A*, 74(1):011602(R), Jul 2006. doi: 10.1103/PhysRevA.74.011602.
- [31] Daniel E. Sheehy and Leo Radzihovsky. BEC-BCS crossover in “magnetized” Feshbach-resonantly paired superfluids. *Phys. Rev. Lett.*, 96(6):060401, Feb 2006. doi: 10.1103/PhysRevLett.96.060401.

- [32] Y. Shin, M. W. Zwierlein, C. H. Schunck, A. Schirotzek, and W. Ketterle. Observation of phase separation in a strongly interacting imbalanced Fermi gas. *Phys. Rev. Lett.*, 97(3):030401, Jul 2006. doi: 10.1103/PhysRevLett.97.030401.
- [33] Daniel E. Sheehy and Leo Radzihovsky. BEC-BCS crossover, phase transitions and phase separation in polarized resonantly-paired superfluids. *Annals of Physics*, 322(8):1790–1924, August 2007. ISSN 0003-4916. doi: 10.1016/j.aop.2006.09.009.
- [34] Michael McNeil Forbes, Elena Gubankova, W. Vincent Liu, and Frank Wilczek. Stability criteria for breached-pair superfluidity. *Phys. Rev. Lett.*, 94(1):017001, Jan 2005. doi: 10.1103/PhysRevLett.94.017001.
- [35] C.-H. Pao, Shin-Tza Wu, and S.-K. Yip. Superfluid stability in the BEC-BCS crossover. *Phys. Rev. B*, 73(13):132506, Apr 2006. doi: 10.1103/PhysRevB.73.132506.
- [36] Peter Fulde and Richard A. Ferrell. Superconductivity in a strong spin-exchange field. *Phys. Rev.*, 135(3A):A550–A563, Aug 1964. doi: 10.1103/PhysRev.135.A550.
- [37] A. I. Larkin and Y. N. Ovchinnikov. Nonuniform state of superconductors. *Zh. Eksp. Teor. Fiz.*, 47:1136–1146, 1964. [Sov. Phys. JETP, 20:762, 1965].
- [38] Pierre Meystre. *Atom Optics*. Springer, 1st edition, 2001. ISBN-10: 0387952748.
- [39] S. S. Botelho and C. A. R. Sá de Melo. Vortex-antivortex lattice in ultracold fermionic gases. *Phys. Rev. Lett.*, 96(4):040404, Feb 2006. doi: 10.1103/PhysRevLett.96.040404.
- [40] I. B. Spielman, W. D. Phillips, and J. V. Porto. Condensate fraction in a 2D Bose gas measured across the Mott-insulator transition. *Phys. Rev. Lett.*, 100(12):120402, Mar 2008. doi: 10.1103/PhysRevLett.100.120402.
- [41] John Hubbard. Electron correlations in narrow energy bands. *Proceedings of the Royal Society of London. Series A, Mathematical and Physical Sciences*, 276(1365):238–257, November 1963. URL <http://www.jstor.org/pss/2414761>.
- [42] Markus Greiner, Olaf Mandel, Tilman Esslinger, Theodor W. Hänsch, and Immanuel Bloch. Quantum phase transition from a superfluid to a Mott insulator in a gas of ultracold atoms. *Nature*, 415(6867):39–44, January 2002. ISSN 0028-0836. doi: 10.1038/415039a.
- [43] Fabrice Gerbier, Artur Widera, Simon Fölling, Olaf Mandel, Tatjana Gericke, and Immanuel Bloch. Phase coherence of an atomic Mott insulator. *Phys. Rev. Lett.*, 95(5):050404, Jul 2005. doi: 10.1103/PhysRevLett.95.050404.
- [44] J. K. Chin, D. E. Miller, Y. Liu, C. Stan, W. Setiawan, C. Sanner, K. Xu, and W. Ketterle. Evidence for superfluidity of ultracold fermions in an optical lattice. *Nature*, 443(7114):961–964, October 2006. ISSN 0028-0836. doi: 10.1038/nature05224.
- [45] D. van Oosten, P. van der Straten, and H. T. C. Stoof. Quantum phases in an optical lattice. *Phys. Rev. A*, 63(5):053601, Apr 2001. doi: 10.1103/PhysRevA.63.053601.
- [46] Matthew P. A. Fisher, Peter B. Weichman, G. Grinstein, and Daniel S. Fisher. Boson localization and the superfluid-insulator transition. *Phys. Rev. B*, 40(1):546–570, Jul 1989. doi: 10.1103/PhysRevB.40.546.
- [47] Roberto B. Diener, Qi Zhou, Hui Zhai, and Tin-Lun Ho. Criterion for bosonic superfluidity in an optical lattice. *Phys. Rev. Lett.*, 98(18):180404, May 2007. doi: 10.1103/PhysRevLett.98.180404.
- [48] Fabrice Gerbier, Simon Fölling, Artur Widera, and Immanuel Bloch. Visibility of a Bose-condensed gas released from an optical lattice at finite temperatures. *arXiv:cond-mat/0701420v1*, 2007. URL <http://arxiv.org/abs/cond-mat/0701420v1>.

- [49] W. Yi, G.-D. Lin, and L.-M. Duan. Signal of Bose-Einstein condensation in an optical lattice at finite temperature. *Phys. Rev. A*, 76(3):031602(R), Sep 2007. doi: 10.1103/PhysRevA.76.031602.
- [50] D. Deutsch. Quantum theory, the Church-Turing principle and the universal quantum computer. *Proceedings of the Royal Society of London. A. Mathematical and Physical Sciences*, 400(1818):97–117, 1985. doi: 10.1098/rspa.1985.0070.
- [51] Seth Lloyd. Universal quantum simulators. *Science*, 273(5278):1073–1078, 1996. doi: 10.1126/science.273.5278.1073.
- [52] Michael A. Nielsen and Isaac L. Chuang. *Quantum Computation and Quantum Information*. Cambridge University Press, 1 edition, September 2000. ISBN-10: 0521635039.
- [53] J. I. Cirac and P. Zoller. Quantum computations with cold trapped ions. *Phys. Rev. Lett.*, 74(20):4091–4094, May 1995. doi: 10.1103/PhysRevLett.74.4091.
- [54] Anders Sørensen and Klaus Mølmer. Quantum computation with ions in thermal motion. *Phys. Rev. Lett.*, 82(9):1971–1974, Mar 1999. doi: 10.1103/PhysRevLett.82.1971.
- [55] Klaus Mølmer and Anders Sørensen. Multiparticle entanglement of hot trapped ions. *Phys. Rev. Lett.*, 82(9):1835–1838, Mar 1999. doi: 10.1103/PhysRevLett.82.1835.
- [56] Anders Sørensen and Klaus Mølmer. Entanglement and quantum computation with ions in thermal motion. *Phys. Rev. A*, 62(2):022311, Jul 2000. doi: 10.1103/PhysRevA.62.022311.
- [57] G.J. Milburn, S. Schneider, and D.F.V. James. Ion trap quantum computing with warm ions. *Fortschritte der Physik*, 48(9-11):801–810, 2000. doi: 10.1002/1521-3978(200009)48:9/11(801::AID-PROP801)3.0.CO;2-1.
- [58] J. J. García-Ripoll, P. Zoller, and J. I. Cirac. Speed optimized two-qubit gates with laser coherent control techniques for ion trap quantum computing. *Phys. Rev. Lett.*, 91(15):157901, Oct 2003. doi: 10.1103/PhysRevLett.91.157901.
- [59] J. J. García-Ripoll, P. Zoller, and J. I. Cirac. Coherent control of trapped ions using off-resonant lasers. *Phys. Rev. A*, 71(6):062309, Jun 2005. doi: 10.1103/PhysRevA.71.062309.
- [60] Shi-Liang Zhu, C. Monroe, and L.-M. Duan. Trapped ion quantum computation with transverse phonon modes. *Phys. Rev. Lett.*, 97(5):050505, Aug 2006. doi: 10.1103/PhysRevLett.97.050505.
- [61] Shi-Liang Zhu, C. Monroe, and L.-M. Duan. Arbitrary-speed quantum gates within large ion crystals through minimum control of laser beams. *Europhys. Lett.*, 73(4):485, 2006. doi: 10.1209/epl/i2005-10424-4.
- [62] D. Porras and J. I. Cirac. Effective quantum spin systems with trapped ions. *Phys. Rev. Lett.*, 92(20):207901, May 2004. doi: 10.1103/PhysRevLett.92.207901.
- [63] A. Friedenauer, H. Schmitz, J. T. Glueckert, D. Porras, and T. Schaetz. Simulating a quantum magnet with trapped ions. *Nature Physics*, 4(10):757–761, October 2008. ISSN 1745-2473. doi: 10.1038/nphys1032.
- [64] K. Kim, M.-S. Chang, R. Islam, S. Korenblit, L.-M. Duan, and C. Monroe. Entanglement and tunable spin-spin couplings between trapped ions using multiple transverse modes. *Phys. Rev. Lett.*, 103(12):120502, Sep 2009. doi: 10.1103/PhysRevLett.103.120502.
- [65] X.-L. Deng, D. Porras, and J. I. Cirac. Effective spin quantum phases in systems of trapped ions. *Phys. Rev. A*, 72(6):063407, Dec 2005. doi: 10.1103/PhysRevA.72.063407.

- [66] G.-D. Lin, W. Yi, and L.-M. Duan. Superfluid shells for trapped fermions with mass and population imbalance. *Phys. Rev. A*, 74(3):031604(R), Sep 2006. doi: 10.1103/PhysRevA.74.031604.
- [67] Wei Zhang, G.-D. Lin, and L.-M. Duan. BCS-BEC crossover of a quasi-two-dimensional Fermi gas: The significance of dressed molecules. *Phys. Rev. A*, 77(6):063613, Jun 2008. doi: 10.1103/PhysRevA.77.063613.
- [68] G.-D. Lin, Wei Zhang, and L.-M. Duan. Characteristics of Bose-Einstein condensation in an optical lattice. *Phys. Rev. A*, 77(4):043626, Apr 2008. doi: 10.1103/PhysRevA.77.043626.
- [69] G.-D. Lin, S.-L. Zhu, R. Islam, K. Kim, M.-S. Chang, S. Korenblit, C. Monroe, and L.-M. Duan. Large-scale quantum computation in an anharmonic linear ion trap. *Europhys. Lett.*, 86(6):60004 (5pp), 2009. doi: 10.1209/0295-5075/86/60004.
- [70] K. Kim, M.-S. Chang, S. Korenblit, R. Islam, E. E. Edwards, J. K. Freericks, G.-D. Lin, L.-M. Duan, and C. Monroe. Quantum simulation of frustrated Ising spins with trapped ions. 2010. Accepted by *Nature*.
- [71] W. Yi and L.-M. Duan. Trapped fermions across a Feshbach resonance with population imbalance. *Phys. Rev. A*, 73(3):031604(R), Mar 2006. doi: 10.1103/PhysRevA.73.031604.
- [72] W. Yi and L.-M. Duan. Phase diagram of a polarized Fermi gas across a Feshbach resonance in a potential trap. *Phys. Rev. A*, 74(1):013610, Jul 2006. doi: 10.1103/PhysRevA.74.013610.
- [73] T. N. De Silva and E. J. Mueller. Profiles of near-resonant population-imbalanced trapped Fermi gases. *Phys. Rev. A*, 73(5):051602(R), May 2006. doi: 10.1103/PhysRevA.73.051602.
- [74] P. Pieri and G. C. Strinati. Trapped fermions with density imbalance in the Bose-Einstein condensate limit. *Phys. Rev. Lett.*, 96(15):150404, Apr 2006. doi: 10.1103/PhysRevLett.96.150404.
- [75] J. Kinnunen, L. M. Jensen, and P. Törmä. Strongly interacting Fermi gases with density imbalance. *Phys. Rev. Lett.*, 96(11):110403, Mar 2006. doi: 10.1103/PhysRevLett.96.110403.
- [76] F. Chevy. Density profile of a trapped strongly interacting Fermi gas with unbalanced spin populations. *Phys. Rev. Lett.*, 96(13):130401, Apr 2006. doi: 10.1103/PhysRevLett.96.130401.
- [77] Tin-Lun Ho and Hui Zhai. Homogeneous fermion superfluid with unequal spin populations. *J. Low Temp. Phys.*, 148(1):33–41, July 2007. doi: 10.1007/s10909-007-9350-9.
- [78] Chih-Chun Chien, Qijin Chen, Yan He, and K. Levin. Finite temperature effects in trapped Fermi gases with population imbalance. *Phys. Rev. A*, 74(2):021602(R), Aug 2006. doi: 10.1103/PhysRevA.74.021602.
- [79] C. A. Stan, M. W. Zwierlein, C. H. Schunck, S. M. F. Raupach, and W. Ketterle. Observation of Feshbach resonances between two different atomic species. *Phys. Rev. Lett.*, 93(14):143001, Sep 2004. doi: 10.1103/PhysRevLett.93.143001.
- [80] S. Inouye, J. Goldwin, M. L. Olsen, C. Ticknor, J. L. Bohn, and D. S. Jin. Observation of heteronuclear Feshbach resonances in a mixture of bosons and fermions. *Phys. Rev. Lett.*, 93(18):183201, Oct 2004. doi: 10.1103/PhysRevLett.93.183201.
- [81] E. Wille, F. M. Spiegelhalder, G. Kerner, D. Naik, A. Trenkwalder, G. Hendl, F. Schreck, R. Grimm, T. G. Tiecke, J. T. M. Walraven, S. J. J. M. F. Kokkelmans, E. Tiesinga, and P. S. Julienne. Exploring an ultracold Fermi-Fermi mixture: Interspecies Feshbach resonances and scattering properties of ${}^6\text{Li}$ and ${}^4\text{K}$. *Phys. Rev. Lett.*, 100(5):053201, Feb 2008. doi: 10.1103/PhysRevLett.100.053201.

- [82] M. Taglieber, A.-C. Voigt, T. Aoki, T. W. Hänsch, and K. Dieckmann. Quantum degenerate two-species Fermi-Fermi mixture coexisting with a Bose-Einstein condensate. *Phys. Rev. Lett.*, 100(1):010401, Jan 2008. doi: 10.1103/PhysRevLett.100.010401.
- [83] A.-C. Voigt, M. Taglieber, L. Costa, T. Aoki, W. Wieser, T. W. Hänsch, and K. Dieckmann. Ultracold heteronuclear Fermi-Fermi molecules. *Phys. Rev. Lett.*, 102(2):020405, Jan 2009. doi: 10.1103/PhysRevLett.102.020405.
- [84] T. G. Tiecke, M. R. Goosen, A. Ludewig, S. D. Gensemer, S. Kraft, S. J. J. M. F. Kokkelmans, and J. T. M. Walraven. Broad Feshbach resonance in the ${}^6\text{Li}$ - ${}^40\text{K}$ mixture. *Phys. Rev. Lett.*, 104(5):053202, Feb 2010. doi: 10.1103/PhysRevLett.104.053202.
- [85] M. Iskin and C. A. R. Sá de Melo. Two-species fermion mixtures with population imbalance. *Phys. Rev. Lett.*, 97(10):100404, Sep 2006. doi: 10.1103/PhysRevLett.97.100404.
- [86] M. Iskin and C. A. R. Sá de Melo. Asymmetric two-component Fermi gas with unequal masses. *arXiv:cond-mat/0606624v2*, 2006. URL <http://arxiv.org/abs/cond-mat/0606624>.
- [87] Shin-Tza Wu, C.-H. Pao, and S.-K. Yip. Resonant pairing between fermions with unequal masses. *Phys. Rev. B*, 74(22):224504, Dec 2006. doi: 10.1103/PhysRevB.74.224504.
- [88] J. von Stecher, Chris H. Greene, and D. Blume. BEC-BCS crossover of a trapped two-component Fermi gas with unequal masses. *Phys. Rev. A*, 76(5):053613, Nov 2007. doi: 10.1103/PhysRevA.76.053613.
- [89] C.-H. Pao, Shin-Tza Wu, and S.-K. Yip. Asymmetric Fermi superfluid with different atomic species in a harmonic trap. *Phys. Rev. A*, 76(5):053621, Nov 2007. doi: 10.1103/PhysRevA.76.053621.
- [90] T. Paananen, P. Törmä, and J.-P. Martikainen. Coexistence and shell structures of several superfluids in trapped three-component Fermi mixtures. *Phys. Rev. A*, 75(2):023622, Feb 2007. doi: 10.1103/PhysRevA.75.023622.
- [91] M. M. Parish, F. M. Marchetti, A. Lamacraft, and B. D. Simons. Polarized Fermi condensates with unequal masses: Tuning the tricritical point. *Phys. Rev. Lett.*, 98(16):160402, Apr 2007. doi: 10.1103/PhysRevLett.98.160402.
- [92] M. Iskin and C. A. R. Sá de Melo. Mixtures of ultracold fermions with unequal masses. *Phys. Rev. A*, 76(1):013601, Jul 2007. doi: 10.1103/PhysRevA.76.013601.
- [93] M. Iskin and C. A. R. Sá de Melo. Fermi-Fermi mixtures in the strong-attraction limit. *Phys. Rev. A*, 77(1):013625, Jan 2008. doi: 10.1103/PhysRevA.77.013625.
- [94] M. Holland, S. J. J. M. F. Kokkelmans, M. L. Chiofalo, and R. Walser. Resonance superfluidity in a quantum degenerate Fermi gas. *Phys. Rev. Lett.*, 87(12):120406, Aug 2001. doi: 10.1103/PhysRevLett.87.120406.
- [95] Y. Ohashi and A. Griffin. BCS-BEC crossover in a gas of Fermi atoms with a Feshbach resonance. *Phys. Rev. Lett.*, 89(13):130402, Sep 2002. doi: 10.1103/PhysRevLett.89.130402.
- [96] Roberto B. Diener and Tin-Lun Ho. The condition for universality at resonance and direct measurement of pair wavefunctions using RF spectroscopy. *arXiv:cond-mat/0405174v2*, 2004. URL <http://arxiv.org/abs/cond-mat/0405174v2>.
- [97] A. J. Leggett. *Modern Trends in the Theory of Condensed Matter*. Springer-Verlag, Berlin, 1980.
- [98] P. Nozières and S. Schmitt-Rink. Bose condensation in an attractive fermion gas: From weak to strong coupling superconductivity. *J. Low Temp. Phys.*, 59(3):195–211, May 1985. doi: 10.1007/BF00683774.

- [99] C. A. R. Sá de Melo, Mohit Randeria, and Jan R. Engelbrecht. Crossover from BCS to Bose superconductivity: Transition temperature and time-dependent Ginzburg-Landau theory. *Phys. Rev. Lett.*, 71(19):3202–3205, Nov 1993. doi: 10.1103/PhysRevLett.71.3202.
- [100] Marzena H. Szymańska, Krzysztof Góral, Thorsten Köhler, and Keith Burnett. Conventional character of the BCS-BEC crossover in ultracold gases of $^4\text{0K}$. *Phys. Rev. A*, 72(1):013610, Jul 2005. doi: 10.1103/PhysRevA.72.013610.
- [101] Stefano Giorgini, Lev P. Pitaevskii, and Sandro Stringari. Theory of ultracold atomic Fermi gases. *Rev. Mod. Phys.*, 80(4):1215–1274, Oct 2008. doi: 10.1103/RevModPhys.80.1215.
- [102] W. Yi and L.-M. Duan. Detecting the breached-pair phase in a polarized ultracold Fermi gas. *Phys. Rev. Lett.*, 97(12):120401, Sep 2006. doi: 10.1103/PhysRevLett.97.120401.
- [103] Thilo Stöferle, Henning Moritz, Kenneth Günter, Michael Köhl, and Tilman Esslinger. Molecules of fermionic atoms in an optical lattice. *Phys. Rev. Lett.*, 96(3):030401, Jan 2006. doi: 10.1103/PhysRevLett.96.030401.
- [104] Zoran Hadzibabic, Peter Krüger, Marc Cheneau, Baptiste Battelier, and Jean Dalibard. Berezinskii-Kosterlitz-Thouless crossover in a trapped atomic gas. *Nature*, 441(7097):1118–1121, June 2006. ISSN 0028-0836. doi: 10.1038/nature04851.
- [105] Fortágh, József and Claus Zimmermann. Magnetic microtraps for ultracold atoms. *Rev. Mod. Phys.*, 79(1):235–289, Feb 2007. doi: 10.1103/RevModPhys.79.235.
- [106] Mohit Randeria, Ji-Min Duan, and Lih-Yir Shieh. Superconductivity in a two-dimensional Fermi gas: Evolution from Cooper pairing to Bose condensation. *Phys. Rev. B*, 41(1):327–343, Jan 1990. doi: 10.1103/PhysRevB.41.327.
- [107] M. Marini, F. Pistolesi, and G.C. Strinati. Evolution from BCS superconductivity to Bose condensation: analytic results for the crossover in three dimensions. *The European Physical Journal B - Condensed Matter and Complex Systems*, 1(2):151–159, February 1998. doi: 10.1007/s100510050165.
- [108] D. S. Petrov, M. Holzmann, and G. V. Shlyapnikov. Bose-Einstein condensation in quasi-2D trapped gases. *Phys. Rev. Lett.*, 84(12):2551–2555, Mar 2000. doi: 10.1103/PhysRevLett.84.2551.
- [109] T. Bergeman, M. G. Moore, and M. Olshanii. Atom-atom scattering under cylindrical harmonic confinement: Numerical and analytic studies of the confinement induced resonance. *Phys. Rev. Lett.*, 91(16):163201, Oct 2003. doi: 10.1103/PhysRevLett.91.163201.
- [110] J. P. Kestner and L.-M. Duan. Effective low-dimensional Hamiltonian for strongly interacting atoms in a transverse trap. *Phys. Rev. A*, 76(6):063610, Dec 2007. doi: 10.1103/PhysRevA.76.063610.
- [111] L.-M. Duan. Effective Hamiltonian for fermions in an optical lattice across a Feshbach resonance. *Phys. Rev. Lett.*, 95(24):243202, Dec 2005. doi: 10.1103/PhysRevLett.95.243202.
- [112] J. P. Kestner and L.-M. Duan. Conditions of low dimensionality for strongly interacting atoms under a transverse trap. *Phys. Rev. A*, 74(5):053606, Nov 2006. doi: 10.1103/PhysRevA.74.053606.
- [113] Anna Posazhennikova. Colloquium: Weakly interacting, dilute Bose gases in 2D. *Rev. Mod. Phys.*, 78(4):1111–1134, Oct 2006. doi: 10.1103/RevModPhys.78.1111.
- [114] I. V. Tokatly. Bose representation for a strongly coupled nonequilibrium fermionic superfluid in a time-dependent trap. *Phys. Rev. A*, 70(4):043601, Oct 2004. doi: 10.1103/PhysRevA.70.043601.

- [115] I. Bloch and M. Greiner. Exploring quantum matter with ultracold atoms in optical lattices. *Adv. At., Mol., Opt. Phys.*, 52:1, 2005.
- [116] Jens O. Andersen. Theory of the weakly interacting Bose gas. *Rev. Mod. Phys.*, 76(2): 599–639, Jul 2004. doi: 10.1103/RevModPhys.76.599.
- [117] Ana Maria Rey, Keith Burnett, Robert Roth, Mark Edwards, Carl J Williams, and Charles W Clark. Bogoliubov approach to superfluidity of atoms in an optical lattice. *Journal of Physics B: Atomic, Molecular and Optical Physics*, 36(5):825, 2003. doi: 10.1088/0953-4075/36/5/304.
- [118] Hua Shi and Allan Griffin. Finite-temperature excitations in a dilute Bose-condensed gas. *Physics Reports*, 304(1-2):1–87, 1998. ISSN 0370-1573. doi: 10.1016/S0370-1573(98)00015-5.
- [119] . The cases of different lattice structures and anisotropic trapping potentials can be analyzed analogously, provided that the anisotropy of the global trap is not strong enough to cause a breakdown of LDA.
- [120] Anatoli Polkovnikov, Subir Sachdev, and S. M. Girvin. Nonequilibrium Gross-Pitaevskii dynamics of boson lattice models. *Phys. Rev. A*, 66(5):053607, Nov 2002. doi: 10.1103/PhysRevA.66.053607.
- [121] Chris Hooley and Jorge Quintanilla. Single-atom density of states of an optical lattice. *Phys. Rev. Lett.*, 93(8):080404, Aug 2004. doi: 10.1103/PhysRevLett.93.080404.
- [122] Ana Maria Rey, Guido Pupillo, Charles W. Clark, and Carl J. Williams. Ultracold atoms confined in an optical lattice plus parabolic potential: A closed-form approach. *Phys. Rev. A*, 72(3):033616, Sep 2005. doi: 10.1103/PhysRevA.72.033616.
- [123] Franco Dalfovo, Stefano Giorgini, Lev P. Pitaevskii, and Sandro Stringari. Theory of Bose-Einstein condensation in trapped gases. *Rev. Mod. Phys.*, 71(3):463–512, Apr 1999. doi: 10.1103/RevModPhys.71.463.
- [124] . In this work, we have assumed that the expansion time is long enough so that the final absorption image represents the initial momentum distribution (the far-field limit). In real experiments, the expansion time may not be long enough to achieve this far-field limit [I. Bloch (private communication)]. This leads to some effective momentum broadening effect seen in observation, which looks similar to the momentum broadening caused by the atomic interaction. However, these two effects should be distinguished. According to the calculation here, the interaction induced momentum broadening is actually not significant for a condensate with a moderate density (such as about one atom per site). The effective broadening effect seen in observation caused by the finite expansion time, in principle, can be undone theoretically if one knows the initial condensate profile and the expansion time.
- [125] Rainer Blatt and David Wineland. Entangled states of trapped atomic ions. *Nature*, 453 (7198):1008–1015, June 2008. ISSN 0028-0836. doi: 10.1038/nature07125.
- [126] H. Häffner, C.F. Roos, and R. Blatt. Quantum computing with trapped ions. *Physics Reports*, 469(4):155–203, December 2008. ISSN 0370-1573. doi: 10.1016/j.physrep.2008.09.003.
- [127] C. Monroe, D. M. Meekhof, B. E. King, W. M. Itano, and D. J. Wineland. Demonstration of a fundamental quantum logic gate. *Phys. Rev. Lett.*, 75(25):4714–4717, Dec 1995. doi: 10.1103/PhysRevLett.75.4714.
- [128] Ferdinand Schmidt-Kaler, Hartmut Häffner, Mark Riebe, Stephan Gulde, Gavin P. T. Lancaster, Thomas Deuschle, Christoph Becher, Christian F. Roos, Jurgen Eschner, and Rainer Blatt. Realization of the Cirac-Zoller controlled-NOT quantum gate. *Nature*, 422(6930): 408–411, March 2003. ISSN 0028-0836. doi: 10.1038/nature01494.

- [129] D. Leibfried, B. DeMarco, V. Meyer, D. Lucas, M. Barrett, J. Britton, W. M. Itano, B. Jenković, C. Langer, T. Rosenband, and D. J. Wineland. Experimental demonstration of a robust, high-fidelity geometric two ion-qubit phase gate. *Nature*, 422(6930):412–415, March 2003. ISSN 0028-0836. doi: 10.1038/nature01492.
- [130] L.-M. Duan. Scaling ion trap quantum computation through fast quantum gates. *Phys. Rev. Lett.*, 93(10):100502, Sep 2004. doi: 10.1103/PhysRevLett.93.100502.
- [131] C. A. Sackett, D. Kielpinski, B. E. King, C. Langer, V. Meyer, C. J. Myatt, M. Rowe, Q. A. Turchette, W. M. Itano, D. J. Wineland, and C. Monroe. Experimental entanglement of four particles. *Nature*, 404(6775):256–259, March 2000. ISSN 0028-0836. doi: 10.1038/35005011.
- [132] H. Häffner, W. Hänsel, C. F. Roos, J. Benhelm, D. Chek-al-kar, M. Chwalla, T. Körber, U. D. Rapol, M. Riebe, P. O. Schmidt, C. Becher, O. Gühne, W. Dür, and R. Blatt. Scalable multiparticle entanglement of trapped ions. *Nature*, 438(7068):643–646, December 2005. ISSN 0028-0836. doi: 10.1038/nature04279.
- [133] D. Leibfried, E. Knill, S. Seidelin, J. Britton, R. B. Blakestad, J. Chiaverini, D. B. Hume, W. M. Itano, J. D. Jost, C. Langer, R. Ozeri, R. Reichle, and D. J. Wineland. Creation of a six-atom ‘Schrödinger cat’ state. *Nature*, 438(7068):639–642, December 2005. ISSN 0028-0836. doi: 10.1038/nature04251.
- [134] D. L. Moehring, P. Maunz, S. Olmschenk, K. C. Younge, D. N. Matsukevich, L.-M. Duan, and C. Monroe. Entanglement of single-atom quantum bits at a distance. *Nature*, 449(7158):68–71, September 2007. ISSN 0028-0836. doi: 10.1038/nature06118.
- [135] M. Riebe, H. Häffner, C. F. Roos, W. Hänsel, J. Benhelm, G. P. T. Lancaster, T. W. Körber, C. Becher, F. Schmidt-Kaler, D. F. V. James, and R. Blatt. Deterministic quantum teleportation with atoms. *Nature*, 429(6993):734–737, June 2004. ISSN 0028-0836. doi: 10.1038/nature02570.
- [136] S. Olmschenk, D. N. Matsukevich, P. Maunz, D. Hayes, L.-M. Duan, and C. Monroe. Quantum teleportation between distant matter qubits. *Science*, 323(5913):486–489, 2009. doi: 10.1126/science.1167209.
- [137] D. Porras and J. I. Cirac. Quantum manipulation of trapped ions in two dimensional Coulomb crystals. *Phys. Rev. Lett.*, 96(25):250501, Jun 2006. doi: 10.1103/PhysRevLett.96.250501.
- [138] J. I. Cirac and P. Zoller. A scalable quantum computer with ions in an array of microtraps. *Nature*, 404(6778):579–581, April 2000. ISSN 0028-0836. doi: 10.1038/35007021.
- [139] J. P. Schiffer. Phase transitions in anisotropically confined ionic crystals. *Phys. Rev. Lett.*, 70(6):818–821, Feb 1993. doi: 10.1103/PhysRevLett.70.818.
- [140] Daniel H. E. Dubin. Theory of structural phase transitions in a trapped Coulomb crystal. *Phys. Rev. Lett.*, 71(17):2753–2756, Oct 1993. doi: 10.1103/PhysRevLett.71.2753.
- [141] D. Kielpinski, C. Monroe, and D. J. Wineland. Architecture for a large-scale ion-trap quantum computer. *Nature*, 417(6890):709–711, June 2002. ISSN 0028-0836. doi: 10.1038/nature00784.
- [142] L.-M. Duan, B.B. Blinov, D.L. Moehring, and C. Monroe. Scalable trapped ion quantum computation with a probabilistic ion-photon mapping. *Quant. Inf. Comp.*, 4:165–173, 2004.
- [143] D. L. Moehring, M. J. Madsen, K. C. Younge, R. N. Kohn, Jr., P. Maunz, L.-M. Duan, C. Monroe, and B. B. Blinov. Quantum networking with photons and trapped atoms (Invited). *J. Opt. Soc. Am. B*, 24(2):300–315, February 2007. doi: 10.1364/JOSAB.24.000300.
- [144] A. Steane. The ion trap quantum information processor. *Applied Physics B: Lasers and Optics*, 64(6):623–643, June 1997. doi: 10.1007/s003400050225.

- [145] Robert Raussendorf and Jim Harrington. Fault-tolerant quantum computation with high threshold in two dimensions. *Phys. Rev. Lett.*, 98(19):190504, May 2007. doi: 10.1103/PhysRevLett.98.190504.
- [146] K. M. Svore, D. P. DiVincenzo, and B. M. Terhal. Noise threshold for a fault-tolerant two-dimensional lattice architecture. *Quant. Inf. Comp.*, 7:297–318, 2007.
- [147] T. Szkopek, P.O. Boykin, Heng Fan, V.P. Roychowdhury, E. Yablonovitch, G. Simms, M. Gyure, and B. Fong. Threshold error penalty for fault-tolerant quantum computation with nearest neighbor communication. *Nanotechnology, IEEE Transactions on*, 5(1):42 – 49, jan. 2006. ISSN 1536-125X. doi: 10.1109/TNANO.2005.861402.
- [148] Daniel Gottesman. Fault-tolerant quantum computation with local gates. *J. of Mod. Optics*, 47(2):333–345, 2000. doi: 10.1080/09500340008244046.
- [149] Michael Johanning, Andrés F Varón, and Christof Wunderlich. Quantum simulations with cold trapped ions. *Journal of Physics B: Atomic, Molecular and Optical Physics*, 42(15):154009, 2009. doi: 10.1088/0953-4075/42/15/154009.
- [150] D. Porras, F. Marquardt, J. von Delft, and J. I. Cirac. Mesoscopic spin-boson models of trapped ions. *Phys. Rev. A*, 78(1):010101, Jul 2008. doi: 10.1103/PhysRevA.78.010101.
- [151] Marisa Pons, Veronica Ahufinger, Christof Wunderlich, Anna Sanpera, Sibylle Braungardt, Aditi Sen(De), Ujjwal Sen, and Maciej Lewenstein. Trapped ion chain as a neural network: Error resistant quantum computation. *Phys. Rev. Lett.*, 98(2):023003, Jan 2007. doi: 10.1103/PhysRevLett.98.023003.
- [152] P. A. Ivanov, S. S. Ivanov, N. V. Vitanov, A. Mering, M. Fleischhauer, and K. Singer. Simulation of a quantum phase transition of polaritons with trapped ions. *Phys. Rev. A*, 80(6):060301, Dec 2009. doi: 10.1103/PhysRevA.80.060301.
- [153] D. Porras and J. I. Cirac. Bose-Einstein condensation and strong-correlation behavior of phonons in ion traps. *Phys. Rev. Lett.*, 93(26):263602, Dec 2004. doi: 10.1103/PhysRevLett.93.263602.
- [154] H. T. Diep. *Frustrated Spin Systems*. World Scientific Publishing Company, April 2005. ISBN-10: 9812560912.
- [155] R. Moessner and A. P. Ramirez. Geometrical frustration. *Phys. Today*, 59:24–29, 2006.
- [156] S. Sachdev. *Quantum Phase Transitions*. Cambridge University Press, Cambridge, 1999.
- [157] K. Binder and A. P. Young. Spin glasses: Experimental facts, theoretical concepts, and open questions. *Rev. Mod. Phys.*, 58(4):801–976, Oct 1986. doi: 10.1103/RevModPhys.58.801.
- [158] Christopher M. Dawson and Michael A. Nielsen. Frustration, interaction strength, and ground-state entanglement in complex quantum systems. *Phys. Rev. A*, 69(5):052316, May 2004. doi: 10.1103/PhysRevA.69.052316.
- [159] Bruce Normand and Andrzej M. Oleś. Frustration and entanglement in the t_{2g} spin-orbital model on a triangular lattice: Valence-bond and generalized liquid states. *Phys. Rev. B*, 78(9):094427, Sep 2008. doi: 10.1103/PhysRevB.78.094427.
- [160] Otfried Gühne and Géza Tóth. Entanglement detection. *Physics Reports*, 474(1-6):1–75, April 2009. ISSN 0370-1573. doi: 10.1016/j.physrep.2009.02.004.
- [161] Roberto Casalbuoni and Giuseppe Nardulli. Inhomogeneous superconductivity in condensed matter and QCD. *Rev. Mod. Phys.*, 76(1):263–320, Feb 2004. doi: 10.1103/RevModPhys.76.263.

- [162] Mark G. Alford, Andreas Schmitt, Krishna Rajagopal, and Thomas Schäfer. Color superconductivity in dense quark matter. *Rev. Mod. Phys.*, 80(4):1455–1515, Nov 2008. doi: 10.1103/RevModPhys.80.1455.
- [163] M. A. Baranov, C. Lobo, and G. V. Shlyapnikov. Superfluid pairing between fermions with unequal masses. *Phys. Rev. A*, 78(3):033620, Sep 2008. doi: 10.1103/PhysRevA.78.033620.
- [164] D. S. Petrov. Three-body problem in Fermi gases with short-range interparticle interaction. *Phys. Rev. A*, 67(1):010703, Jan 2003. doi: 10.1103/PhysRevA.67.010703.
- [165] D. S. Petrov, C. Salomon, and G. V. Shlyapnikov. Diatomic molecules in ultracold Fermi gases: novel composite bosons. *Journal of Physics B: Atomic, Molecular and Optical Physics*, 38(9):S645, 2005. doi: 10.1088/0953-4075/38/9/014.
- [166] D. Blume. Small mass- and trap-imbalanced two-component Fermi systems. *Phys. Rev. A*, 78(1):013613, Jul 2008. doi: 10.1103/PhysRevA.78.013613.
- [167] M. Iskin and C. J. Williams. Trap-imbalanced fermion mixtures. *Phys. Rev. A*, 77(1):013605, Jan 2008. doi: 10.1103/PhysRevA.77.013605.
- [168] S. A. Siloti. Trap- and population-imbalanced two-component Fermi gas in the Bose-Einstein-condensate limit. *Phys. Rev. A*, 81(1):013623, Jan 2010. doi: 10.1103/PhysRevA.81.013623.
- [169] Aurel Bulgac, Michael McNeil Forbes, and Achim Schwenk. Induced p -wave superfluidity in asymmetric Fermi gases. *Phys. Rev. Lett.*, 97(2):020402, Jul 2006. doi: 10.1103/PhysRevLett.97.020402.
- [170] Robert Raussendorf, Daniel E. Browne, and Hans J. Briegel. Measurement-based quantum computation on cluster states. *Phys. Rev. A*, 68(2):022312, Aug 2003. doi: 10.1103/PhysRevA.68.022312.
- [171] J.C. Angles d’Auriac, M. Preissmann, and R. Rammal. The random field Ising model: algorithmic complexity and phase transition. *J. Physique Lett.*, 46(5):173–180, 1985. doi: 10.1051/jphyslet:01985004605017300.